

Enzo+Moray: Radiation Hydrodynamics Adaptive Mesh Refinement Simulations with Adaptive Ray Tracing

John H. Wise^{1*} and Tom Abel²

¹ *Department of Astrophysical Sciences, Princeton University, Peyton Hall, Ivy Lane, Princeton, NJ 08544, USA*

² *Kavli Institute for Particle Astrophysics and Cosmology, Stanford University, Menlo Park, CA 94025, USA*

16 March 2011

ABSTRACT

We describe a photon-conserving radiative transfer algorithm, using a spatially-adaptive ray tracing scheme, and its parallel implementation into the adaptive mesh refinement (AMR) cosmological hydrodynamics code, ENZO. By coupling the solver with the energy equation and non-equilibrium chemistry network, our radiation hydrodynamics framework can be utilised to study a broad range of astrophysical problems, such as stellar and black hole (BH) feedback. Inaccuracies can arise from large timesteps and poor sampling, therefore we devised an adaptive time-stepping scheme and a fast approximation of the optically-thin radiation field with multiple sources. We test the method with several radiative transfer and radiation hydrodynamics tests that are given in Iliev et al. (2006, 2009). We further test our method with more dynamical situations, for example, the propagation of an ionisation front through a Rayleigh-Taylor instability, time-varying luminosities, and collimated radiation. The test suite also includes an expanding H II region in a magnetised medium, utilising the newly implemented magnetohydrodynamics module in ENZO. This method linearly scales with the number of point sources and number of grid cells. Our implementation is scalable to 512 processors on distributed memory machines and can include radiation pressure and secondary ionisations from X-ray radiation. It is included in the newest public release of ENZO.

Key words: cosmology — methods: numerical — hydrodynamics — radiative transfer.

1 INTRODUCTION

Radiation from stars and black holes strongly affects their surroundings and plays a crucial role in topics such as stellar atmospheres, the interstellar medium (ISM), star formation, galaxy formation, supernovae (SNe) and cosmology. It is a well-studied problem (e.g. Mathews 1965; Rybicki & Lightman 1979; Mihalas & Mihalas 1984; Yorke 1986); however, its treatment in multi-dimensional calculations is difficult because of the dependence on seven variables – three spatial, two angular, frequency, and time. The non-local nature of the thermal and hydrodynamical response to radiation sources further adds to the difficulty. Depending on the problem of interest some simplifying assumptions may be made.

An important case was considered by Strömgren (1939) for an ultraviolet (UV) radiation source photo-ionising a

static uniform neutral medium. When recombinations balance photo-ionisations, the radius of a so-called H II region,

$$R_s = \left(\frac{3\dot{N}_\gamma}{4\pi\alpha_B n_H^2} \right)^{1/3}, \quad (1)$$

where \dot{N}_γ is the ionising photon luminosity, α_B is the recombination rate, and n_H is the ambient hydrogen number density. Furthermore he found that the delineation between the neutral and ionised medium to be approximately the mean free path of the ionising radiation. His seminal work was expanded upon by Spitzer (1948, 1949, 1954) and Spitzer & Savedoff (1950), who showed that the ionising radiation heated the medium to $T \sim 10^4$ K. If the density is equal on both sides of the ionisation front, then this over-pressurised region would expand and drive a shock outwards (e.g. Oort 1954; Schatzman & Kahn 1955). These early works provided the basis for the modern topic of radiation hydrodynamics of the ISM. A decade later, the first radiation hydrodynamical numerical models of H II regions in spherical symmetry and plane-parallel ionisation fronts

* Hubble Fellow; e-mail: jwise@astro.princeton.edu

were developed (e.g. Mathews 1965; Lasker 1966; Hjellming 1966). They described the expansion of the ionisation front and the evolution of its associated shock wave that carries most of the gas away from the source. At the same time, theoretical models of ionisation fronts matured and were classified by Kahn (1954) and Axford (1961) as either R-type (rare) or D-type (dense). In R-type fronts, the ionised gas density is higher than the neutral gas density, and in D-type fronts, the opposite is true. R-type fronts travel supersonically with respect to the neutral gas, whereas D-type fronts are subsonic. Furthermore “weak” and “strong” R-type fronts move supersonically and subsonically with respect to the ionised gas, respectively. The same terminology conversely applies to D-type fronts. “Critical” fronts are defined as moving exactly at the sound speed. These works established the evolutionary track of an expanding H II illuminated by a massive star in a uniform medium:

(i) Weak R-type: When the star (gradually) starts to shine, the ionisation front will move supersonically through the ambient medium. The gas is heated and ionised, but otherwise left undisturbed. This stage continues until $r \sim 0.02R_s$.

(ii) Critical R-type: As the ionisation front moves outwards, it begins to slow because of the geometric dilution of the radiation. It becomes a critical R-type front, which is equivalent to an isothermal shock in the neutral gas.

(iii) Strong and weak D-type: The front continues to slow, becoming a strong D-type front, and then a critical D-type front. From this point forward, it is moving subsonically with respect to the ionised gas, i.e. a weak D-type front. Thus sound waves can travel across the ionisation front and form a shock. The ionisation front detaches from the shock, putting the shock ahead of the ionisation front.

(iv) Expansion phase: After the shock forms, the H II region starts to expand, lowering the interior density and thus the recombination rates. This increases the number of photons available for ionising the gas. The sphere expands until it reaches pressure equilibrium with the ambient medium at $r \sim 5R_s$.

In the 1970’s and 1980’s, algorithmic and computational advances allowed numerical models to be expanded to two dimensions, mainly using axi-symmetric to simplify the problem (e.g. Bodenheimer et al. 1979; Sandford et al. 1982; Yorke et al. 1983). One topic that was studied extensively were champagne flows. Here the source is embedded in an overdense region, and the H II region escapes from this region in one direction. The interface between the ambient and dense medium was usually set up to be a constant pressure boundary. When the ionisation front passes this boundary, the dense, ionised gas is orders of magnitude out of pressure equilibrium as the temperatures on both sides of initial boundary are within a factor of a few. In response, the gas is accelerated outwards in this direction, creating a fan-shaped outflow.

Only in the past 15 years, computational resources have become large enough, along with further algorithmic advances, to cope with the requirements of three-dimensional calculations. There are two popular methods to solve the radiative transfer equation in three-dimensions:

- Moment methods: The angular moments of the radi-

ation field can describe its angular structure, which are related to the energy, flux, and radiation pressure (Auer & Mihalas 1970; Norman et al. 1998). These have been implemented in conjunction with short characteristics (Stone et al. 1992, 2D), with long characteristics (Finlator et al. 2009), with a variable Eddington tensor in the optically thin limit (OTVET; Gnedin & Abel 2001; Petkova & Springel 2009), and with an M1 closure relation (González et al. 2007; Aubert & Teyssier 2008). Moment methods have the advantage of being fast and independent of the number of radiation sources. However, they are diffusive and result in incorrect shadows in some situations.

- Ray tracing: Radiation can be propagated along rays that extend through the computational grid (e.g. Razoumov & Scott 1999; Abel et al. 1999; Ciardi et al. 2001; Sokasian et al. 2001; Whalen & Norman 2006; Rijkhorst et al. 2006; Mellema et al. 2006; Alvarez et al. 2006a; Trac & Cen 2007; Krumholz et al. 2007; Paardekooper et al. 2010) or particle set (e.g. Susa 2006; Johnson et al. 2007; Pawlik & Schaye 2008, 2010; Altay et al. 2008; Hasegawa et al. 2009). In general, these methods are very accurate but computationally expensive because the radiation field must be well sampled by the rays with respect to the spatial resolution of the grid or particles.

Until the mid-2000’s the vast majority of the three-dimensional calculations were performed with static density distributions. One example is calculating cosmological reionisation by post-processing of density fields from N-body simulations (Ciardi et al. 2001; Sokasian et al. 2001; McQuinn et al. 2007; Iliev et al. 2006, 2007). Any hydrodynamical response to the radiation field was thus ignored. Several radiative transfer codes were compared in four purely radiative transfer tests in Iliev et al. (2006, hereafter RT06). Only recently has the radiative transfer equation been coupled to the hydrodynamics in three-dimensions (e.g. Krumholz et al. 2007). In the second comparison paper (Iliev et al. 2009, hereafter RT09), results from these radiation hydrodynamics codes were compared. Even more rare are ones that couple it with magneto-hydrodynamics (e.g. Krumholz et al. 2007). The tests in RT06 and RT09 were kept relatively simple to ease the comparison.

In this paper, we present our implementation, ENZO+MORAY, of adaptive ray tracing (Abel & Wandelt 2002) in the cosmological hydrodynamics adaptive mesh refinement (AMR) code, ENZO (Bryan & Norman 1997; O’Shea et al. 2004). The radiation field is coupled to the hydrodynamics solver at small time-scales, enabling it to study radiation hydrodynamical problems. We have used this code to investigate the growth of an H II region from a $100M_\odot$ Population III (Pop III) star (Abel et al. 2007), the early stages of reionisation from Pop III stars (Wise & Abel 2008a), radiative feedback on the formation of high redshift dwarf galaxies (Wise & Abel 2008b; Wise et al. 2010), ultraviolet radiation escape fractions from dwarf galaxies before reionisation (Wise & Cen 2009), negative radiative feedback from accreting Pop III seed black holes (Alvarez et al. 2009), and radiative feedback in accreting supermassive black holes (Kim et al. 2011, in prep.). We have included

ENZO+MORAY in the latest public release of ENZO¹, and it is also coupled with the newly added MHD solver in ENZO (Wang & Abel 2009).

We have structured this paper as follows. In Section 2, we describe the mathematical connections between adaptive ray tracing and the radiative transfer equation. Furthermore, we detail how physics other than photo-ionisation and photo-heating are included. We then derive a geometric correction factor to any ray tracing method to improve accuracy. We end the section by describing a new computational technique to approximate an optically-thin radiation field with ray tracing and multiple sources. In Section 3, we cover the details of our radiation hydrodynamics implementation in ENZO, specifically (1) the ray tracing algorithms, (2) coupling with the hydrodynamics solver, (3) several methods to calculate the radiative transfer timestep, and (4) our parallelisation strategy. We present our results from the RT06 radiative transfer tests in Section 4. Afterwards in Section 5, we show the results from the RT09 radiation hydrodynamics tests. In Section 6, we expand on these tests to include more dynamical and complex setups to demonstrate the flexibility and high fidelity of ENZO+MORAY. Section 7 gives the results from spatial, angular, frequency, and temporal resolution tests. In Section 8, we illustrate the improvements from the geometric correction factor and our optically-thin approximation. We also show the effects of X-ray radiation and radiation pressure in this section. Finally in Section 9, we demonstrate the parallel scalability of ENZO+MORAY. Last Section 10 summarises our method and results.

2 TREATMENT OF RADIATIVE TRANSFER

Radiation transport is a well-studied topic, and we begin by describing our approach in solving the radiative transfer equation, which in comoving coordinates (Gnedin & Ostriker 1997) is

$$\frac{1}{c} \frac{\partial I_\nu}{\partial t} + \frac{\hat{n} \cdot \nabla I_\nu}{\bar{a}} - \frac{H}{c} \left(\nu \frac{\partial I_\nu}{\partial \nu} - 3I_\nu \right) = -\kappa_\nu I_\nu + j_\nu. \quad (2)$$

Here $I_\nu \equiv I(\nu, \mathbf{x}, \Omega, t)$ is the radiation specific intensity in units of energy per time t per solid angle per unit area per frequency ν . $H = \dot{a}/a$ is the Hubble constant, where a is the scale factor. $\bar{a} = a/a_{em}$ is the ratio of scale factors at the current time and time of emission. The second term represents the propagation of radiation, where the factor $1/\bar{a}$ accounts for cosmic expansion. The third term describes both the cosmological redshift and dilution of radiation. On the right hand side, the first term considers the absorption coefficient $\kappa_\nu \equiv \kappa_\nu(\mathbf{x}, \nu, t)$, and the second term $j_\nu \equiv j_\nu(\mathbf{x}, \nu, t)$ is the emission coefficient that includes any point sources of radiation or diffuse radiation. We neglect any (v/c) terms in equation (2) that become important in the dynamic diffusion limit ($l\kappa(v/c) \gg 1$), where l is the characteristic size of the system. This occurs in relativistic flows or very optically thick systems, such as stellar interiors or radiation-dominated shocks (see Krumholz et al. 2007, for a rigorous derivation that includes (v/c) terms to second-order).

Solving this equation is difficult because of its high dimensionality; however, we can make some appropriate

approximations to reduce its complexity in order to include radiation transport in numerical calculations. Typically timesteps in dynamic calculations are small enough so that $\Delta a/a \ll 1$, therefore $\bar{a} = 1$ in any given timestep, reducing the second term to $\hat{n} \partial I_\nu / \partial \mathbf{x}$. To determine the importance of the third term, we evaluate the ratio of the third term to the second term. This is HL/c , where L is the simulation box length. If this ratio is $\ll 1$, we can ignore the third term. For example at $z = 5$, this ratio is 0.1 when $L = c/H(z = 5) = 53$ proper Mpc. In large boxes where the light crossing time is comparable to the Hubble time, then it becomes important to consider cosmological redshifting and dilution of the radiation. Thus equation (2) reduces to the non-cosmological form in this local approximation,

$$\frac{1}{c} \frac{\partial I_\nu}{\partial t} + \hat{n} \frac{\partial I_\nu}{\partial \mathbf{x}} = -\kappa_\nu I_\nu + j_\nu. \quad (3)$$

We choose to represent the source term j_ν as point sources of radiation (e.g. stars, quasars) that emit radial rays that are propagated along the direction \hat{n} . Next we describe this discretisation and its contribution to the radiation field.

2.1 Adaptive Ray Tracing

Ray tracing is an accurate method to propagate radiation from point sources on a computational grid, given that there are a sufficient number of rays passing through each cell. Along a ray, the radiative transfer equation reads

$$\frac{1}{c} \frac{\partial P}{\partial t} + \frac{\partial P}{\partial r} = -\kappa P, \quad (4)$$

where P is the photon number flux along the ray. To sample the radiation field at large radii, ray tracing requires at least $N_{ray} = 4\pi R^2/(\Delta x)^2$ rays to sample each cell with one ray, where R is the radius from the source to the cell and Δx is the cell width. If one were to trace N_{ray} rays out to R , the cells at a smaller radius r would be sampled by, on average, $(r/R)^2$ rays, which is computationally wasteful because only a few rays per cell, as we will show later, provides an accurate calculation of the radiation field.

We avoid this inefficiency by utilising adaptive ray tracing (Abel & Wandelt 2002), which progressively splits rays when the sampling becomes too coarse and is based on Hierarchical Equal Area isoLatitude Pixelation (HEALPix; Górski et al. 2005). In this scheme, the rays are traced along normal directions of the centres of HEALPix pixels, which evenly divides a sphere into equal areas. The rays are initialised at each point source with the photon luminosity (ph s^{-1}) equally spread across $N_{pix} = 12 \times 4^l$ rays, where l is the initial HEALPix level. We usually find $l = 0$ or 1 is sufficient because these coarse rays will usually be split before traversing the first cell.

The rays are traced through the grid in a typical fashion (e.g. Abel et al. 1999), in which we calculate the next cell boundary crossing. The ray segment length crossing the cell is

$$dr = R_0 - \min_{i=1 \rightarrow 3} [(x_{cell,i} - x_{src,i})/\hat{n}_{ray,i}], \quad (5)$$

where R_0 , \hat{n}_{ray} , $x_{cell,i}$, and $x_{src,i}$ are the initial distance travelled by the ray, normal direction of the ray, the next cell boundary crossing in the i -th dimension, and the position of the point source that emitted the ray, respectively. However

¹ <http://enzo.googlecode.com>

Table 1. Variable definitions used in Sections 2 and 3

Variable	Description
A_{cell}	Cell face area
a	Scale factor
C_{H}	Collisional ionization rate of hydrogen
$C_{\text{RT,cf}}$	CFL safety factor in timestep calculation
$D_{\text{c,i}}$	Distance from ray segment center to cell center
D_{edge}	Distance from ray segment center to cell edge
dP	Photon loss from absorption
dP_{C}	Photon loss from Compton Scattering
$d\mathbf{p}_{\gamma}$	Momentum change from radiation pressure
dt_P	Photon timestep
E_{ph}	Photon energy
E_i	Ionization energy of absorber
f_c	Geometric correction factor
f_{shield}	Shielding function for H ₂
H	Hubble constant
I_{ν}	Specific intensity
j_{ν}	Emission coefficient
k_{ph}	Photo-ionization rate
k_{diss}	Photo-dissociation rate of H ₂
L_{pix}	Linear width of a HEALPix pixel
l	HEALPix level
N_{H2}	Column density of H ₂
n_{abs}	Number density of absorber
$N_{\text{pix}}(l)$	HEALPix pixels on level l
N_{ray}	Rays per cell
\dot{N}_{γ}	Photon luminosity
\hat{n}	Normal direction of radiation
n_x	Number density of absorber x
P	Photon flux
r	Radius
r_{cell}	Distance from the radiation source to the cell center
r_{ray}	Distance from the radiation source to the next cell boundary crossing
V_{cell}	Cell volume
v_{IF}	Ionization front velocity
$x_{0,i}$	Cell center coordinates
$x_{\text{cell},i}$	Next cell boundary crossing in the i -th dimension
$x_{\text{src},i}$	Source position in the i -th dimension
Y_{x}	Secondary ionization factors
α_B	Case-B recombination rate
Γ_{ph}	Photo-heating rate
Δx	Cell width
Φ_c	Angular resolution in units of rays per cell area
κ_{ν}	Absorption coefficient
λ_{mfp}	Mean free path
Ω_{ray}	Solid angle associated with a ray
σ_{abs}	Cross-section of absorber
θ_{ray}	Angle associated with a ray
τ	Optical depth

before the ray travels across the cell, we evaluate the ratio of the face area A_{cell} of the current cell and the solid angle Ω_{ray} of the ray,

$$\Phi_c = \frac{A_{\text{cell}}}{\Omega_{\text{ray}}} = \frac{N_{\text{pix}}(\Delta x)^2}{4\pi R_0^2}. \quad (6)$$

If Φ_c is less than a pre-determined value (usually > 3), the ray is split into 4 child rays. We investigate the variations in solutions with Φ_c in §7.2. The pixel numbers of the child rays p' are given by the “nested” scheme of HEALPix at

the next level, i.e. $p' = 4 \times p + [0, 1, 2, 3]$, where p is the original pixel number. The child rays (1) acquire the new normal vectors of the pixels, (2) retain the same radius of the parent ray, and (3) gets a quarter of the photon flux of the parent ray. Afterwards the parent ray is discontinued.

A ray propagates and splits until

- (i) the photon has travelled $c \times dt_P$, where dt_P is the radiative transfer timestep,
- (ii) its photon flux is almost fully absorbed ($> 99.9\%$) in a single cell, which significantly reduces the computational time if the radiation volume filling fraction is small,
- (iii) the photon leaves the computational domain with isolated boundary conditions, or
- (iv) the photon travels $\sqrt{3}$ of the simulation box length with periodic boundary conditions.

In the first case, the photon is halted at that position and saved, where it will be considered in the solution of I_{ν} at the next timestep. In the next timestep, the photon will encounter a different hydrodynamical and ionisation state, hence κ , in its path. Furthermore any time variations of the luminosities will be retained in the radiation field. This is how this method retains the time derivative of the radiative transfer equation. The last restriction prevents our method from considering sources external to the computational domain, but a uniform radiation background can be used in conjunction with ray tracing in ENZO+MORAY that adds the local radiation field to the background intensity.

2.2 Radiation Field

The radiation field is calculated by integrating equation (4) along each ray, which is done by considering the discretisation of the ray into segments. In the following section, we assume the rays are monochromatic. For convenience, we express the integration in terms of optical depth $\tau = \int \kappa(r, t) dr$, and for a ray segment,

$$d\tau = \sigma_{\text{abs}}(\nu) n_{\text{abs}} dr. \quad (7)$$

Here σ_{abs} and n_{abs} are the cross section and number density of the absorbing medium, respectively. We use the cell-centred density in our calculations. Using trilinearly interpolated densities (see Mellema et al. 2006) did not produce improved results. In the static case, equation (4) has a simple exponential analytic solution, and the photon flux of a ray is reduced by

$$dP = P \times (1 - e^{-\tau}) \quad (8)$$

as it crosses a cell. We equate the photo-ionisation rate to the absorption rate, resulting in photon conservation (Abel et al. 1999; Mellema et al. 2006). Thus the photo-ionisation k_{ph} and photo-heating Γ_{ph} rates associated with a single ray are

$$k_{\text{ph}} = \frac{P(1 - e^{-\tau})}{n_{\text{abs}} V_{\text{cell}} dt_P}, \quad (9)$$

$$\Gamma_{\text{ph}} = k_{\text{ph}} (E_{\text{ph}} - E_i), \quad (10)$$

where V_{cell} is the cell volume, E_{ph} is the photon energy, and E_i is the ionisation energy of the absorbing material. In each cell, the photo-ionisation and photo-heating rates from each ray in the calculation are summed, and after the

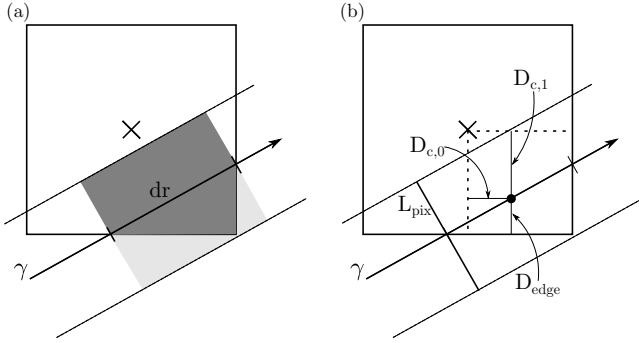


Figure 1. (a) A two-dimensional illustration of the overlap between the beam associated with a ray γ and a computational cell. The ray has a segment length of dr passing through the cell. The covering area is denoted by dark grey, where the full area ($dr \times L_{\text{pix}}$) is colored by the dark and light grey. The photo-ionisation and photo-heating rates should be corrected by the ratio of these areas, i.e. the overlap fraction f_c . (b) Annotation of quantities used in this geometric correction.

ray tracing is complete, these rates can be used to update the ionisation state and energy of the cells. Considering a system with only hydrogen photo-ionisations and radiative recombinations, these changes are very straightforward and is useful for illustrative purposes. The change in neutral hydrogen is

$$\frac{dn_{\text{H}}}{dt} = \alpha_B n_e n_p - C_{\text{H}} n_e n_{\text{H}} - k_{\text{ph}}, \quad (11)$$

where $\alpha_B = 2.59 \times 10^{-13} \text{ cm}^3 \text{ s}^{-1}$ is the recombination coefficient at 10^4 K in the Case B on-the-spot approximation in which all recombinations are locally reabsorbed, (Spitzer 1978), and C_{H} is the collisional ionisation rate. However, for more accurate solutions in calculations that consider several chemical species, the photo-ionisation rates are terms in the relevant chemical networks (e.g. Abel et al. 1997).

2.3 Geometric Corrections

For a ray tracing method to accurately, i.e. without non-spherical artifacts, compute the radiation field, the computational grid must be well-sampled by the rays. The main source of potential artifacts is the geometrical difference between the cell and the HEALPix pixel relevant in the angular integration of the intensity over the cell. In this section, we devise a correction scheme to account for these differences. Consider the solid angle Ω_{ray} and photon flux P associated with a single ray, and assume the flux is constant across Ω_{ray} . There exists a discrepancy between the geometry cell face and HEALPix pixel when the pixel does not cover the entire cell face, which is illustrated in Fig. 1. This mismatch causes non-spherical artifacts and is most apparent in the optically thin case, where the area of the pixel is dominant over $(1 - e^{-\tau})$ when calculating k_{ph} . One can avoid these artifacts by increasing the sampling Φ_c to high values (> 10) but we have formulated a simple geometric correction to the calculation of the radiation field. This correction is not unique to the HEALPix formalism but can be applied to any type of pixelisation.

The contribution to k_{ph} and Γ_{ph} must be corrected by the covering factor f_c of the pixel with respect to the cell.

When the pixel is fully contained within the cell face, $f_c \equiv 1$. Because the geometry of the pixel can be complex with curved edges, we approximate f_c by assuming the pixel is square. The covering factor is thus related to the width of a pixel, $L_{\text{pix}} = R_0 \theta_{\text{pix}}$, and the distance from the ray segment midpoint to the closest cell boundary $D_{c,i}$, which is depicted in Fig. 1. To estimate f_c , we first find the distance $d_{\text{centre},i}$ from the midpoint of the ray segment to the cell centre $x_{0,i}$ in orthogonal directions,

$$D_{c,i} = \left| R_{0,i} + \hat{n}_i \frac{dr}{2} - x_{0,i} \right|, \quad (12)$$

where $R_{0,i}$ is the distance travelled by the ray in each orthogonal direction. The distance to the closest cell boundary is $D_{\text{edge}} = dx/2 - \max_{i=1 \rightarrow 3}(D_{c,i})$. Thus the covering factor is related to the square of the ratio between the L_{pix} and D_{edge} by

$$f_c = \left(\frac{1}{2} + \frac{D_{\text{edge}}}{L_{\text{pix}}} \right)^2 \quad (13)$$

One half of the pixel is always contained within the cell, which results in the factor of $1/2$. Finally we multiply k_{ph} and Γ_{ph} by f_c but leave the absorbed radiation dP untouched because this would underestimate the attenuation of the incoming radiation. Using f_c calculated like above, the method is no longer photon conserving. In our implementation, we felt that the spherical symmetry obtained outweighed the loss of photon conservation. However we show that there are no perceptible deviations from photon conservation in §4.1 and §7.1.

We briefly next describe how to retain photon conservation with a geometric correction. Notice that we compute f_c by only considering the distances in orthogonal directions. A better estimate would consider the distance between the cell boundary and ray segment midpoint in the direction between the midpoint and cell centre of $\mathbf{x}_{\text{mid}} - \mathbf{x}_0$. We find that the method outlined here provides a sufficient correction factor to avoid any non-spherical artifacts and deviations from photon conservation. Furthermore in principle, the ray should also contribute to any neighboring cells that overlap with Ω_{ray} , which is the key to be photon conservative with such a geometric correction.

2.4 Optically Thin Approximation

In an optically thin medium, radiation is only attenuated by geometric dilution in the local approximation to Equation (2), i.e. the inverse square law. With such a simple solution, the tracing of rays is wasteful, however these rays must be propagated because the the medium farther away can be optically thick. Here we describe a method that minimizes the computational work of ray tracing in the optically thin regime by exploiting this fact. Each ray tracks the total column density N_{abs} and the equivalent total optical depth τ traversed by the photon. If $\tau < \tau_{\text{thin}} \sim 0.1$ after the ray exits the cell, we calculate the photo-ionisation and photo-heating rates directly from the incoming ray instead of the luminosity of the source.

$$k_{\text{ph}} = \frac{\sigma_{\text{abs}} P}{dt_P \theta_{\text{pix}}} \frac{r_{\text{cell}}}{r_{\text{ray}}}. \quad (14)$$

Note that the photon number P in the ray has already been geometrically diluted by ray splitting. Here r_{cell} and r_{ray} are the radii from the radiation source to the cell centre and where the ray exits the cell. Thus the last factor corrects the flux to a value appropriate for the cell centre. The photo-heating ray is calculated in the same manner as the general case, $\Gamma_{\text{ph}} = k_{\text{ph}}(E_{\text{ph}} - E_i)$. This should only be evaluated once per cell per radiation source. No photons are removed from the ray. With this method, we only require one ray travel through each cell where the gas is optically thin, thus reducing the computational expense.

We must be careful not to overestimate the radiation when multiple rays enter a single cell. In the case of a single radiation source, the solution is simple – only assign the cell the photo-ionisation and photo-heating rates when $k_{\text{ph}} = 0$. However in the case with multiple sources, this is no longer valid, and we must sum the flux from all optically thin sources. Only one ray per source must contribute to a single cell in this framework. We create a flagging field that marks whether a cell has already been touched by an optically thin photon from a particular radiation source. Naively, we would be restricted to tracing rays from a single source at a time if we use a boolean flagging field. However we can trace rays for 32 sources at a time by using bitwise operations on a 32-bit integer field. For example in C, we would check if an optically thin ray from the n -th source has propagated through cell i by evaluating `MarkerField[i] >> n & 1`. If false, then we can add the optically thin approximation [equation (14)] to the cell and set `MarkerField[i] |= (1 >> n)`; to mark the cell.

2.5 Additional Physics

Other radiative processes can also be important in some situations, such as attenuation of radiation in the Lyman-Werner bands, secondary ionisations from X-ray radiation, Compton heating of from scattered photons, and radiation pressure. We describe our implementation of these physics next.

2.5.1 Absorption of Lyman-Werner Radiation

Molecular hydrogen can absorb photons in the Lyman-Werner bands through the two-step Solomon process, which for the lowest ro-vibrational states already consists of 76 absorption lines ranging from 11.1 to 13.6 eV (Stecker & Williams 1967; Dalgarno & Stephens 1970; Haiman et al. 2000). Each of these spectral lines can be modelled with a typical exponential attenuation equation (Ricotti et al. 2001), but Draine & Bertoldi (1996) showed that this self-shielding is well modeled with the following relation to total H_2 column density

$$f_{\text{shield}}(N_{\text{H}_2}) = \begin{cases} 1 & (N_{\text{H}_2} \leq 10^{14}) \\ (N_{\text{H}_2}/10^{14})^{-0.75} & (N_{\text{H}_2} > 10^{14}) \end{cases}, \quad (15)$$

where N_{H_2} is in units of cm^{-2} . To incorporate this shielding function into the ray tracer, we store the total H_2 column density and calculate the H_2 dissociation rate by summing the contribution of all rays,

$$k_{\text{diss}} = \sum_{\text{rays}} \frac{P \sigma_{\text{LW}} \Omega_{\text{ray}} r^2 dr}{A_{\text{cell}} dV dt_P}, \quad (16)$$

where $\sigma_{\text{LW}} = 3.71 \times 10^{18} \text{cm}^2$ is the effective cross-section of H_2 (Abel et al. 1997). To account for absorption, we attenuate the photon number flux by

$$dP = P[f_{\text{shield}}(N_{\text{H}_2} + dN_{\text{H}_2}) - f_{\text{shield}}(N_{\text{H}_2})], \quad (17)$$

where dN_{H_2} is the H_2 column density in the current cell.

2.5.2 Secondary Ionisations from X-rays

At the other end of the spectrum, a high-energy ($E_{\text{ph}} \gtrsim 100$ eV) photon can ionise multiple neutral hydrogen and helium atoms, and this should be considered in such radiation fields. Shull & van Steenberg (1985) studied this effect with Monte Carlo calculations over varying electron fractions and photon energies up to 3 keV. They find that the excitation of hydrogen and helium and the ionisation of He II is negligible. The number of secondary ionisations of H and He is reduced from the ratio of the photon and ionisation energies (E_{ph}/E_i) by a factor of

$$Y_{\text{K,H}} = 0.3908(1 - x^{0.4092})^{1.7592}, \quad (18)$$

$$Y_{\text{K,He}} = 0.0554(1 - x^{0.4614})^{1.6660}, \quad (19)$$

where x is the electron fraction. The remainder of the photon energy is deposited into thermal energy that is approximated by

$$Y_{\text{T}} = 0.9971[1 - (1 - x^{0.2663})^{1.3163}] \quad (20)$$

and approaches one as $x \rightarrow 1$. Thus in gas with low electron fractions, most of the energy results in ionisations of hydrogen and helium, and in nearly ionised gas, the energy goes into photo-heating.

2.5.3 Compton Heating from Photon Scattering

High energy photons can also cause Compton heating by scattering off free electrons. During a scattering, a photon loses $\Delta E(T_e) = 4kT_e \times (E_{\text{ph}}/m_e c^2)$ of energy, where T_e is the electron temperature. For the case of monochromatic energy groups, we model this process by considering that the photons are absorbed by a factor of

$$\frac{dP_C}{P} = (1 - e^{-\tau_e}) \frac{\Delta(T_e)}{E_{\text{ph}}}, \quad (21)$$

which is the equivalent of the photon energy decreasing. Here $\tau_e = n_e \sigma_{\text{KN}} dl$ is the optical depth to Compton scattering, and σ_{KN} is the non-relativistic Klein-Nishina cross section (Rybicki & Lightman 1979). The Compton heating rate is thus

$$\Gamma_{\text{ph,C}} = \frac{dP_C}{n_e V_{\text{cell}} dt_P}, \quad (22)$$

which has been used in Kim et al. (2011).

2.5.4 Radiation Pressure

Another relevant process is radiation pressure, where the absorption of radiation transfers momentum from photons to the absorbing medium. This is easily computed by considering the momentum

$$d\mathbf{p}_\gamma = \frac{dP E_{\text{ph}}}{c} \hat{\mathbf{r}} \quad (23)$$

of the absorbed radiation from the incoming ray, where \hat{r} is the normal direction of the ray. We do not include radiation pressure on dust currently. The resulting acceleration of the gas because of radiation pressure is

$$d\mathbf{a} = \frac{d\mathbf{p}_\gamma}{dt_P \rho V_{\text{cell}}}, \quad (24)$$

where ρ is the gas density inside the cell. This acceleration is then added to the other forces, e.g. gravity, in the calculation in an operator split fashion.

3 NUMERICAL IMPLEMENTATION IN ENZO

In this section, we describe our parallel implementation of the adaptive ray tracing method into ENZO. ENZO is a parallel block-structured AMR (Berger & Colella 1989) code that is publicly available (Bryan & Norman 1997; O’Shea et al. 2004). First we explain the programming design of handling the “photon packages” that are traced along the adaptive rays. We use the terms photon packages and rays interchangeably. Next we focus on the details of the radiation hydrodynamics and then the importance of correct time-stepping. Last we give our parallelisation strategy of tracing rays through an AMR hierarchy. This implementation is included in the v2.0 public version of ENZO.

3.1 Programming Design

Each photon package is stored in the AMR grid with the finest resolution that contains its current position. The photon packages keep track of their (1) photon flux, (2) photon type, (3) photon energy, (4) the time interval of its emission, (5) emission time, (6) current time, (7) radius, (8) total column density, (9) HEALPix pixel number, (10) HEALPix level, and (11) position of the originating source, totaling 60 (88) bytes for single (double) precision. When ENZO uses double precision for grid and particle positions and time, items 4-7 and 11 are double precision.

We only treat point sources of radiation in our implementation; therefore all base level photon packages originate from them. As they travel away from the source, they generally pass through many AMR grids, especially if the simulation has a high dynamic range. This is a challenging programming task as rays are constantly entering and exiting grids. Before any computation, the number of rays in a particular grid is highly unpredictable because the intervening medium is unknown. Furthermore, the splitting of parent rays into child rays and a dynamic AMR hierarchy add to the complexity. Because of this, we store the photon packages as a doubly linked list (Abel & Wandelt 2002). Thus we can freely add and remove them from grids without the concern of allocating enough memory before the tracing commences.

We illustrate the underlying algorithm of the ray tracing module in ENZO in Fig. 2 and the ray tracing algorithm is shown in Fig. 3. The module is only called when advancing the finest AMR level. We describe its steps below.

Step 1.– Create N_{pix} new photon packages on the initial HEALPix level from point sources. Place the new rays in the highest resolution AMR grid that contains the source.

Step 2.– Initialise all radiation fields to zero.

Step 3.– Loop through all AMR grids, tracing any rays that exist in it. For each ray, the following substeps are taken.

Step 3a.– Compute the ray normal based on the HEALPix level and pixel number of the photon package with the HEALPix routine `pix2vec_nest`. One strategy to accelerate the computation is to store ray segment paths in memory (Abel & Wandelt 2002; Krumholz et al. 2007); however this must be recomputed if the grid structure or point source position changes. We do not restrict these two aspects and cannot employ this acceleration method.

Step 3b.– Compute the position of the ray ($\mathbf{r}_{\text{src}} + r\hat{\mathbf{n}}$), the current cell coordinates in floating point and its corresponding integer indices. Here \mathbf{r}_{src} is the position of the point source, r is the distance travelled by the ray, and $\hat{\mathbf{n}}$ is the ray normal.

Step 3c.– Check if a subgrid exists under the current cell. If so, move the ray to a linked list that contains all rays that should be moved to other grids. We call this variable `PhotonMoveList`. Store the destination grid number and level. Continue to the next ray in the grid (step 3a). We determine whether a subgrid exists by creating a temporary 3D field of pointers that either equals the pointer of the current grid if no subgrid exists under the current cell or the child grid pointer that exists under the current cell. This provides a significant speedup when compared to a simple comparison of a photon package position and all of the child grid boundaries. Note that this is the same algorithm used in ENZO when moving collisionless particles to child grids.

Step 3d.– Compute the next cell crossing of the ray and the ray segment length across the cell (Equation 5).

Step 3e.– Compare the solid angle associated with the ray at radius $r + dr$ with a user-defined splitting criterion (Equation 6). If the solid angle is larger than the desired minimum sampling, split the ray into 4 child rays (§2.1). These rays are inserted into the linked list after the parent ray, which is subsequently deleted. Continue to the next ray (step 3a), which will be the first child ray.

Step 3f.– Calculate the geometric correction (Equation 13), the optical depth of the current cell (Equation 7), photo-ionisation and photo-heating rates (Equations 9 and 10), and add the column density of the cell to the total column density of the ray.

Step 3g.– Add the effects of any optional physics modules (§2.5) – secondary ionisations from X-rays, Compton heating from scattering, and radiation pressure.

Step 3h.– Update the current time ($t = t + cdr$), photon flux ($P = P - dP$, Equation 8), and radius of the ray ($r = r + dr$).

Step 3i.– If the photon flux is zero or the total optical depth is large (> 20), delete the ray.

Step 3j.– Check if the ray has travelled a total distance of cdt_P in the last timestep. If we are keeping the time-derivative of the radiative transfer equation, halt the photon. If not (i.e. infinite speed of light), delete the photon.

Step 3k.– Check if the ray has exited the current grid. If false, continue to the next cell (step 3b). If true, move the ray to the linked list `PhotonMoveList`, similar to step 3c. If the ray exits the simulation domain, delete it if the boundary conditions are isolated; otherwise, we change the source position of the ray by a distance $-\text{sign}(\mathbf{n}[\mathbf{i}]) * \text{DomainWidth}[\mathbf{i}]$, where \mathbf{n} is the ray normal, and \mathbf{i} is the

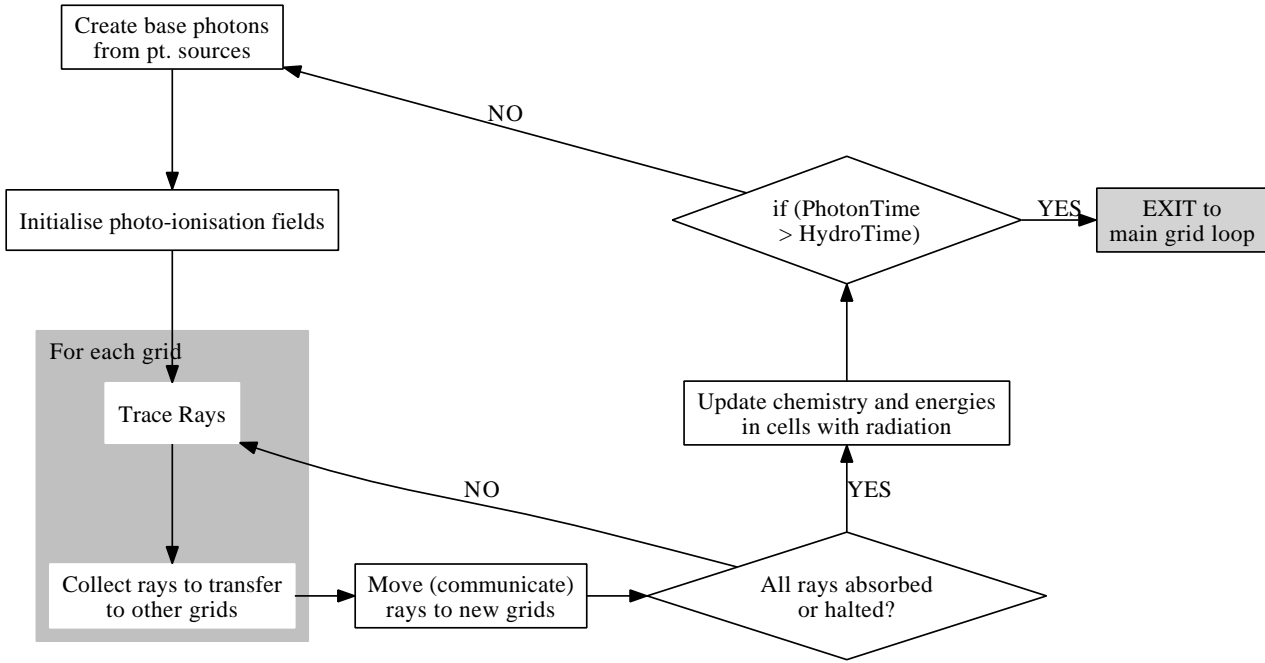


Figure 2. Flow chart for the overall algorithm of the radiative transfer module in ENZO that illustrates (1) the creation of photon packages, (2) ray tracing, (3) the transport of photon packages between AMR grids, and (4) coupling with the hydrodynamics. The ray tracing algorithm, which is contained in the “Trace Rays” is detailed in Fig. 3.

dimension of the outer boundary it has crossed. The radius is kept unchanged. In essence, this creates a “virtual source” outside the box because the ray will be moved to the opposite side of the domain, appearing that it originated from this virtual source.

Step 4.– If any rays exist in the linked list `PhotonMoveList`, move them to their destination grids and return to step 3. This requires MPI communication if the destination grid exists on another processor.

Step 5.– If all rays have not been halted (keeping the time-derivative of the radiative transfer equation), absorbed, or exited the domain, return to step 3.

Step 6.– With the radiation fields updated, call the chemistry and energy solver and update only the cells with radiation, which is discussed further in §3.3.

Step 7.– Advance the time associated with the photons t_P by the global timestep dt_P (for its calculation, see §3.4). If t_P does not exceed the time on the finest AMR level, return to step 1.

3.2 Energy groups

In our implementation, photon packages are monochromatic, i.e. energy groups (Mihalas & Mihalas 1984, Ch. 6), and are assigned a photon type that corresponds whether it is a photon that (1) ionises hydrogen, (2) singly ionises helium, (3) doubly ionises helium, (4) has an X-ray energy, or (5) dissociates molecular hydrogen (Lyman-Werner radiation). One disadvantage of mono-chromatic rays is the number of rays increase with the number of frequency bins. However this allows for early termination of rays that are fully absorbed, which are likely to have high absorption cross-sections (e.g. H I ionisations near 13.6 eV) or a low

initial intensity (e.g. He II ionising photons in typical stellar populations). The other approach used by some groups (e.g. Trac & Cen 2007) is to store all energy groups in a single ray. This reduces the number of the rays generated and the computation associated with the ray tracing. Unless the ray dynamically adjusts its memory allocation for the energy groups as they become depleted, this method is also memory intensive in the situation where most of the energy groups are completely absorbed but a few groups still have significant flux.

In practice, we have found that one energy group per photon type is sufficient to match expected analytical tests (§7.3). For example when modeling Population III stellar radiation (e.g. Abel et al. 2007; Wise & Abel 2008b, for hydrogen ionising radiation only), we have 3 energy groups – H I, He I, He II – each with an energy that equals the average photon energy above the ionisation threshold.

3.3 Coupling with Hydrodynamics

Solving the radiative transfer equation is already an intensive task, but coupling the effects of radiation to the gas dynamics is even more difficult because the radiation fields must be updated on a time-scale such that it can react to the radiative heating, i.e. sound-crossing time. The frequency of its evaluation will be discussed in the next section.

ENZO solves the physical equations in an operator-split fashion over a loop of AMR grids. On the finest AMR level, we call our radiation transport solver before this main grid loop in the following sequence:

- **All grids:**

- (i) Solve for the radiation field with the adaptive ray tracer

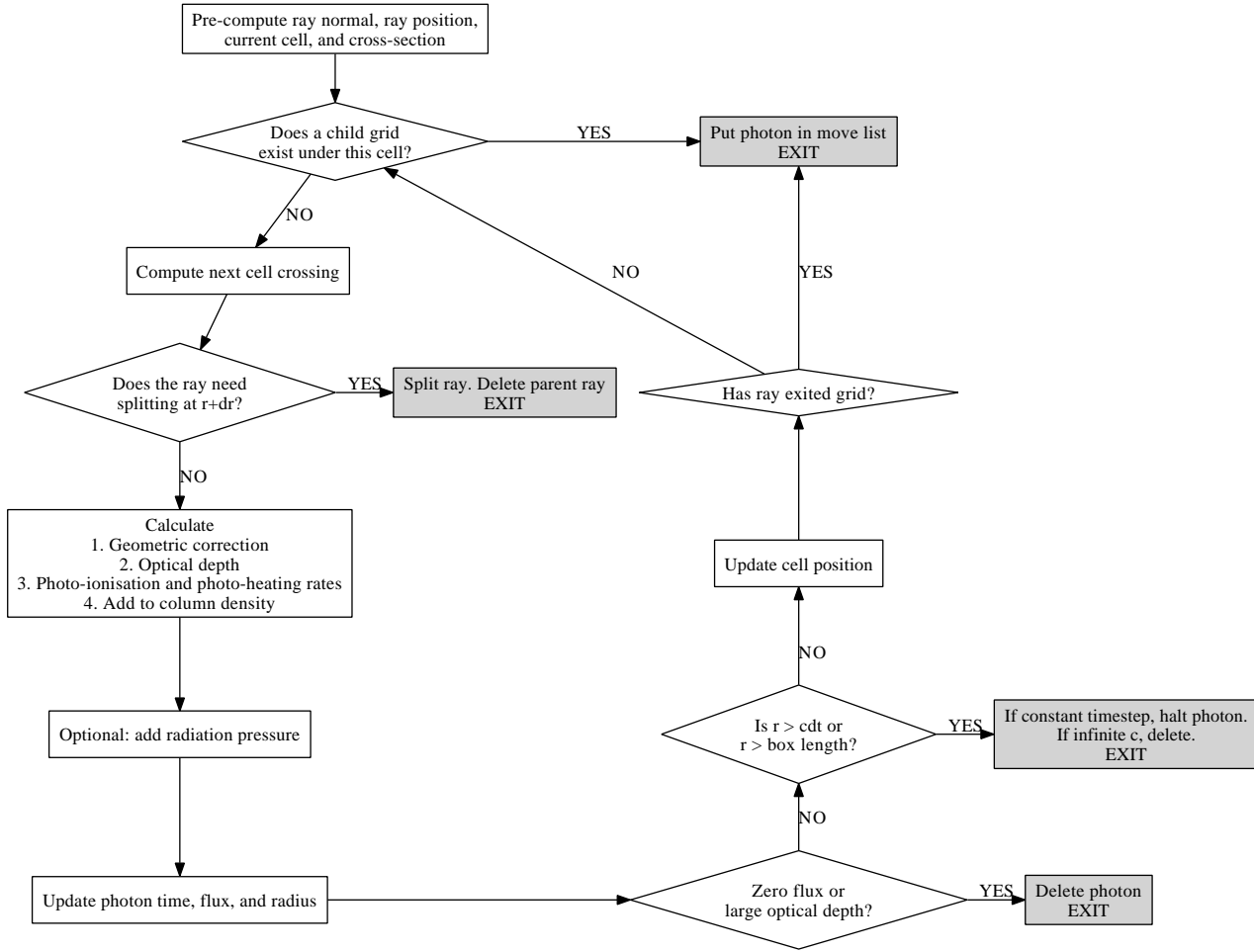


Figure 3. Flow chart for the ray tracing algorithm for one photon passing through a grid. Note that only one step is needed in the routine to adaptively split rays. The remainder is a typical ray tracing method.

(ii) Update species fractions and energies for cells with radiation with a non-equilibrium chemistry solver on subcycles (Equation 25).

- **For each grid:**

- (i) Solve for the gravitational potential with the particle mesh method
- (ii) Solve hydrodynamics
- (iii) Update species fractions and energies for cells without radiation with a non-equilibrium chemistry solver on subcycles (Equation 25).
- (iv) Update particle positions
- (v) Star particle formation

- **All grids:** Update solution from children grids

Since the solver must be called many times, the efficiency of the radiation solver is paramount. After every radiation timestep, we call the non-equilibrium chemistry and energy solver in ENZO. This solves both the energy equation and the network of stiff chemical equations on small timesteps, i.e. subcycles (Anninos et al. 1997). The timestep is

$$dt = \min \left(\frac{0.1n_e}{|dn_e/dt|}, \frac{0.1n_{\text{HI}}}{|dn_{\text{HI}}/dt|}, \frac{0.1e}{|de/dt|}, \frac{dt_{\text{hydro}}}{2} \right), \quad (25)$$

where n_e is the electron number density, e is the specific energy, and dt_{hydro} is the hydrodynamic timestep. This limits the subcycle timestep to a 10% change in either electron density, neutral hydrogen density, or specific energy. In simulations without radiation, ENZO calls this solver in a operation-split manner after the hydrodynamics module for grids only on the AMR level that is being solved. In simulations with radiative transfer, the radiation field can change on much faster time-scales than the normal hydrodynamical timesteps.

For example, a grid on level L might have no radiation in its initial evaluation, but the ionisation front exists just outside its boundary. Then radiation permeates the grid in the time between $t_L \rightarrow t_L + dt_L$, and the energy and chemical state of the cells must be updated with each radiation update to advance the ionisation front accurately. If one does not update these cells, it will appear that the ionisation front does not enter the grid until the next hydrodynamical timestep! Visually this appears as discontinuities in the temperature and electron fraction on grid boundaries. One may avert this problem by solving the chemistry and energy equations for every cell on every radiative transfer timestep, but this is very time consuming and unnecessary, especially if the radiation filling factor is small.

We choose to dynamically split the problem by cells with and without radiation. In every radiation timestep, the chemo-thermal state of *only* the cells with radiation are updated. For the solver subcycling, we replace dt_{hydro} with dt_P in Equation 25 in this case. Once the radiative transfer solver is finished with its timesteps, the hydrodynamic module is called, and then the chemo-thermal state of the cells without radiation are updated on a subcycle timestep stated in Equation 25.

For cells that transition from zero to non-zero photo-ionisation rates, the initial state that enters into the chemistry and energy solver does not correspond to the current time of the radiation transport solver t_{RT} , but either time t_L if the grid level is the finest level because its chemo-thermal state has not been updated or time $t_L + dt_L$ on all other levels. In principle, one could first revert the cell back to time t_L and then update to t_{RT} with the chemistry and energy solver if the cell is on the finest level. However in practice, the time-scales in gas without radiation are small compared to the ionisation and heating time-scales when radiation is introduced. Therefore, we do not perform this correction and find that this does not introduce any inaccuracies in both test problems (see §4) and real world applications.

3.4 Temporal evolution

There have been several methods of choosing a maximal timestep to solve radiation transfer equation while retaining stability and accuracy. We describe several methods to calculate the radiative transfer timestep in this section. With a small enough timestep, the solution is accurate (ignoring any systematic ones), but the solver is slow. Furthermore for very small timesteps, the photon packages only advance a short distance, and they will exist in every dx/dt_P cells with radiation and are stored between timesteps, excessively consuming memory. On the shortest time-scale, one can safely set the timestep to the light-crossing time of a cell (Abel et al. 1999; Trac & Cen 2007) but encounters the problems stated above.

If the timestep is too large, the solution will become inaccurate; specifically, ionisation fronts will advance too slowly, as radiation intensity exponentially drops with a scale length of the mean free path

$$\lambda_{\text{mfp}} = \frac{1}{n_{\text{abs}} \sigma_{\text{abs}}} \quad (26)$$

past the ionisation front. For example in our implementation, the chemo-thermal state of the system remains constant as the rays are traced through the cells. In the case of a single H II region, the speed of the ionisation front is limited to approximately $\lambda_{\text{mfp}}/dt_P$.

3.4.1 Minimizing neutral fraction change

Another strategy is restricting the neutral fraction to change a small amount, i.e. for a single cell,

$$dt_{P,\text{cell}} = \epsilon_{\text{ion}} \frac{n_{\text{HI}}}{|dn_{\text{HI}}/dt|} = \frac{\epsilon_{\text{ion}}}{|k_{\text{ph}} + n_e(C_{\text{H}} + \alpha_B)|}, \quad (27)$$

where ϵ_{ion} is the maximum fraction change in neutral fraction. Shapiro et al. (2004) found that this limited the speed of the ionisation front. We can investigate this further

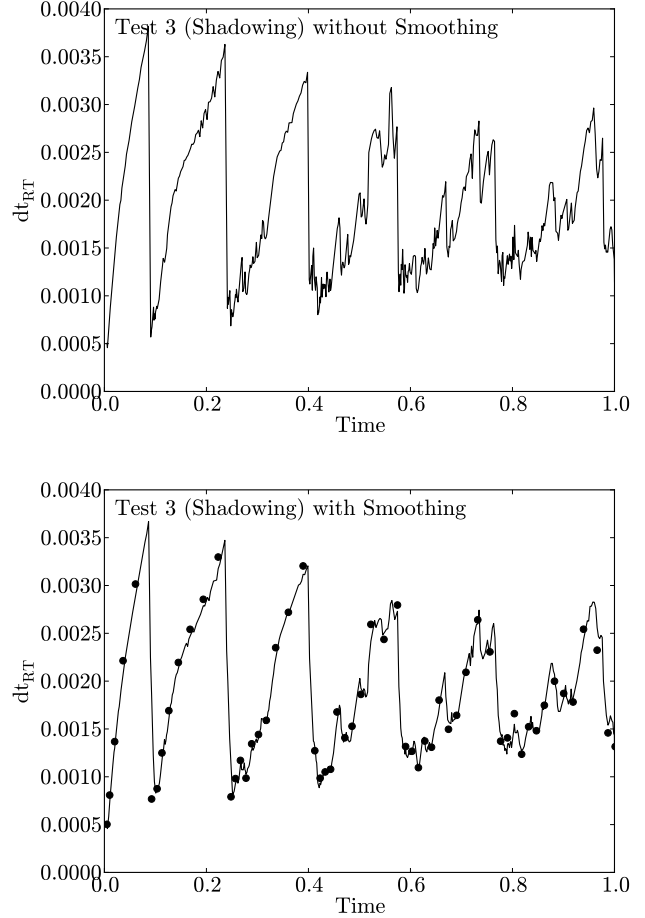


Figure 4. Radiative transfer adaptive timestep in shadowing test (Test 3; §4.3) while restricting the neutral fraction change to 5% in the ionisation front. The unmodified timestep (top) is slightly more noisy and the minima are more prominent than the timestep computed with a running average of the last two timesteps (bottom). The points show every tenth timestep taken into account for the running average. The sawtooth behavior is created by the ionisation front advancing into the next neutral cell in the over-density.

by evaluating the ionisation front velocity in a growing Strömgren sphere without recombinations,

$$\dot{N}_\gamma = 4\pi R^2 n_{\text{H}} v_{\text{IF}}. \quad (28)$$

Using $k_{\text{ph}} = \dot{N}_\gamma \sigma / 4\pi R^2 A_{\text{cell}}$ and $k_{\text{ph}} \propto \dot{n}_{\text{H}} / n_{\text{H}}$, we can make substitutions respectively on both sides of Equation (28) to arrive at the ionisation front velocity $v_{\text{IF}} \propto n_{\text{H}} / \dot{n}_{\text{H}}$.

We have implemented this method but we only consider cells within the ionisation front (by experiment we choose $\tau > 0.5$) because we are interested in evolving ionisation fronts at the correct speed. In the ionised region, the absolute changes in neutral fraction are small and will not significantly affect the ionisation front evolution. In other words, $n_{\text{HI}}/(dn_{\text{HI}}/dt)$ may be large but $(dn_{\text{HI}}/dt) \sim 0$, thus we can safely ignore these cells when determining the timestep without sacrificing accuracy.

We search for the cell with the smallest dt_P based on Equation 27. In principle, one could use this value without

modifications as the timestep, but there is considerable noise both spatially and temporally. In order to stabilise this technique, we first spatially smooth the values of $dt_{P,\text{cell}}$ with a Gaussian filter over a 3^3 cube. Because we only consider the cells within the ionisation front, we set $dt_{P,\text{cell}}$ to the hydrodynamical timestep outside the front during the smoothing. After we have smoothed $dt_{P,\text{cell}}$, we select the minimum value as dt_P . Significant noise in dt_P can exist between time steps as well. Because the solution can become inaccurate if the timestep is allowed to be too large, we restrict the next timestep to be less than twice the previous timestep,

$$dt_{P,1} = \min(2dt_{P,0}, dt_{P,1}). \quad (29)$$

Fig. 4 shows the smooth evolution of dt_P in a growing Strömgren sphere when compared to the values of $\min(dt_{P,\text{cell}})$.

3.4.2 Time averaged quantities within a timestep

Mellema et al. (2006) devised an iterative scheme that allows for large timesteps while retaining accuracy by considering the time-averaged values (τ , k_{ph} , n_e , n_{HI}) during the timestep. Starting with the cells closest to the source, they first calculate the column density to the cell. Then they compute the time-averaged neutral density for the cell and its associated optical depth, which is added to the total time-averaged optical depth. With these quantities, one can compute a photo-ionisation rate and update the electron density. This process is repeated until convergence is found in the neutral number density. In a test with a Strömgren sphere, they found analytical agreement with 10^{-3} less timesteps than a method without time-averaging. Another advantage of this method is the use of pre-calculated tables for the photo-ionisation rates as a function of optical depth, based on a given spectrum. This minimizes the energy groups needed to accurately sample a spectrum. We are currently implementing this method into ENZO+MORAY.

3.4.3 Physically motivated

A constant timestep is necessary when solving the time-dependent radiative transfer equation in ENZO+MORAY. It should be small enough to evolve ionisation fronts accurately, as discussed earlier. The timestep can be based on physical arguments, for example, the sound-crossing time of an ionised region at $T > 10^4$ K. To be conservative, one may choose the sound-crossing time of a cell (e.g. Abel et al. 2007; Wise & Abel 2008b). Alternatively, the diameter of the smallest relevant system (e.g., an accretion radius, transition radius to a D-type ionisation front, etc.) in the simulation may be chosen to calculate the sound-crossing time.

If the timestep is too large, the ionisation front will propagate too slowly, but it eventually approaches the correct radius at late times (see §7.4). This does not prevent one from using a large timestep, particularly if the system is not critically affected by a slower I-front velocity. One example is an expanding H II region in a power-law density gradient. After a brief, initial R-type phase, the I-front becomes D-type phase, where the ionisation and shock front progress jointly at the sound speed of the ionised region. A moderately large (0.1 Myr) timestep can accurately follow its evolution. However after the I-front passes a critical radius (Franco et al.

1990), the I-front detaches from the shock front, accelerates, and transitions back to an R-type front. This can also occur in champagne flows when the ionisation front passes a density discontinuity. The I-front velocities in these two stages differ up to a factor of ~ 10 . Although the solution is accurate with a large timestep in the D-type phase, the I-front may lag behind because of the constant timestep. After a few recombination times, the numerical solution eventually approaches the analytical solution. If such a simulation focuses on the density core expansion and any small scale structures, such as cometary structures and photo-dissociation regions, one can cautiously sacrifice temporal accuracy at large scales for computational savings.

3.4.4 Change of incident radiation

Ionisation front velocities can approach significant fractions of the speed of light in steep density gradients and in the early expansion of the H II region. If the ionisation front position is critical to the calculation, the radiation transport timestep can be derived from a non-relativistic estimate of the ionisation front velocity

$$v_{\text{IF}}(\mathbf{r}) \approx \frac{F(\mathbf{r})}{n_{\text{abs}}(\mathbf{r})}, \quad (30)$$

based on the incident radiation field at a particular position². Alternatively, the propagation of the ionisation front can be restricted by limiting the change in specific intensity I to a safety factor $C_{\text{RT},\text{cfl}}$, resulting in a timestep of

$$dt_P = C_{\text{RT},\text{cfl}} \frac{I}{|dI/dt|}. \quad (31)$$

We consider the specific intensity after the ray travels through the cell, so $I = I_0 \exp(-\tau)$, where $\tau = n_{\text{H}} \sigma dl$ is the optical depth through the cell. The time derivative of I is

$$\frac{dI}{dt} = I_0 \exp(-\tau) (-\dot{n}_{\text{H}} \sigma dl), \quad (32)$$

which can be expressed in terms of local optical depth and neutral fraction,

$$\frac{dI}{dt} = -I \frac{\tau \dot{n}_{\text{H}}}{n_{\text{H}}}. \quad (33)$$

\dot{n}_{H} is computed with the same formula as equation (27). Substituting in equation (31) gives

$$dt_P = C_{\text{RT},\text{cfl}} \frac{n_{\text{H}}}{\tau \dot{n}_{\text{H}}}. \quad (34)$$

In practice, we have found that a ceiling of 3 can be placed on the optical depth, so optically thick cells do not create a very small timestep. We still find excellent agreement with analytical solutions with this approximation. We show the accuracy using this timestep method in §7.4.

² See Shapiro et al. (2006) for the exact calculation of a relativistic ionisation front. Neglecting relativistic terms do not affect the solution because the front velocity is only considered in the timestep calculation.

3.5 Parallelisation Strategy

Parallelisation of the ray tracing code is essential when exploring problems that require high resolution and thus large memory requirements. Furthermore, ENZO is already parallelised and scalable to $O(10^2)$ processors in AMR simulations, and $O(10^3)$ in unigrid calculations. ENZO stores the AMR grid structure on every processor, but only one processor contains the actual grid and particle data and photon packages. All other processors contain an empty grid container. As discussed in *Step 4* in §3.1, we store the photon packages that need to be transferred to other grids in the linked list `PhotonMoveList`. In a single processor (serial) run, moving the rays is trivial by inserting these photons into the linked list of the destination grid. For multi-processor runs, we must send these photons through MPI communication to the processors that host the data of the destination grids. We describe our strategy below.

The easiest case is when the destination grid exists on the same processor as the source grid, where we move the ray as in the serial case. For all other rays, we organise the rays by destination processors and send them in groups. We also send the destination grid level and ID number along with the ray information that is listed at the beginning of §3.1.

For maximum overlap of communication and computation, which enables scaling to large numbers of processors, we must employ “non-blocking” MPI communication, where each processor does not wait for synchronisation with other processors. We use this technique for the sending and receiving of rays. Here we desire to minimize the idle time of each processor when it is waiting to receive data. In the loop shown in Fig. 2 with the conditional that checks whether we have traced all of the rays, we aggressively transport rays that are local on the processor, and process any MPI receive calls as they arrive, not waiting for their completion in order to continue to the next iteration. We describe the steps in this algorithm next.

Step 1.– Before any communication occurs, we count the number of rays that will be sent to each processor. The MPI receive calls (`MPI_Irecv`) must have a data buffer that is greater than or equal to the size of the message. We choose to send a maximum of N_{\max} ($= 10^5$ in ENZO v2.0) rays per MPI message. Therefore, we allocate a buffer of this size for each `MPI_Irecv` call. We then determine the number of MPI messages N_{mesg} and send this number in a non-blocking fashion, i.e. `MPI_Isend`.

Step 2.– Pack the photon packages into a contiguous array for MPI communication while the messages from *Step 1* completes.

Step 3.– Process the number of photon messages that we are expecting from each processor, sent in *Step 1*. Then post this number of `MPI_Irecv` calls for the photon data. Because we strive to make the ray tracing routine to be totally non-blocking, the processors will most likely not be synchronised on the same loop (Steps 3–5 in §3.1). Therefore, there might be additional N_{mesg} MPI messages waiting to be processed. We check for these messages and aggressively drain the message stack to determine the total number of photon messages that we are expecting and post their associated `MPI_Irecv` calls for the photon data.

Step 4.– Send the grouped photon data with `MPI_Isend` with a maximum size of N_{\max} photons.

Step 5.– Place any received photon data into the destination grids. We monitor whether the processor has any rays that were moved to grids on the same processor. If so, this processor has rays to transport, and we do not necessarily have to wait for any MPI receive messages and thus use `MPI_Testsome` to receive any messages that have already arrived. If not, we call `MPI_Waitsome` to wait for any MPI receive messages.

Step 6.– If all processors have exhausted their workload, then all rays have been either absorbed, exited the domain, or halted after travelling a distance cdt_P . We check this in a similar non-blocking manner as the N_{mesg} calls in *Step 1*.

Lastly we have experimented with a hybrid OpenMP/MPI version of ENZO, where workload is partitioned over grids on each MPI process. We found that parallelisation over grids for the photon transport does not scale well, and threading over the rays in each grid is a better approach. Because the rays are stored in a linked list in each grid, we must manually split the list into separate lists and let each thread work on each list.

4 RADIATIVE TRANSFER TESTS

Tests plays an important role in creating and maintaining computational tools. In this section, we present tests drawn from the Cosmological Radiative Transfer Codes Comparison Project (Iliev et al. 2006), where results from 11 different radiative transfer codes compared results in four test problems. The codes use various methods for radiation transport: ray tracing with short, long, and hybrid characteristics, Monte Carlo casting; ionisation front tracking (Alvarez et al. 2006b); variable Eddington Tensor formalism (Gnedin & Abel 2001). They conducted tests that investigated (1) the growth of a single Strömgren sphere enforcing isothermal conditions, (2) the same test with an evolving temperature field, (3) shadowing created by a dense, optically thick clump, and (4) multiple H II regions in a cosmological density field. In all of the tests presented here, we use the method of restricted neutral fraction changes (§3.4.1) for choosing a radiative transfer timestep. We cast 48 rays (HEALPix level 1) from the point source and require a sampling of at least $\Phi_c = 5.1$ rays per cell.

4.1 Test 1. Pure hydrogen isothermal H II region expansion

The expansion of an ionising region with a central source in a uniform medium is a classic problem first studied by Strömgren (1939). This simple but useful test can uncover any asymmetries or artifacts that may arise from deficiencies in the method or newly introduced bugs in the development process. In this problem, the ionised region grows until recombinations balance photo-ionisations [equation (1)]. The evolution of the radius r_s and velocity v_s of the ionisation front has an exact solution of

$$r_s(t) = R_s [1 - \exp(-t/t_{\text{rec}})]^{1/3}, \quad (35)$$

$$v_s(t) = \frac{R_s}{3t_{\text{rec}}} \frac{\exp(-t/t_{\text{rec}})}{[1 - \exp(-t/t_{\text{rec}})]^{2/3}}, \quad (36)$$

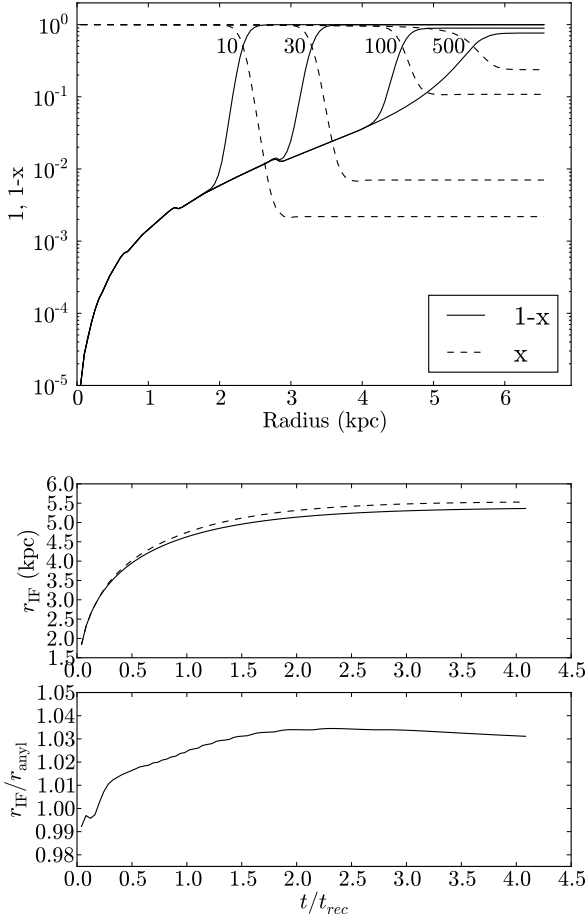


Figure 5. Test 1 (H II region expansion with a monochromatic spectrum of 13.6 eV). Top: Radially averaged profile of neutral fraction (solid) and ionised (dashed) fraction at 10, 30, 100, and 500 Myr. Bottom: Evolution of the calculated (top, dashed) and analytical (top, solid) Strömgren radius. The ratio of these radii are plotted in the bottom panel.

where $t_{\text{rec}} = (\alpha_B n_H)^{-1}$ is the recombination time.

We adopt the problem parameters used in RT06. The ionising source emits 5×10^{48} ph s $^{-1}$ of monochromatic radiation at 13.6 eV and is located at the origin in a simulation box of 6.6 kpc. The ambient medium is initially set at $T = 10^4$ K, $n_H = 10^{-3}$ cm $^{-3}$, $x = 1.2 \times 10^{-3}$, resulting in $R_s = 5.4$ kpc and $t_{\text{rec}} = 122.4$ Myr. The problem is run for 500 Myr. In the original tests, the temperature is fixed at 10^4 K; however, our solver is inherently tied to the chemistry and energy solver. To mimic an isothermal behavior, we set the adiabatic index $\gamma = 1.0001$, which ensures an isothermal state but not a fixed ionisation fraction outside of the Strömgren sphere.

In Fig. 5, we show (a) the evolution of the neutral and ionisation fraction as a function of radius at $t = 10, 30, 100,$ and 500 Myr, and (b) the growth of the ionisation front radius as a function of time and its ratio with the analytical Strömgren radius [equation (35)]. The ionisation front has a width of ~ 0.7 kpc, which is in agreement with the inherent thickness of $\sim 18\lambda_{\text{mfp}} = 0.74$ kpc, given a 13.6 eV monochromatic spectrum. There are small kinks in the neutral

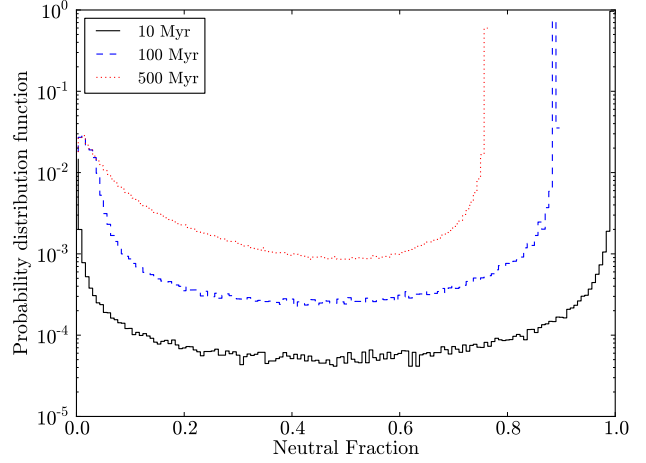


Figure 6. Test 1 (H II region expansion with a monochromatic spectrum of 13.6 eV). Probability distribution function for neutral fraction at 10 Myr (solid), 100 Myr (dashed), and 500 Myr (dotted). Recombination of hydrogen at $T = 10^4$ K causes the maximum neutral fraction to decrease from 1 to 0.75.

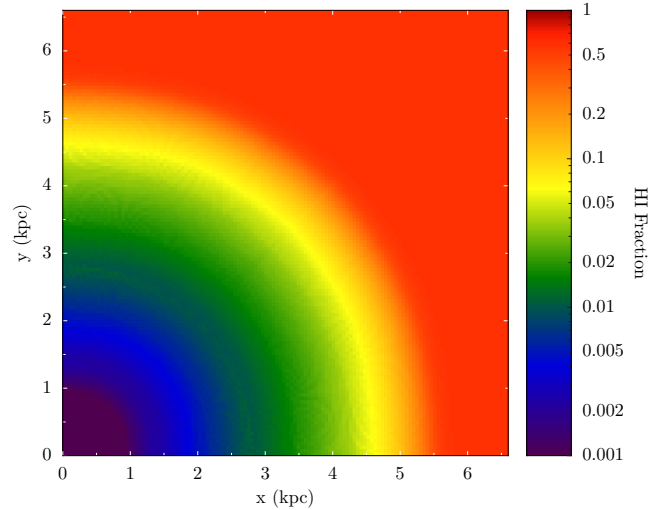


Figure 7. Test 1 (H II region expansion with a monochromatic spectrum of 13.6 eV). Slice of neutral fraction at the origin at 500 Myr.

fraction at 1.5 and 3 kpc that corresponds to artifacts created by the photon package splitting at these radii. However these do not affect the overall solution. One difference between our results and the codes presented in RT06 is the increasing neutral fraction outside of the H II region. This occurs because the initial ionised fraction and temperature is set to 1.2×10^{-3} and 10^4 K, which are not the equilibrium values. Over the 500 Myr in the calculation, the neutral fraction increases to 0.2, which is close to its equilibrium value. In the right panel of Fig. 5, the ionisation front radius exceeds R_s by a few percent for most of the calculation. This difference happens because the analytical solution [equation (35)] assumes the H II region has a constant ionised fraction. The evolution of the ionised fraction as a function of radius can be analytically calculated (e.g. Osterbrock 1989; Petkova & Springel 2009), causing the ionisation front ra-

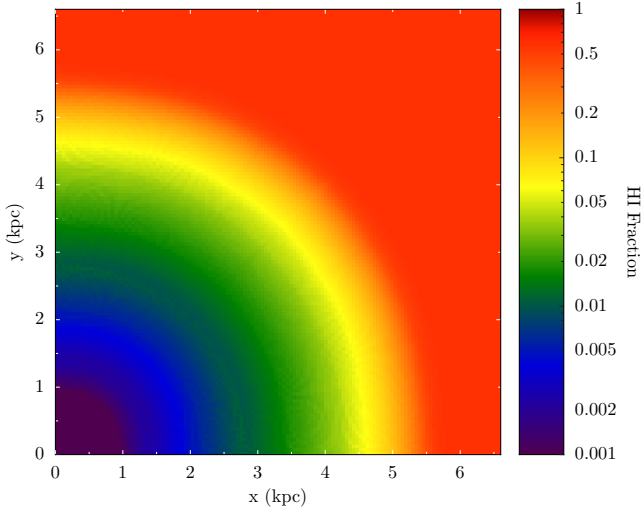


Figure 8. Test 2. (H II region expansion with a $T = 10^5$ K blackbody spectrum). Radially averaged profile of neutral (solid) and ionized (dashed) fraction at 10, 30, 100, and 500 Myr.

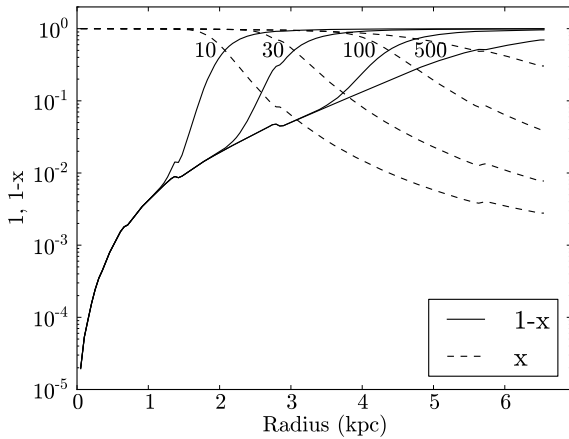


Figure 9. Test 2. (H II region expansion with a $T = 10^5$ K blackbody spectrum). Evolution of the average neutral fraction.

dus to be slightly larger, increasing from 0 to 3% in the interval 80–350 Myr. Our results are in excellent agreement with this more accurate analytical solution. We show the distribution of neutral fraction in the domain for $t = 10$, 100, and 500 Myr in Fig. 6 that agrees well with the results in RT06. In Fig. 7, we show a slice of the neutral fraction through the origin. Other than the ray splitting artifacts that generate the plateaus at 1.5 and 3 kpc, one sees spherical symmetry without any noise in our solution.

4.2 Test 2. H II region expansion: temperature evolution

This test is similar to Test 1, but the temperature is allowed to evolve. The radiation source now has a blackbody spectrum with a $T = 10^5$ K. The initial temperature is set at 100 K. The higher energy photons have a longer mean free path than the photons at the ionisation threshold in

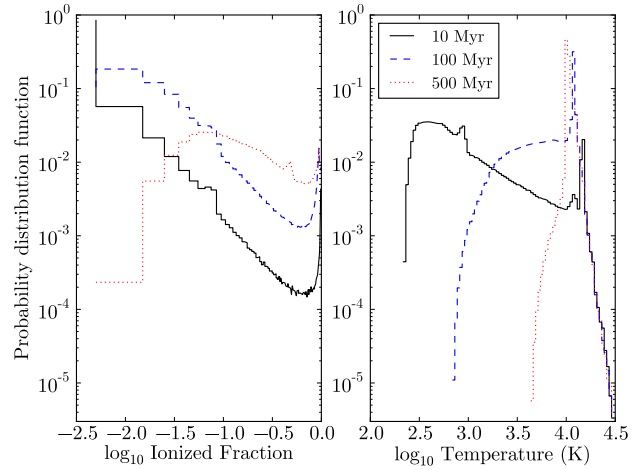


Figure 10. Test 2. (H II region expansion with a $T = 10^5$ K blackbody spectrum). Probability distribution function for ionized fraction (left) and temperature (right) at 10 Myr (solid), 100 Myr (dashed), and 500 Myr (dotted).

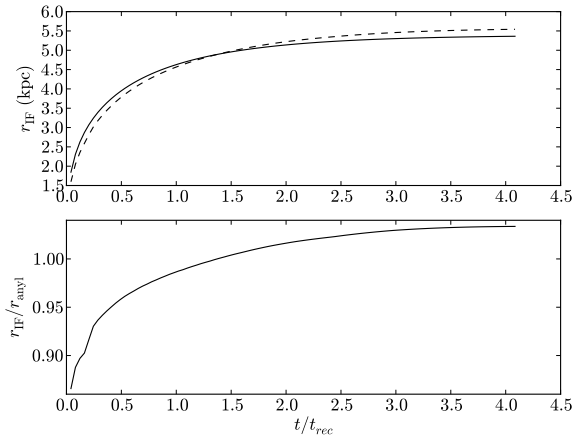


Figure 12. Test 2. (H II region expansion with a $T = 10^5$ K blackbody spectrum). Top: Evolution of the radius of the simulated ionisation front (dashed) and analytical (solid) Strömgren radius. Bottom: The ratio of the calculated and analytical Strömgren radius.

Test 1. Thus the ionisation front is thicker as the photons can penetrate deeper into the neutral medium. Here we use 4 energy groups with the following mean energies and relative luminosities: $E_i = (16.74, 24.65, 34.49, 52.06)$, $L_i/L = (0.277, 0.335, 0.2, 0.188)$.

In Fig. 8, we show the radially averaged neutral and ionized fraction at $t = 10$, 30, 100, and 500 Myr, and the total neutral fraction of the domain in Fig. 9. Compared with Test 1, the ionisation front is thicker, as expected with the harder spectrum. Artifacts originating from ray splitting, similar to Test 1, appear at $r \sim 1$ and 3 kpc as kinks in the neutral fraction. The total neutral fraction decreases to 0.67 over $4t_{\text{rec}} = 500$ Myr, which is in agreement with the analytical expectation and other codes in RT06. Fig. 10 shows the distribution of ionized fraction and temperature in Test 2. The overall trends agree with the codes presented

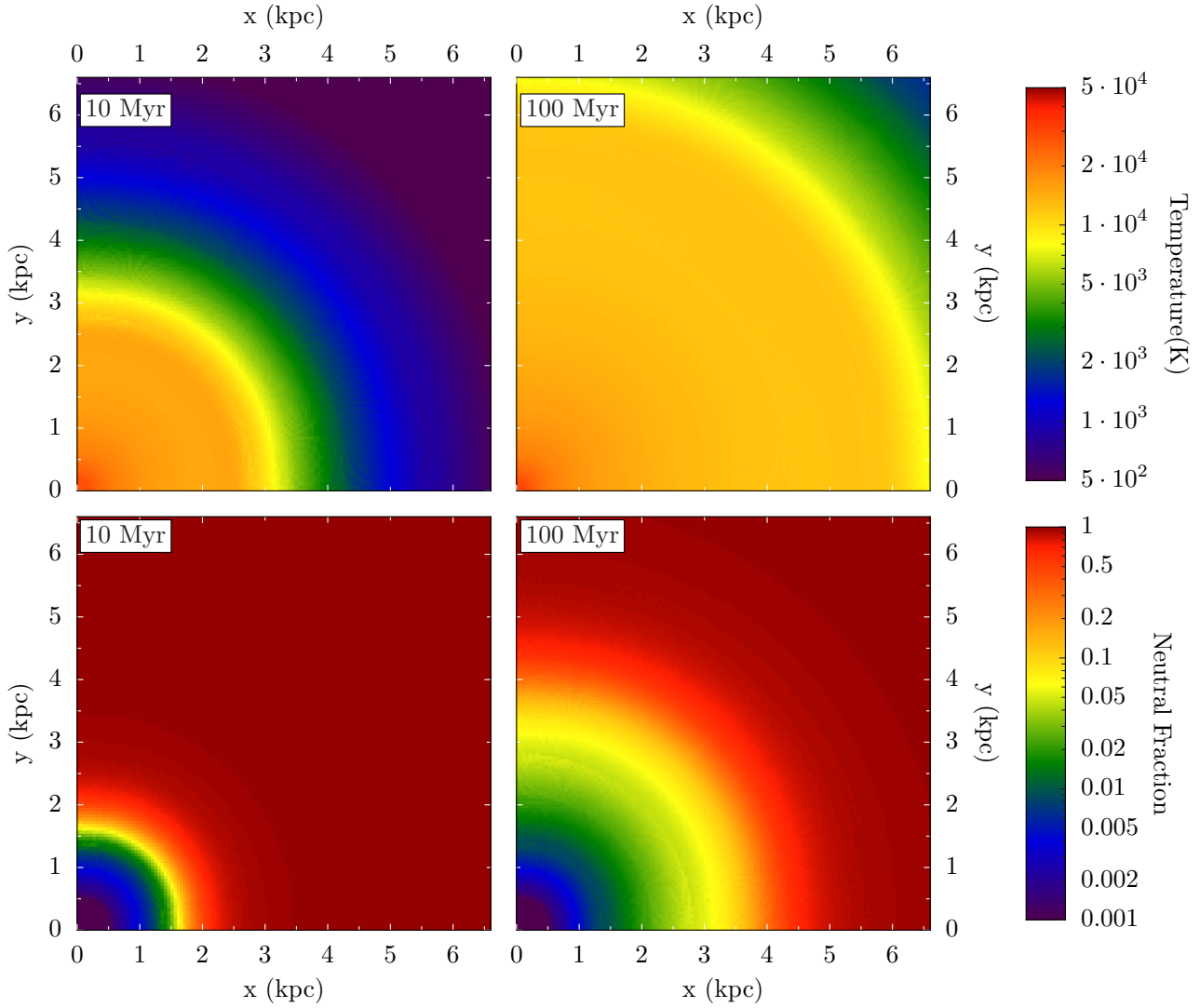


Figure 11. Test 2. (H II region expansion with a $T = 10^5$ K blackbody spectrum). Top: Slices through the origin of neutral fraction at 10 and 100 Myr. Bottom: Slices of temperature at 10 and 100 Myr.

in RT06 with the exception of the ray splitting artifacts that appear as slight rises in the distribution at $\log x_e \sim -1$ and $\log T \sim 3$. In Fig. 11, we show slices of neutral fraction and temperature through the origin at $t = 10$ and 100 Myr. Here one sees the spherically symmetric H II regions and a smooth temperature transition to the neutral ambient medium. In Fig. 12, we show the ratio of the ionisation front radius r_{IF} in our simulation and R_s . Before $1.5t_{\text{rec}}$, r_{IF} lags behind R_s , initially by 10% and then increases to R_s ; however afterwards, this ratio asymptotes to a solution that is 4% greater than R_s . This behavior is approximately the median result in RT06, where this ratio varies between 1 and 1.1, and the early evolution of r_{IF} is under-predicted by almost all of the codes. If we use one energy group with the mean energy (29.6 eV) of a $T = 10^5$ K blackbody, we find that $r_{\text{IF}}/R_s = 1.08$, which is representative of the codes in the upper range of RT06.

4.3 Test 3. I-front trapping in a dense clump and the formation of a shadow

The diffusivity and angular resolution of a radiative transport method can be tested with the trapping of an ionisation front by a dense, neutral clump. In this situation, the ionisation front will uniformly propagate until it reaches the clump surface. Then the radiation in the line of sight of the clump will be absorbed more than the ambient medium. If the clump is optically thick, a shadow will form behind the clump. The sharpness of the ionisation front at the shadow surface can be used to determine the diffusivity of the method. Furthermore the shadow surface should be aligned with the outermost neutral regions of the clump, which can visually assess the angular resolution of the method.

The problem for this test is contained in a 6.6 kpc box with an ambient medium of $n_H = 2 \times 10^{-4} \text{ cm}^{-3}$ and $T = 8000$ K. The clump is in pressure equilibrium with $n_H = 0.04 \text{ cm}^{-3}$ and $T = 40$ K. It has a radius of $r_c = 0.8$ kpc and is centred at $(x, y, z) = (5, 3.3, 3.3)$ kpc. The ionized fraction of the entire domain is zero. In RT06, the test considered a

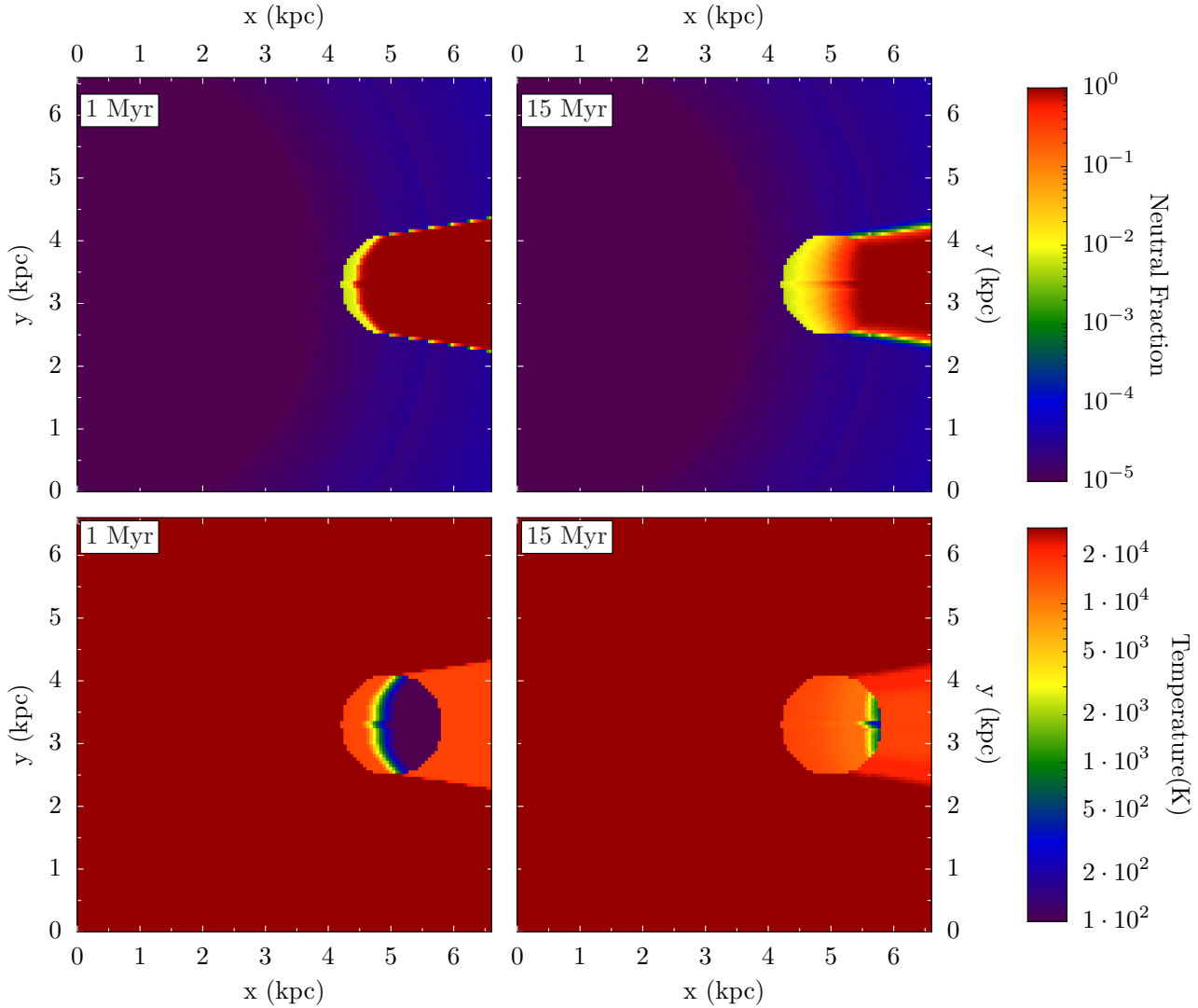


Figure 16. Test 3. (I-front trapping in a dense clump and shadowing). Clockwise from upper left: Slices through the origin of neutral fraction (1 Myr), temperature (1 Myr), temperature (15 Myr), and neutral fraction (15 Myr).

plane parallel radiation field with a flux $F_0 = 10^6 \text{ ph s}^{-1} \text{ cm}^{-2}$ originating from the $y = 0$ plane. Our code can only consider point sources, so we use a single radiation source located in the centre of the $y = 0$ boundary. The luminosity of $\dot{N}_\gamma = 3 \times 10^{51} \text{ ph s}^{-1}$ corresponds to the same flux F_0 at 5 kpc. The location where the ionisation front trapping can be calculated analytically (Shapiro et al. 2004), and with these parameters, it should halt at approximately the centre of the clump. We use the same four energy groups as in Test 2.

In Fig. 13, we show neutral fraction and temperature of a one-dimensional cut through the centre of the dense clump at $z = 0.5$ at $t = 1, 3, 5, 15$ Myr. The ionisation front is halted at a little more than halfway through the clump, which is consistent with the analytical expectation. The hardness of the $T = 10^5$ K blackbody spectrum allows the gas outside of the ionisation front to be photo-heated. Where the gas is ionised, the temperature is between 10,000 and 20,000 K, but decreases sharply with the ionised fraction. Fig. 14 depicts the average ionised fraction and tem-

perature inside the dense clump, which both gradually increase as the ionisation front propagates through the overdensity. Our results are consistent with RT06. The distribution of ionized fraction and temperature within the clump are shown in Fig. 15 and agree well with the other codes in RT06. Finally we show slices of neutral fraction and temperature in the $z = 0.5$ plane in Fig. 16. The neutral fraction slices prominently show the sharp shadows created by the clump and demonstrates the non-diffusivity behavior of ray tracing. The discretisation of the sphere creates one neutral cell on the left side of the sphere. This inherent artifact to the initial setup carries through the calculation. We did not smooth the clump surface like in some of the RT06 codes, in order to remove this artifact. It is seen in the neutral fraction and temperature states at all times and is not caused by our ray tracing algorithm.

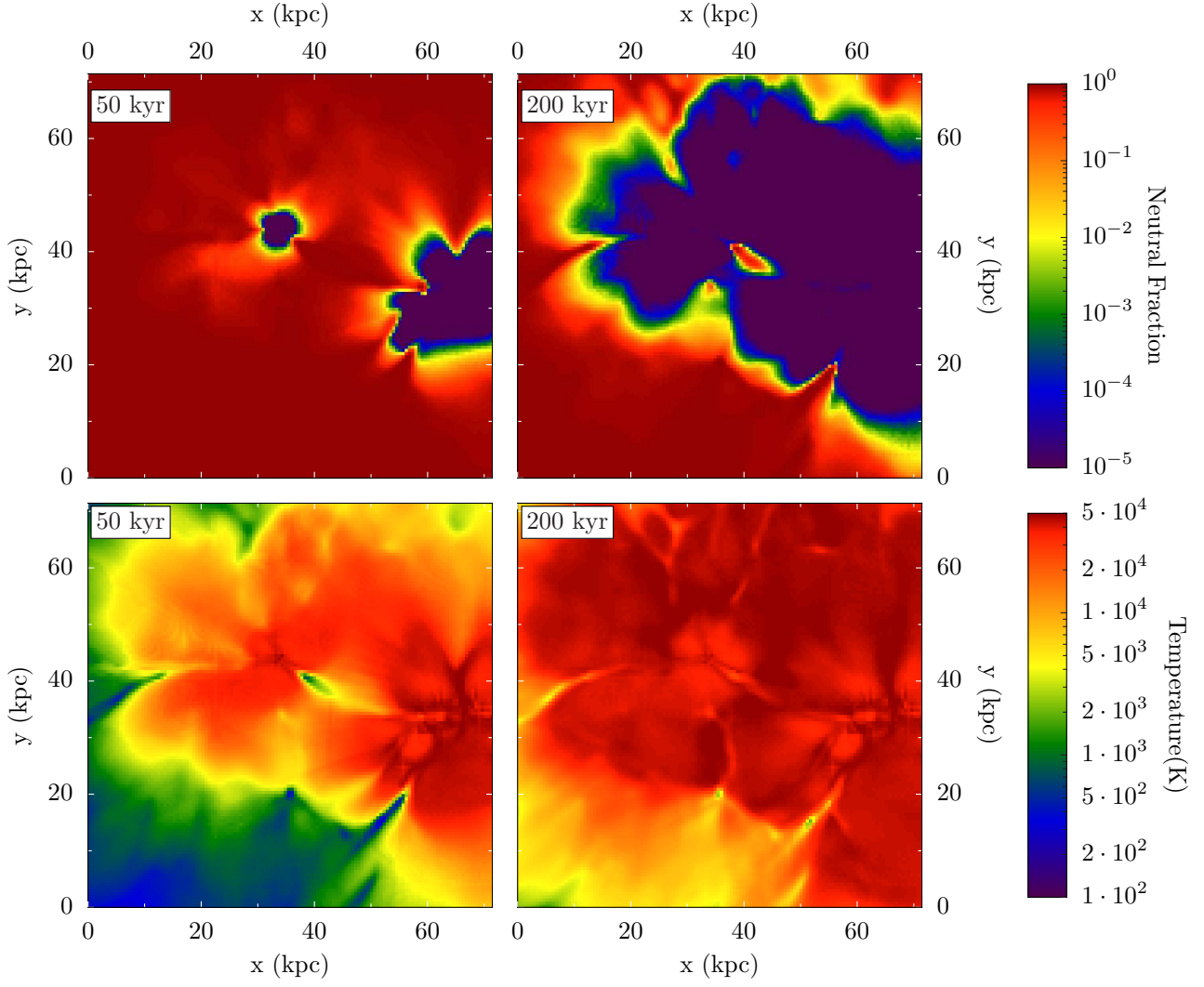


Figure 19. Test 4. (Multiple cosmological sources). Top: Slices through the origin of neutral fraction at 50 and 200 kyr at the coordinate $z = z_{\text{box}}/2$. Bottom: Slices of temperature at 50 and 200 kyr. No smoothing has been applied to the images.

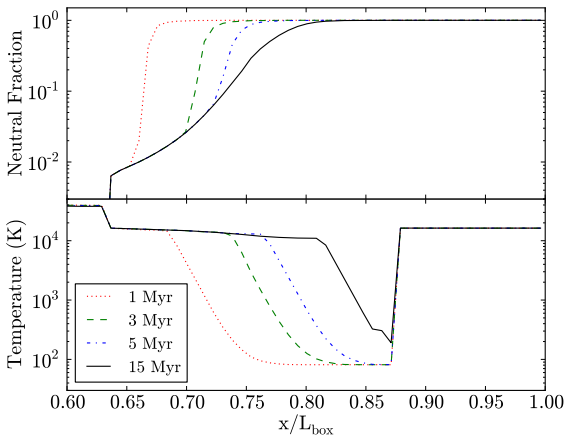


Figure 13. Test 3. (I-front trapping in a dense clump and shadowing). Line cut from the point source through the middle of the dense clump at $t = 1, 3, 5, 15$ Myr. of the average neutral fraction (top) and temperature (bottom) of the clump.

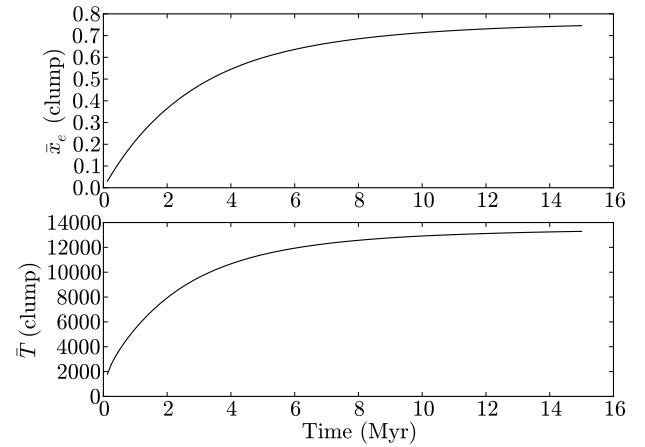


Figure 14. Test 3. (I-front trapping in a dense clump and shadowing). Evolution of the average ionised fraction (top) and temperature (bottom) of the overdense clump.

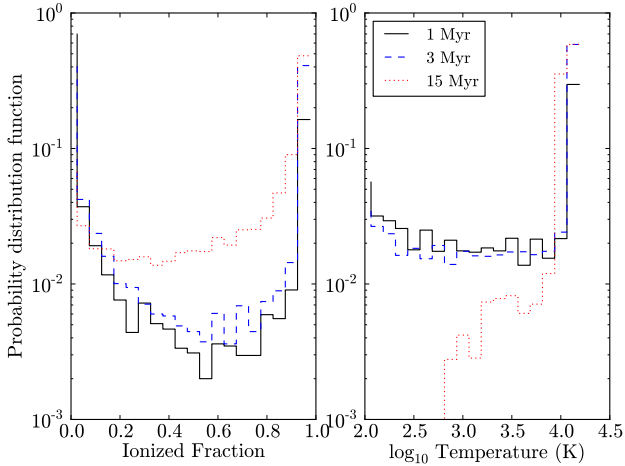


Figure 15. Test 3. (I-front trapping in a dense clump and shadowing). Probability distribution function for ionized fraction (left) and temperature (right) at 1 Myr (solid), 3 Myr (dashed), and 15 Myr (dotted) within the dense clump.

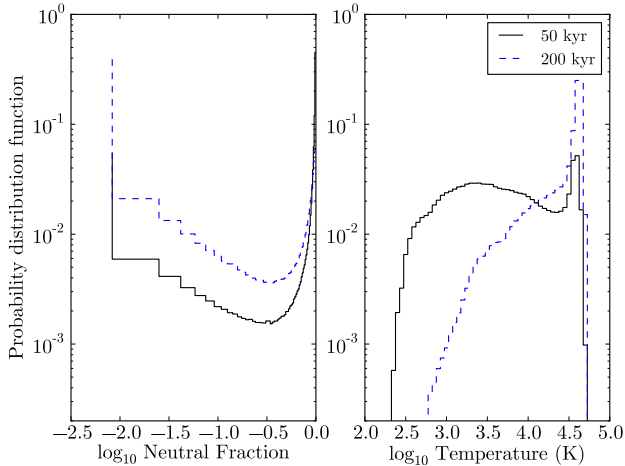


Figure 17. Test 4. (Multiple cosmological sources). Probability distribution function for neutral fraction (left) and temperature (right) at 50 kyr (solid) and 200 kyr (dashed).

4.4 Test 4. Multiple sources in a cosmological density field

The last test in RT06 involves a static cosmological density field at $z = 9$. The simulation comoving box size is $0.5 h^{-1}$ Mpc and has a resolution of 128^3 . There are 16 point sources that are centred in the 16 most massive haloes. They emit $f_\gamma = 250$ ionising photons per baryon in a blackbody spectrum with an effective temperature $T = 10^5$ K, and they live for $t_s = 3$ Myr. Thus the luminosity of each source is

$$\dot{N}_\gamma = f_\gamma \frac{M\Omega_b}{\Omega_m m_H t_s}, \quad (37)$$

where M is the halo mass, $\Omega_m = 0.27$, and $\Omega_b = 0.043$. The radiation boundaries are isolated so that the radiation leaves the box instead being shifted periodically. The simulation is evolved for 0.4 Myr.

Fig. 17 depicts the distribution of the neutral fraction and temperature of the entire domain and shows good

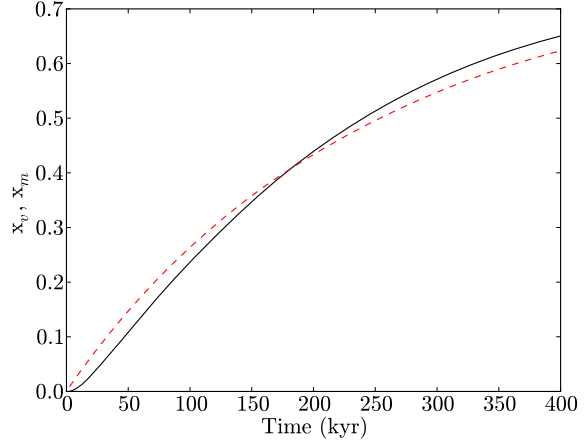


Figure 18. Test 4. (Multiple cosmological sources). Evolution of the mass- (dashed) and volume-averaged (solid) ionised fraction.

agreement with the codes presented in RT06. We show the growth of the H II regions by computing the mass-averaged x_m and volume-averaged x_v ionised fraction in Fig. 18. Initially x_m is larger than x_v , and at $t \sim 170$ kyr, the x_v becomes larger. This is indicative of inside-out reionisation (e.g. Gnedin 2000; Miralda-Escudé et al. 2000; Sokasian et al. 2003), where the dense regions around haloes are ionised first, then the voids are ionised last. At the end of the simulation, 65% of the simulation is ionised. However by visual inspection in the slices of electron fraction (Fig. 19), there appears to be very good agreement with C²-ray and FTTE. By first glance, our result appears to be different than the RT06 because of the color-mapping. Our results are also in good agreement with the multi-frequency version of TRAPHIC (Pawlik & Schaye 2010, see also for better representations of the electron fraction slices). In the slices of electron fraction and temperature, Fig. 19, the photo-heated regions are larger than the ionised regions by a factor of 2–3 because of the hardness of the $T = 10^5$ K blackbody spectrum.

5 RADIATION HYDRODYNAMICS TESTS

We next show results from radiation hydrodynamics test problems presented in Iliev et al. (2009, hereafter RT09). They involve (1) the expansion of an H II region in a uniform medium, similar to Test 2, (2) an H II region in an isothermal sphere, and (3) the photo-evaporation of a dense, cold clump, similar to Test 3. We turn off self-gravity and AMR in accordance with RT09.

5.1 Test 5. Classical H II region expansion

Here we consider the expansion of an H II region into a uniform neutral medium including the hydrodynamical response to the heated gas. The ionised region has a greater pressure than the ambient medium, causing it to expand. This is a well-studied problem (Spitzer 1978) with an analytical solution, where the ionisation front moves as

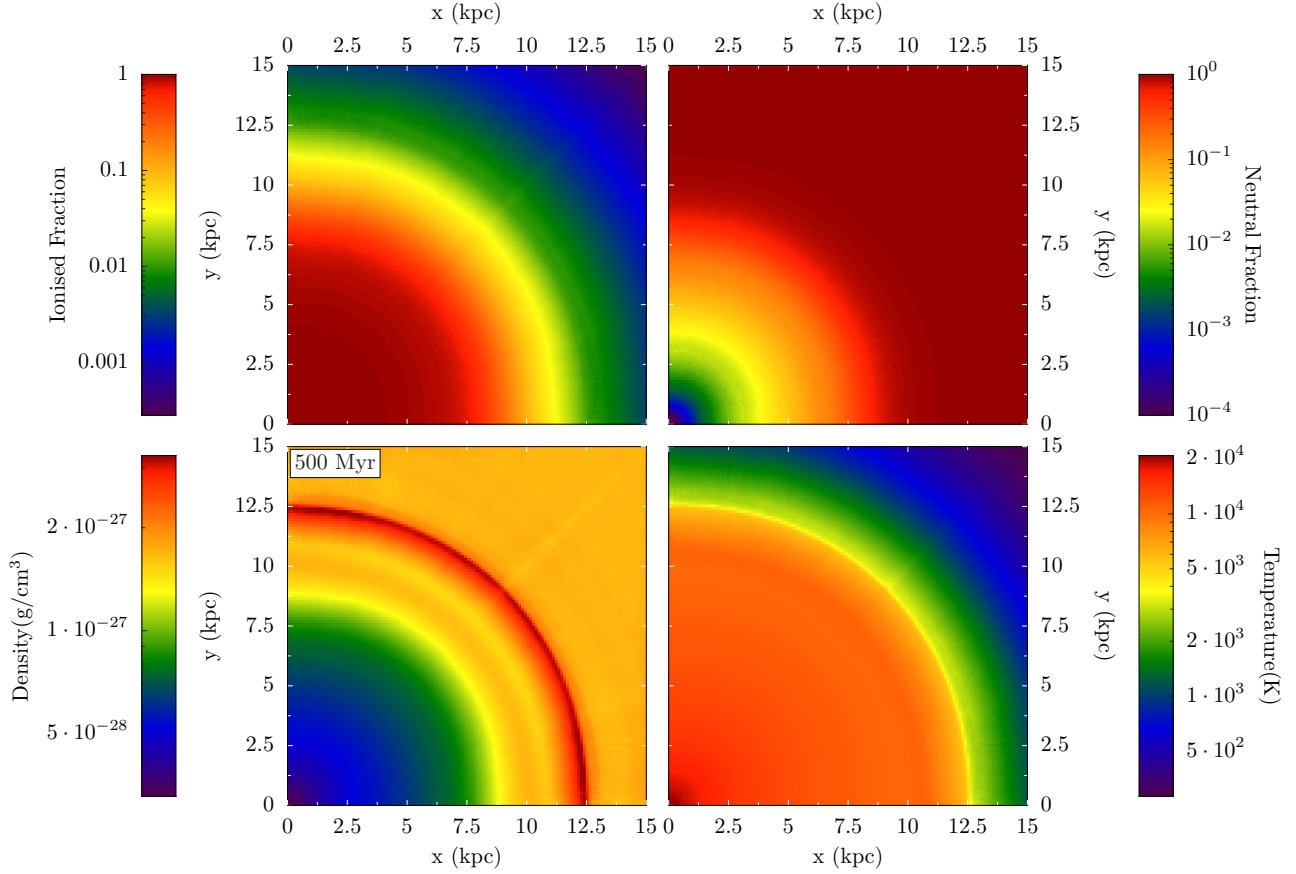


Figure 22. Test 5. (H II region in a uniform medium). Clockwise from the upper left: Slices through the origin of ionised fraction, neutral fraction, temperature, and density at time $t = 500$ Myr.

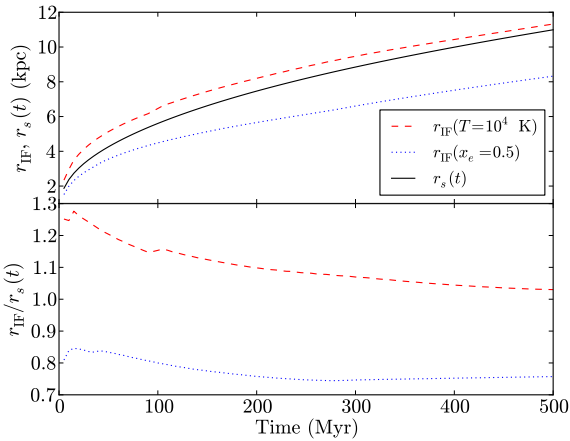


Figure 20. Test 5. (H II region in a uniform medium). Top: Growth of the computed ionisation front radius at an ionised fraction $x_e = 0.5$ (dashed) and at a temperature $T = 10^4$ K (dotted) compared to the analytical estimate [solid; equation (38)]. Bottom: The ratio of the computed ionisation front radii to the analytical estimate.

$$r_s(t) = r_{s,0} \left(1 + \frac{7c_s}{4R_s} \right)^{4/7}, \quad (38)$$

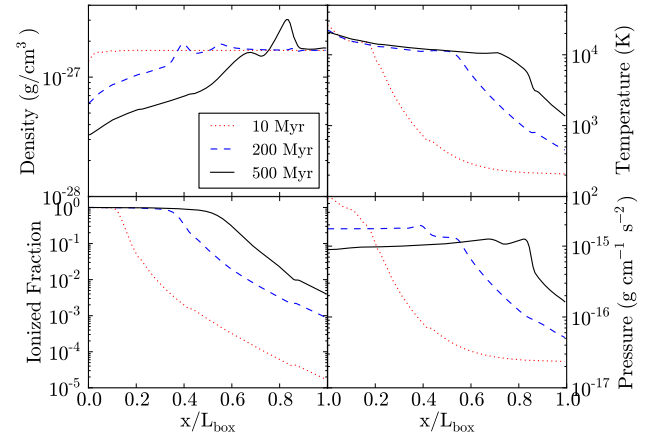


Figure 21. Test 5. (H II region in a uniform medium). Clockwise from the upper left: Radial profiles of density, temperature, ionised fraction, and pressure at times $t = 10, 200$, and 500 Myr.

where c_s is the sound speed of the ionised gas and $r_{s,0}$ is the r_s in Equation 35. The bubble eventually reaches pressure equilibrium with the ambient medium at a radius

$$r_f = R_s \left(\frac{2T}{T_0} \right)^{2/3}, \quad (39)$$

where T and T_0 are the ionised and ambient temperatures, respectively. These solutions only describe the evolution at late times, and not the fast transition from R-type to D-type at early times.

The simulation setup is similar to Test 2 with the exception of the domain size $L = 15$ kpc. Here pressure equilibrium occurs at $r_f = 185$ kpc, which is not captured by this test. However more interestingly, the transition from R-type to D-type is captured and occurs around $R_s = 5.4$ kpc. The test is run for 500 Myr.

The growth of the ionisation front radius is shown in Fig. 20, using both $T = 10^4$ K and $x_e = 0.5$ as ionisation front definitions, compared to the analytical solution [equation (39)]. We define this alternative measure because the ionisation front becomes broad as the D-type front creates a shock. Densities in this shock, as seen in Fig. 21, are high enough for the gas to recombine but not radiatively cool. Before $2t_{\text{rec}} \approx 250$ Myr, the temperature cutoff overestimates r_s by over 10%; however at later times, it provides a good match to the $t^{4/7}$ growth at late times. With the $x_e = 0.5$ criterion for the ionisation front, the radius is always underestimated by $\sim 20\%$. This behavior was also seen in RT09.

Fig. 21 shows the progression of the ionisation front at times $t = 10, 200$, and 500 Myr in radial profiles of density, temperature, pressure, and ionised fraction. The initial H II region is over-pressurised and creates an forward shock wave. The high-energy photons can penetrate through the shock and partially ionises and heats the exterior gas, clearly seen in the profiles. As noted in RT09, this heated exterior gas creates an photo-evaporative flow that flows inward. This interacts with the primary shock and creates the double-peaked features in the density profiles at 200 and 500 Myr. Fig. 22 shows slices through the origin of the same quantities, including neutral fraction. These depict the very good spherical symmetry of our method. The only apparent artifact is a very slight diagonal line, which is caused by the HEALPix pixelisation differences between the polar and equatorial regions. This artifact diminishes as the ray-to-cell sampling is increased.

5.2 Test 6. H II region expansion in an isothermal sphere

A more physically motivated scenario is an isothermal sphere with a constant density n_c core, which is applicable to collapsing molecular clouds and cosmological haloes. The radial density profile is described by

$$n(r) = \begin{cases} n_c & (r \leq r_0) \\ n_c(r/r_0)^{-2} & (r > r_0) \end{cases}, \quad (40)$$

where r_0 is the radius of the core. If the Strömgren radius is smaller than the core radius, then the resulting H II region never escapes into the steep density slope. When the ionisation front propagates out of the core, it accelerates as it travels down the density gradient. There exists no analytical solution for this problem with full gas dynamics but was extensively studied by Franco et al. (1990). After the gas is ionised and photo-heated, the density gradient provides the pressure imbalance to drive the gas outwards.

This test is constructed to study the transition from R-type to D-type in the core and back to R-type in the density gradient. Thus the simulation focuses on small-scale,

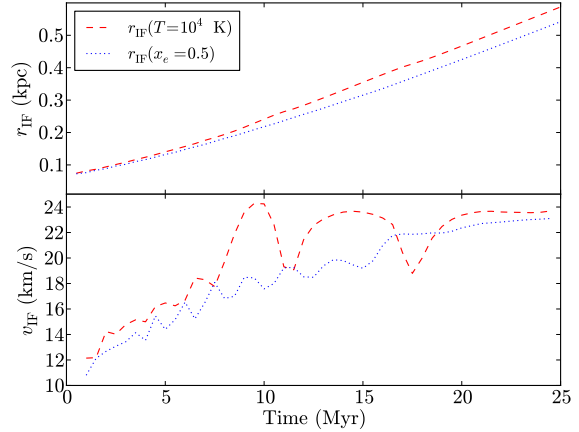


Figure 23. Test 6. (H II region in a $1/r^2$ density profile). Top: Growth of the computed ionisation front radius as $T = 10^4$ K and $x_e = 0.5$ as definitions for the front. Bottom: Velocity of the ionisation front, computed from outputs at 0.5 Myr intervals. The velocity is calculated from r_{IF} , whose coarse time resolution causes the noise seen in v_{IF} . It is smooth within the calculation itself.

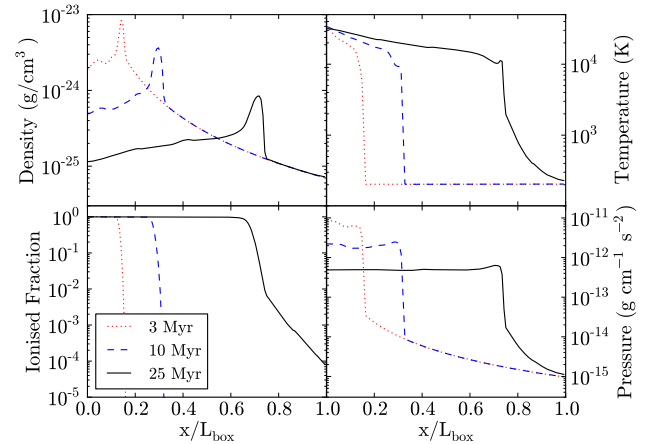


Figure 24. Test 6. (H II region in a $1/r^2$ density profile). Clockwise from the upper left: Radial profiles of density, temperature, ionised fraction, and pressure at times $t = 3, 10$, and 25 Myr.

not long term, behavior of the ionisation front. The simulation box has a side length $L = 0.8$ kpc with core density $n_0 = 3.2 \text{ cm}^{-3}$, core radius $r_0 = 91.5$ pc (15 cells), and temperature $T = 100$ K throughout the box. The ionisation fraction is initially zero, and the point source is located at the origin with a luminosity of $10^{50} \text{ ph s}^{-1} \text{ cm}^{-3}$. The simulation is run for 75 Myr.

Because this problem does not have an analytical solution, we compare our calculated ionisation front radius and velocity, shown in Fig. 23, to the RT09 results. Their evolution are in agreement within 5% of RT09. As in Test 5, we use an extra definition of $T = 10^4$ K for the ionisation front. We compute the ionisation front velocity from the radii at 50 outputs, which causes the noise seen Fig. 23.

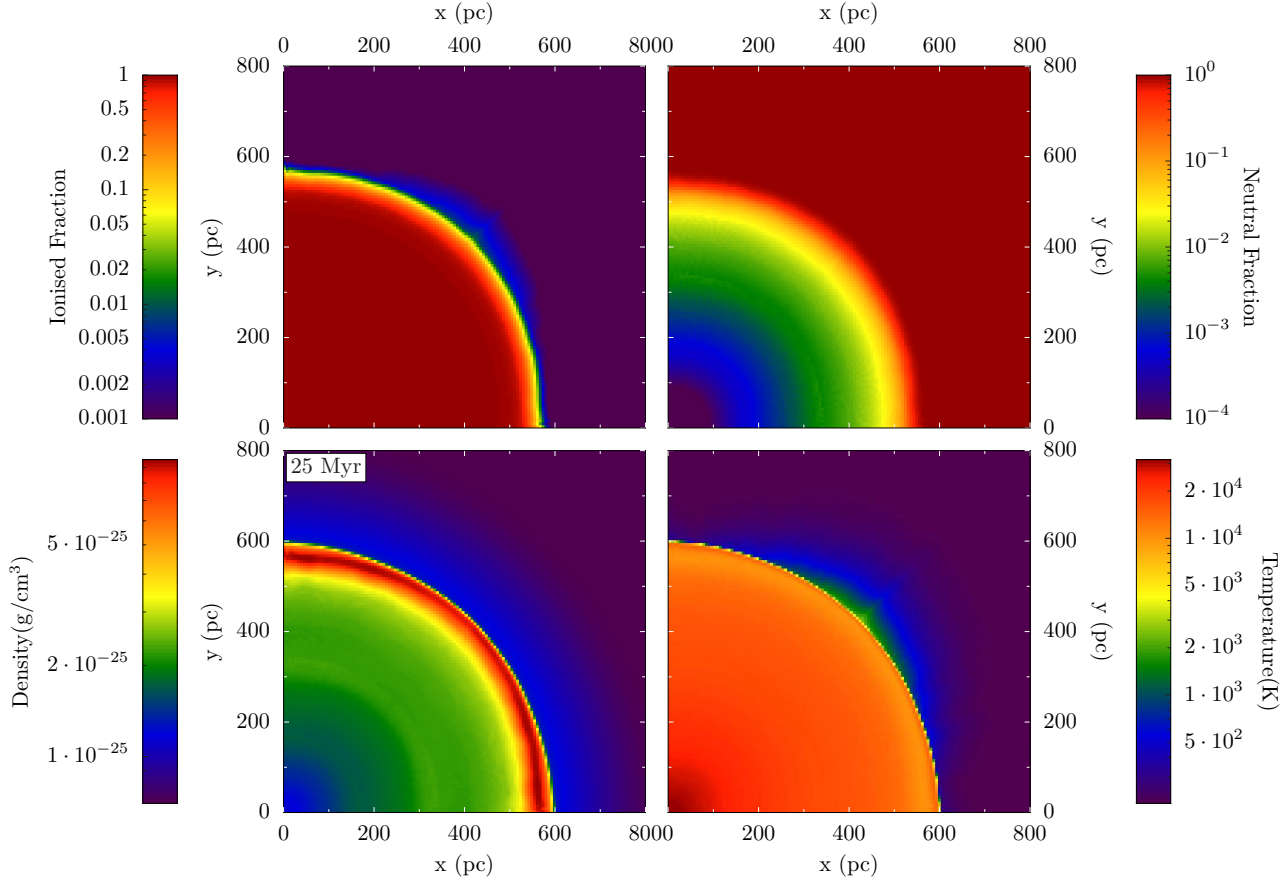


Figure 25. Test 6. (H II region in a $1/r^2$ density profile). Clockwise from the upper left: Slices through the origin of ionised fraction, neutral fraction, temperature, and density at time $t = 25$ Myr.

For the first Myr, the radiation source creates a weak R-type front where the medium is heated and ionised but does not expand because $v_{\text{IF}} > c_s$. When v_{IF} becomes subsonic, the medium can react to the passing ionisation front and creates a shock, leaving behind a heated rarefied medium. This behavior is clearly seen in the radial profiles of density, temperature, ionised fraction, and pressure in Fig. 24. The inner density decreases over two order of magnitude after 25 Myr. To illustrate any deviations in spherical symmetry, we show in Fig. 25 slices of density, temperature, neutral fraction, and ionised fraction at the final time. The only artifact apparent to us is the slight broadening of the shock near the $x = 0$ and $y = 0$ planes. This causes the ionisation front radius to be slightly smaller in those directions. In the diagonal direction, the neutral column density through the shock is slightly smaller, allowing the high-energy photons to photo-ionise and photo-heat the gas to $x_e = 5 \times 10^{-3}$ and $T = 2000$ K out to ~ 50 pc from the shock. The reflecting boundaries are responsible for this artifact because this is not seen when the problem is centred in the domain, removing any boundary effects.

5.3 Test 7. Photo-evaporation of a dense clump

The photo-evaporation of a dense clump in a uniform medium proceeds very differently when radiation hydrodynamics is considered instead of a static density field. The

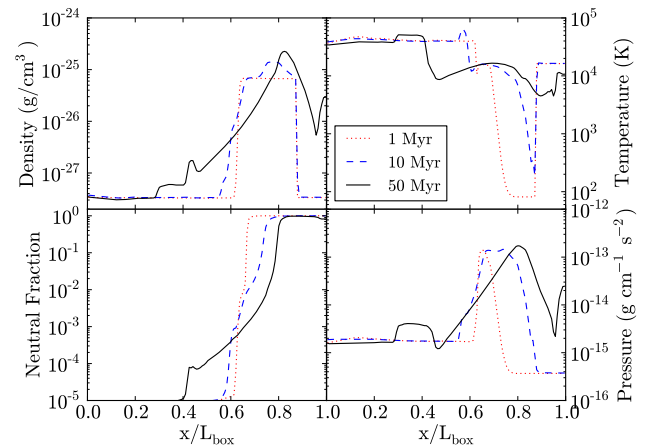


Figure 26. Test 7. (Photo-evaporation of a dense clump). Line cuts from the point source through the middle of the dense clump at $t = 1, 10, 50$ Myr of (clockwise from the upper left) density, temperature, pressure, and neutral fraction.

ionisation front first proceeds as a very fast R-type front, then it slows to a D-type front when it encounters the dense clump. As the clump is gradually photo-ionised and heated, it expands into the ambient medium. The test presented here is exactly like Test 3 but with gas dynamics. In this

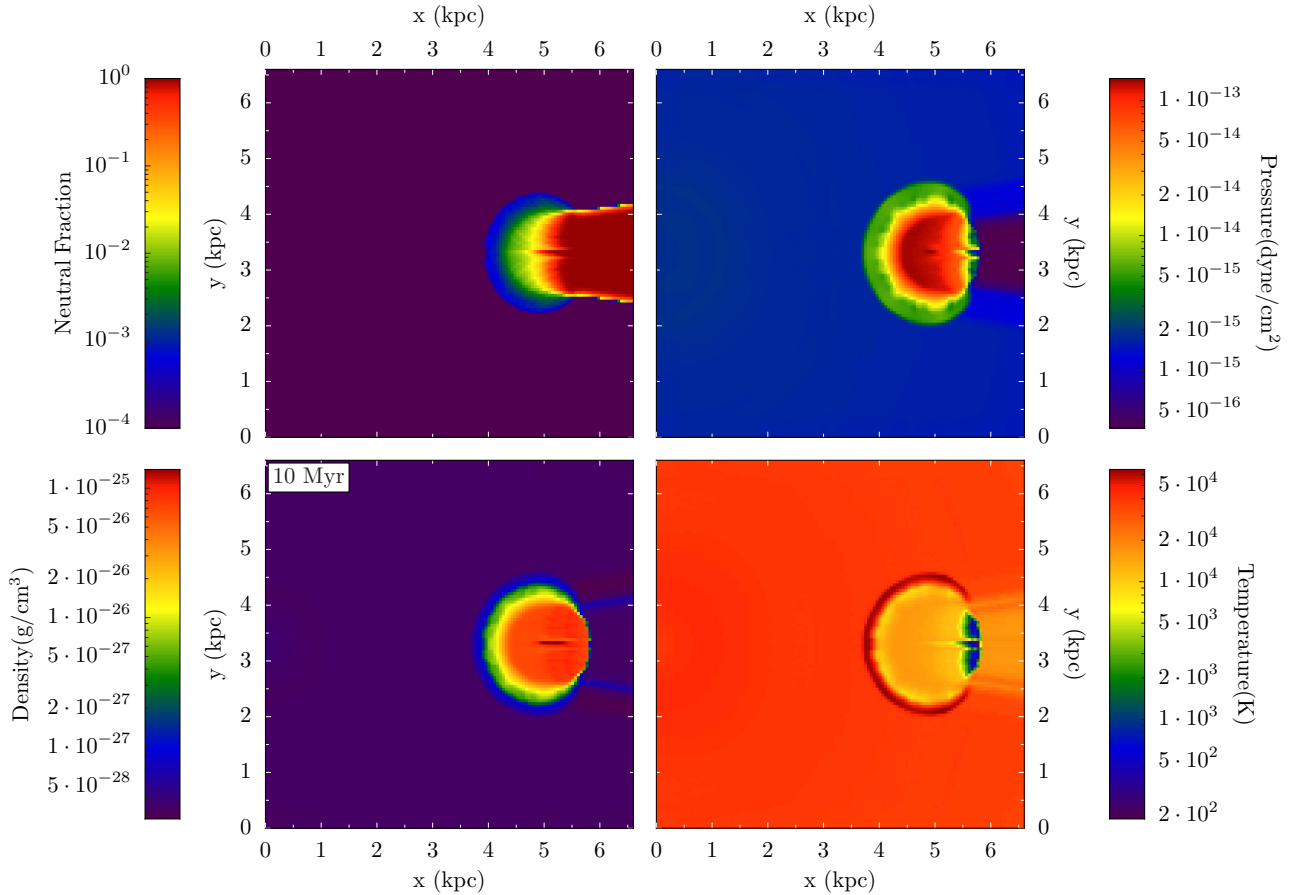


Figure 27. Test 7. (Photo-evaporation of a dense clump). Clockwise from the upper left: Slices through the clump centre of neutral fraction, pressure, temperature, and density at time $t = 10$ Myr.

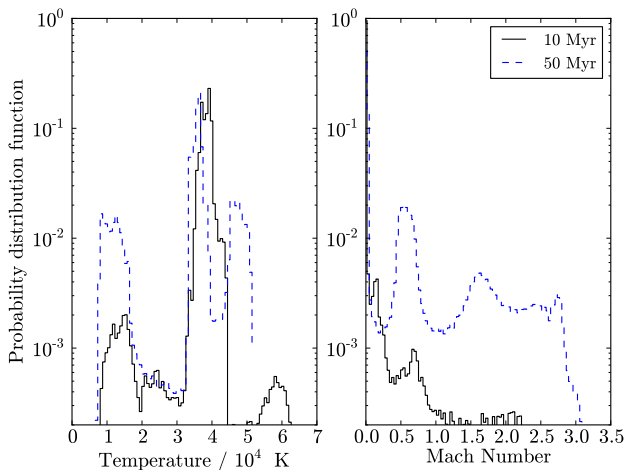


Figure 29. Test 7. (Photo-evaporation of a dense clump). Probability distribution function for temperature (left) and flow Mach number (right) at 10 Myr (solid) and 50 Myr (dashed).

setup, the ionisation front overtakes the entire clump, which is then completely photo-evaporated.

Fig. 26 shows cuts of density, temperature, neutral fraction, and pressure in a line connecting the source and the clump centre at $t = 1, 10$, and 50 Myr. At 1 Myr, the

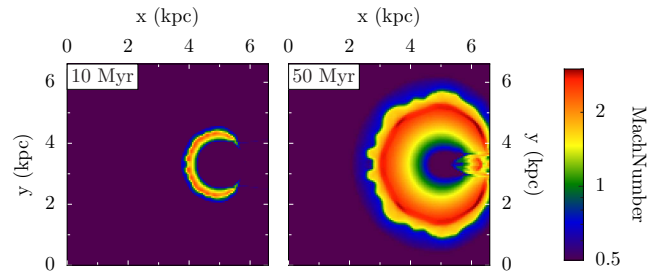


Figure 30. Test 7. (Photo-evaporation of a dense clump). Slices through the clump centre of the flow Mach number at $t = 10$ Myr (left) and 50 Myr (right).

ionisation front has propagated through the left-most 500 pc of the clump. This heated gas is now over-pressurised, as seen in the pressure plot in Fig. 26, and then expands into the ambient medium. This expansion creates a photo-evaporative flow, seen in many star forming regions (e.g. M16; Hester et al. 1996) as stars irradiate nearby cold, dense overdensities. These flows become evident in the density at 10 Myr, seen both in the line cuts and slices (Fig. 27). They have temperatures up to 50,000 K. At this time, the front has progressed about halfway through the clump, if one inspects the neutral fraction. However the high energy photons have heated all but the rear surface of the clump. At the end of the

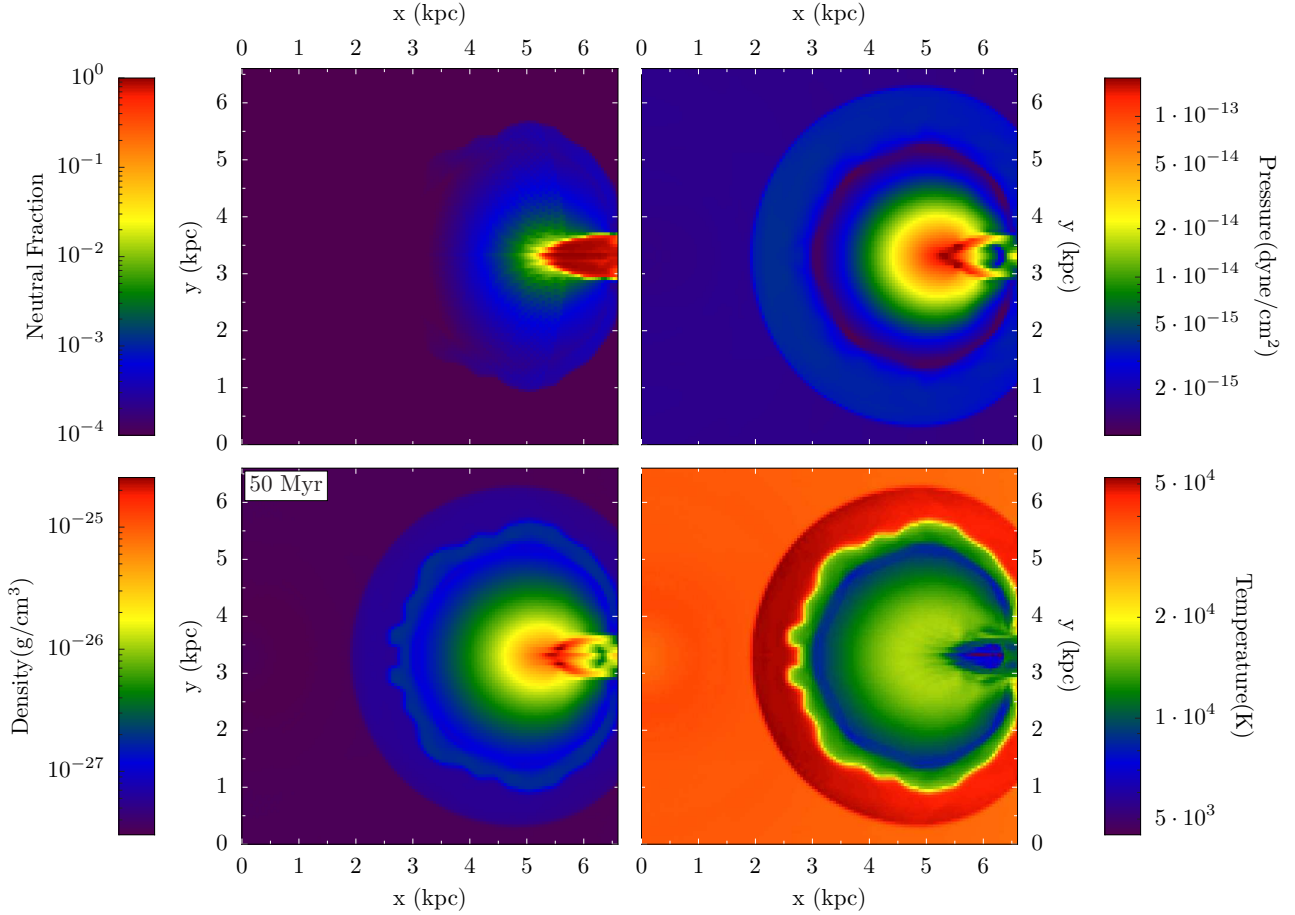


Figure 28. Test 7. (Photo-evaporation of a dense clump). Same as Fig. 26 but at $t = 50$ Myr.

test ($t = 50$ Myr), only the core and its associated shadow is neutral, seen in Fig. 28. The core has been compressed by the surrounding warm medium, thus causing the higher densities seen at $t = 50$ Myr. The non-spherical artifacts on the inner boundary of the warm outermost shell are caused by the initial discretisation of the sphere, as discussed in §4.3. Next Fig. 29 shows the distributions of temperature and flow Mach number in the entire domain at 10 Myr and 50 Myr, showing similar behavior as the codes in RT09. Lastly in Fig. 30, we show slices of the flow Mach number at 10 Myr and 50 Myr, showing the supersonic photo-evaporative flows that originate from the clump.

6 RADIATION HYDRODYNAMICS APPLICATIONS

We have completed presenting results from the RT06 and RT09 test suites. We expand on these test suites to include more complex situations, such as a Rayleigh-Taylor problem illuminated by a radiation source, champagne flows, an irradiated blast wave, collimated radiation, and an H II with a variable source that further demonstrate its capabilities and accuracy. Last we use the new MHD implementation in ENZO v2.0 in the problem of a growing H II region in a magnetic field.

6.1 Application 1. Champagne flow from a dense clump

Radiation-driven outflows from overdensities, known as champagne flows, is a long studied problem (e.g. Yorke 1986, §3.3). To study this, we use the same setup as Bisbas et al. (2009) – a spherical tophat with an overdensity of 10 and radius of 1 pc in a simulation box of 8 pc. The ambient medium has $\rho = 290 \text{ cm}^{-3}$ and $T = 100 \text{ K}$. The radiation source is offset from the overdensity centre by 0.4 pc. It has a luminosity of $10^{49} \text{ ph s}^{-1}$ and a $T = 10^5 \text{ K}$ blackbody spectrum. The resulting Strömgren radius is 0.33 pc, just inside of the overdense clump. These parameters are the same used in Bisbas et al. (2009). The entire domain initially has an ionised fraction of 10^{-6} . We do not consider self-gravity. The simulation has a resolution of 128^3 on base grid, and we refine the grid up to 4 times if a cell has an overdensity of 1.5×2^l , where l is the AMR level. The simulation is run for 150 kyr.

We show slices in the x-y and x-z planes of density in Fig. 31 at $t = 10, 40, 100, 150$ kyr. In the direction of the clump centre, the ionisation front shape transitions from spherical to parabolic after it escapes from the clump in the opposite direction. At $t = 10$ kyr, the surface of the H II region is just contained within the overdensity. In the x-z plane, there are density perturbations only above a latitude of 45 degrees. We believe that these are caused by the mis-

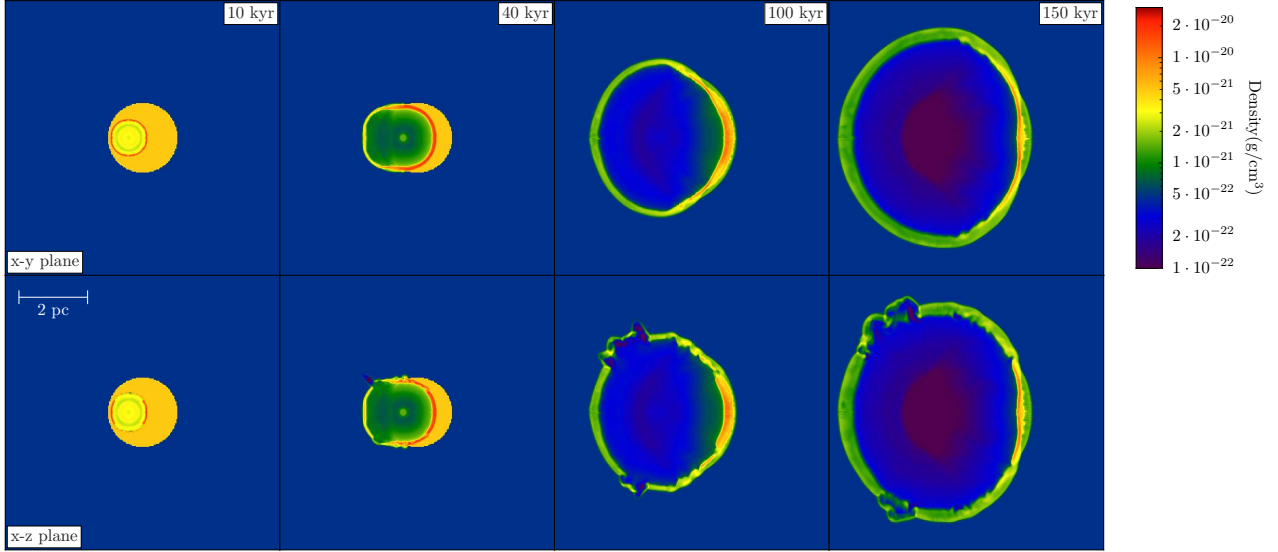


Figure 31. Application 1. (Champagne flow from a dense clump). Slices of density through the initial clump centre in the x-y plane (top) and x-z plane (bottom) at $t = 10, 40, 100, 150$ kyr. Notice the instabilities that grow from perturbations created while the H II region is contained in the dense clump.

match between HEALPix pixels and the Cartesian grid, even with our geometric correction. After the ionisation front escapes from the clump in the negative x-direction, these perturbations grow from Rayleigh-Taylor instabilities as the gas is accelerated when it exits the clump. As the shock propagates through the ambient medium, it is no longer accelerated and has a nearly constant velocity, as seen in Test 6. Thus these perturbations are not as vulnerable to Rayleigh-Taylor instabilities at this point. The ambient medium and shock are always optically thick, even in the directions of the bubbles. Bisbas et al. found that the shock fragmented and formed globules; however we find the density shell is stable against such fragmentation. To investigate this scenario further, our next tests involve radiation driven Rayleigh-Taylor instabilities.

6.2 Application 2. Irradiated Rayleigh-Taylor instability

Here we combine the classic case of a Rayleigh-Taylor instability and an expanding H II region. The Rayleigh-Taylor instability occurs when a dense fluid is being supported by a lighter fluid, initially in hydrostatic equilibrium, in the presence of a constant acceleration field. This classic test alone evaluates how subsonic perturbations evolve. We consider the case of a single-mode perturbation. The system evolves without any radiation until the perturbation grows considerably and then turn on the radiation source. These tests demonstrate that ENZO+MORAY can follow a highly dynamic system and resolve fine density structures.

We run two cases, an optically-thick and optically-thin case. In the former, we take the parameter choices from past literature (e.g. Liska & Wendroff 2003; Stone et al. 2008) by setting the top and bottom halves of the domain to a density $\rho_1 = 2$ and $\rho_0 = 1$, respectively. The velocity perturbation

is set in the z -direction by

$$v_z(x, y, z) = 0.01[1 + \cos(2\pi x/L_x)] \times [1 + \cos(2\pi y/L_y)] \times [1 + \cos(2\pi z/L_z)]/8. \quad (41)$$

We set the acceleration field $g_z = 0.1$ and the adiabatic index $\gamma = 1.4$. We use a domain size of $(L_x, L_y, L_z) = (0.5, 0.5, 1.5)$ with a resolution of $(64, 64, 192)$. For hydrostatic equilibrium, we set $P = P_0 - g\rho(z)z$ with $P_0 = 2.5$. In order to consider a radiation source with a ionising photon luminosity of 10^{42} ph s $^{-1}$, we scale the domain to a physical size of $(0.5, 0.5, 1.5)$ pc; time is in units of Myr; density is in units of m_h , resulting in an initial temperature of $(T_0, T_1) = (363, 726)$ K. The radiation source is placed at the centre of lower z -boundary face and starts to shine at $t = 10$ Myr.

The optically-thin case is set up similarly but with three changes: (1) a density contrast of 10, (2) a luminosity of 10^{43} ph s $^{-1}$, and (3) the source is born at 6.5 Myr. The time units are decreased to 200 kyr so that $(T_0, T_1) = (1.8 \times 10^3, 1.8 \times 10^4)$ K. Note that in code units, pressure is unchanged. We adjust the physical unit scaling because we desire an optically thin bottom medium with $T > 10^4$ K and $x_e \sim 1$. Furthermore, the ionisation front remains R-type before interacting with the instability. A possible physical analogue could be a radiation source heating and rarefying the medium below.

The x and y -boundaries are periodic, and the z -boundaries are reflecting. These will cause artificial features, in particular, because of the top reflecting boundary; nevertheless, these tests provide a stress test on a radiation hydrodynamics solver. We show the evolution of the density, temperature, and ionised fraction of the optically thick and optically thin cases in Figs. 32 and 33. The initial state of the Rayleigh-Taylor instability is shown in the left panels.

In the optically thick case, a D-type front is created,

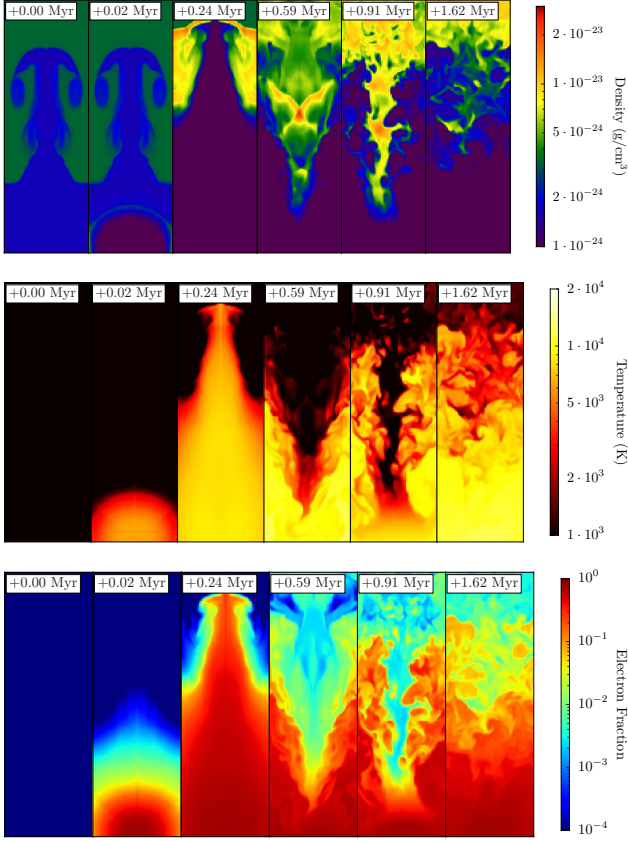


Figure 32. Application 2. (Irradiated Rayleigh-Taylor instability; optically thick case). Slices at $y = 0$ of density (top), temperature (middle), and electron fraction (bottom). The source turns on at $t = 0$.

which is clearly illustrated by the spherical density enhancement at 0.02 Myr. The shock then passes through the instability at ~ 0.25 Myr and reflects off the upper z -boundary. This and complex shock reflections create a Richtmyer-Meshkov instability (see Brouillette 2002, for a review), driving a chaotic jet-like structure downwards. The radiation source photo-evaporates the outer parts of this structure. The interaction between the dense cool “jet” and the hot medium further drives instabilities along the surface, which can be seen when comparing $t = 0.59$ Myr and $t = 0.91$ Myr slices. At the latter time, the jet cannot reach the bottom of the domain before being photo-evaporated. Eventually this structure is completely destroyed, leaving behind a turbulent medium between the hot and cold regions.

The optically thin problem is less violent than the optically thick case because the R-type front does not interact with the initial instability as strongly. The radiation source provides further buoyancy in the already $T = 10^4$ K gas. The gas first to be ionised and photo-evaporated are the outer regions of the instability. The enhanced heating also drives the upper regions of the instability, making the top interface turbulent. It then reflects off the upper z -boundary and creates a warm $T = 5 \times 10^3$ K, partially ionised ($x_e \sim 10^{-2}$), turbulent medium, seen in the slices $t \geq 0.67$ Myr. The slices of electron fraction also show that the dense gas is optically thick.

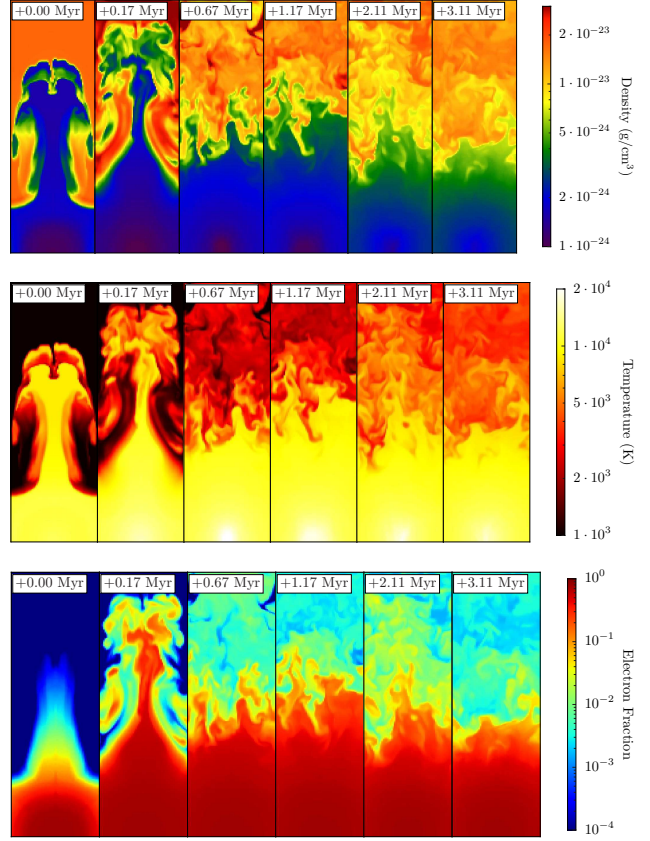


Figure 33. Same as Fig. 32 but for the optically thin case.

6.3 Application 3. Photo-evaporation of a blastwave

A supernova blastwave being irradiated by a nearby star is a likely occurrence in massive-star forming regions. In this test, we set up an idealised test that mimics this scenario. The ambient medium has a density $\rho_0 = 0.1 \text{ cm}^{-3}$ and temperature $T_0 = 10$ K. The domain size is 1 kpc. We use 2 levels of AMR with a base grid of 64^3 that is refined if the density or total energy slope is greater than 0.4. The blastwave is initialised at the beginning of the Sedov-Taylor phase when the mass of the swept-up material equals the ejected material. It has a radius of 21.5 pc, a total energy of 10^{50} erg, and total mass of $100 M_\odot$, corresponding to $E = 315$ eV per particle or $E/k_b = 3.66 \times 10^6$ K. The radiation source is located at the centre of the left x -boundary and has a luminosity of $10^{50} \text{ erg s}^{-1}$. We use a $T = 10^5$ K blackbody spectrum with 2 energy groups (16.0 and 22.8 eV). The source turns on at 2.5 Myr at which point the blastwave has a radius of 200 pc. The simulation is run for 7.5 Myr.

Fig. 34 shows the ionisation front overtaking and disrupting the blastwave. We show the blastwave before the source is born at 2.5 Myr. The interior is rarefied ($\rho \sim 10^{-3} \text{ cm}^{-3}$) and is heated to $T \sim 5 \times 10^5$ K by the reverse shock. At $t = 3$ Myr, the ionisation front is still R-type, and it ionises the rear side of the dense shell. Because the interior is ionised and diffuse, the ionisation front rapidly propagates through it until it reaches the opposite shell surface. Shortly afterward, the ionisation front transitions from

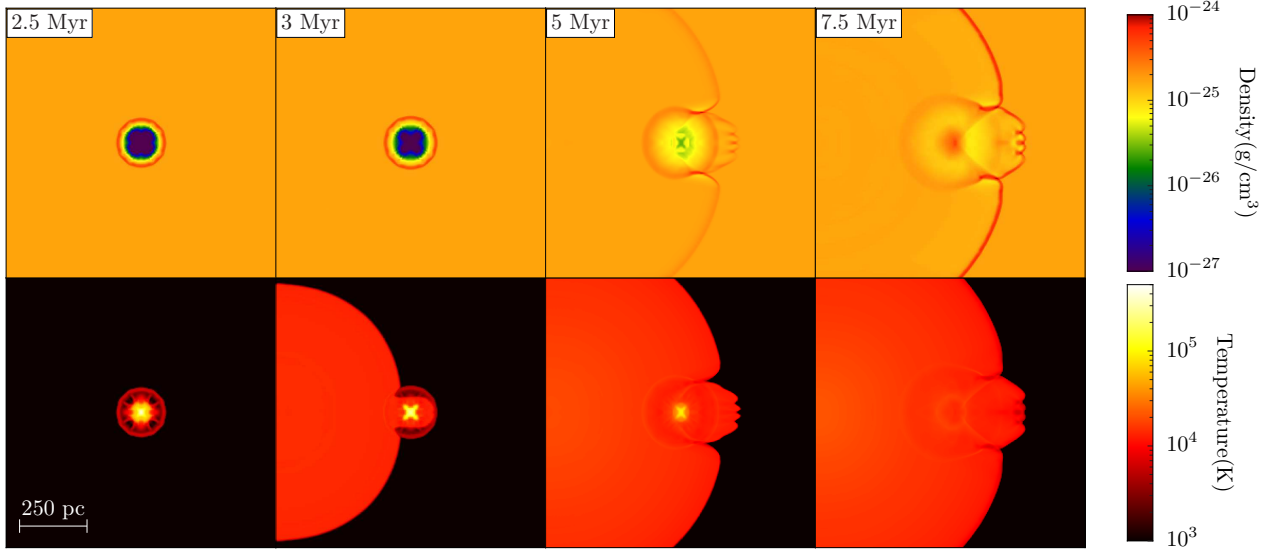


Figure 34. Application 3 (Photo-evaporation of a blastwave). Slices of density (top) and temperature (bottom) at $t = 2.5, 3, 5, 7.5$ Myr in the $x - z$ plane. As the R-type ionisation front propagates through the blastwave centre, instabilities grow from the slightly inhomogeneous hot and rarefied medium. Note that the dense shell of the blastwave also creates dense inward fingers in the ionisation front shock.

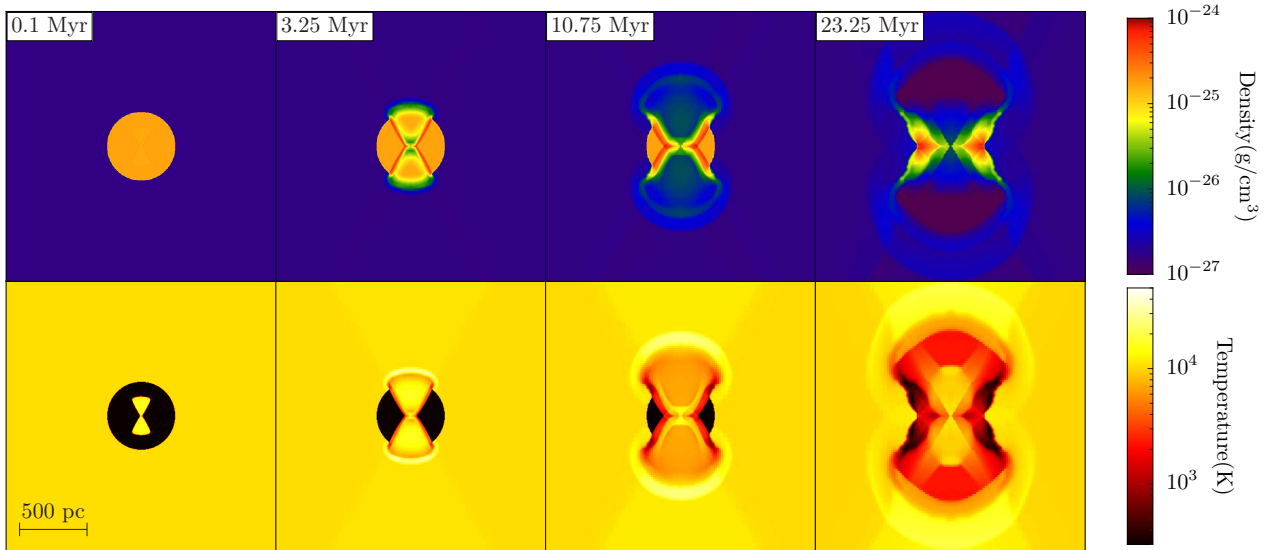


Figure 35. Application 4 (Collimated radiation from a dense clump). Slices of density (top) and temperature (bottom) at $t = 0.1, 3.25, 10.75, 23.25$ Myr. The conical H II region drives shocks transversely into the overdense sphere and creates polar champagne flows. The ambient medium is heated to $T \sim 3 \times 10^4$ K as the ionisation front passes the constant-pressure cloud surface. The ionisation front changes from D-type to R-type after it enters the ambient medium.

R-type to D-type at a radius of 0.5 kpc, seen in the formation of a shock in the 5 Myr density panel. This transition occurs by the construction of the problem not by the interaction with the blastwave. The surfaces of the blastwave that are perpendicular to the ionisation front have the highest column density and thus are last to be fully ionised. The pressure forces from warm ambient medium and blastwave interior compress these surfaces, photo-evaporating them in the process, similar to Test 7. They survive until the final time $t = 7.5$ Myr. As the R-type ionisation front interacts

with the blastwave interior, the density perturbations create ionisation front instabilities (Whalen & Norman 2008) that are seen on the H II region surface at the coordinate $z = 0.5$. Behind the ionisation front, the dense shell of the blastwave is photo-evaporated, and a smooth overdensity is left in the initial blastwave centre.

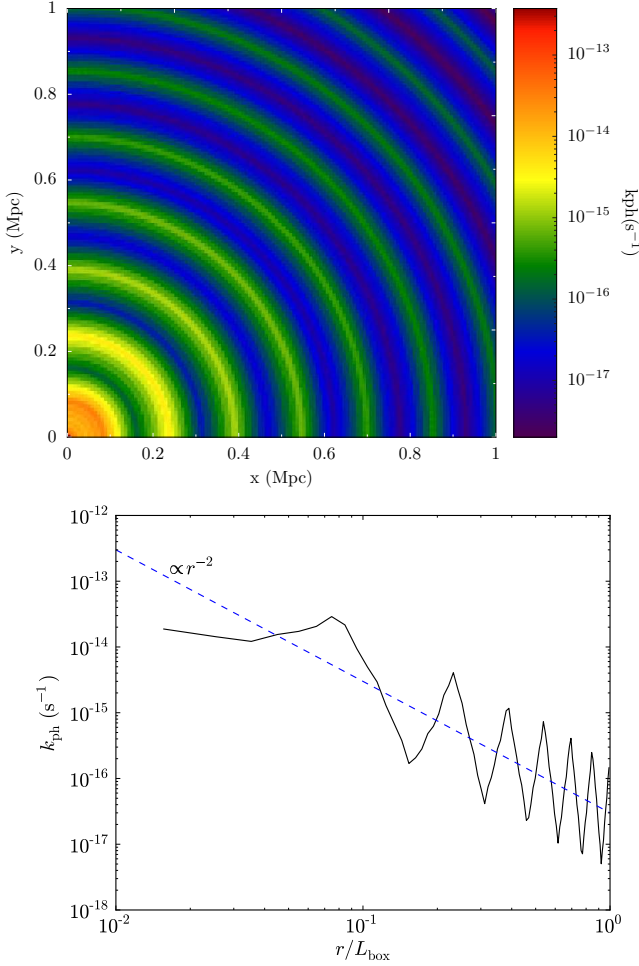


Figure 36. Application 4 (Time variations of the source luminosity). Top: Slice of the photo-ionisation rate k_{ph} through the origin. The source has a duty cycle of 0.5 Myr, and the box has a light crossing time of 3.3 Myr. The shells of high k_{ph} originate from radiation that was emitted when the source was at its peak luminosity, illustrating the time-dependence of the radiative transfer equation. Bottom: Radial profile k_{ph} with the inverse square law overplotted.

6.4 Application 4. Collimated radiation from a dense clump

Some astrophysical systems produce collimated radiation either intrinsically by relativistic beaming or by an optically-thick torus absorbing radiation in the equatorial plane. The latter case would be applicable in a subgrid model of active galactic nuclei (AGN) or protostars, for example. Simulating collimated radiation with ray tracing is trivially accomplished by only initialising rays that are within some opening angle θ_c .

We use a domain that is 2 kpc wide and has an ambient medium with $\rho_0 = 10^{-3} \text{ cm}^{-3}$, $T = 10^4 \text{ K}$, $x_e = 0.99$. We place a dense clump with $\rho/\rho_0 = 100$, $T = 100 \text{ K}$, $x_e = 10^{-3}$, and $r = 250 \text{ pc}$, at the centre of the box. Radiation is emitted in two polar cones with $\theta_c = \pi/6$ with 768 (HEALPix level 3) initial rays, a total luminosity of $10^{49} \text{ erg s}^{-1}$, and a 17.6 eV mono-chromatic spectrum. This results in $t_{\text{rec}} = 1.22 \text{ Myr}$ and $R_s = 315 \text{ pc}$, just outside of

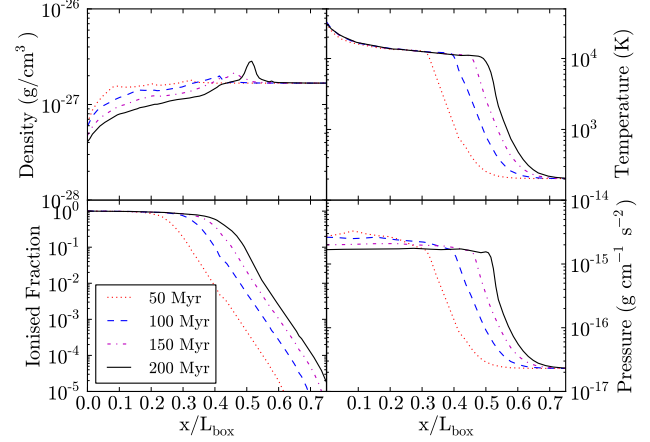


Figure 37. Application 4 (Time variations of the source luminosity). Radial profiles of (clockwise from upper left) density, temperature, pressure, and ionised fraction at $t = 50, 100, 150, 200, 250 \text{ Myr}$. In this problem, the time variations in the source have little effect on the overall H II region expansion. Inside the ionisation front at $t = 50 \text{ Myr}$, there are small density perturbations that are created by the variable source that are later smoothed out over a sound crossing time.

the sphere. The base grid has a resolution of 64^3 , and it is refined with the same overdensity criterion as Application 1. We run this test for 25 Myr.

We illustrate the expansion of the H II region created by the beamed radiation in Fig. 35. Before $t = 3 \text{ Myr}$, the H II region is conical and contained within the dense clump, depicted in the $t = 0.1 \text{ Myr}$ snapshot of the system. At this time, the ionisation front is transitioning from R-type to D-type in the transverse direction of the cone. This can be seen in the minute overdensities on the H II transverse surface. When it breaks out of the overdensity, a champagne flow develops, where the ionisation front transitions back to a weak R-type front. The cloud surface is a constant-pressure contact discontinuity (CD) with a density jump of 100. After the front heats the gas at the CD, there exists a pressure difference of ~ 100 . In response, the high density gas accelerates into the ambient medium and heats it to $3 \times 10^4 \text{ K}$. Additionally a rarefaction wave travels towards the clump centre. At later times, the transverse D-type front continues through the clump, eventually forming a disc-like structure at the final time. The polar champagne flows proceed to flow outwards and produces a dense shell with a diffuse (10^{-28} cm^{-3}) and warm (5000 K) medium in its wake.

6.5 Application 5. Time variations of the source luminosity

Our implementation retains the time derivative of the radiative transfer equation [equation (2)] if we choose a constant ray tracing timestep, which saves the photon packages between timesteps if $c dt_P < L_{\text{box}}$. This effect only becomes apparent when the variation time-scale of the point source is smaller than the light crossing time of the simulation. Furthermore, the timestep should resolve the variation time-scale by at least a few times. This property might be important in large box simulations with variable sources, e.g. AGN

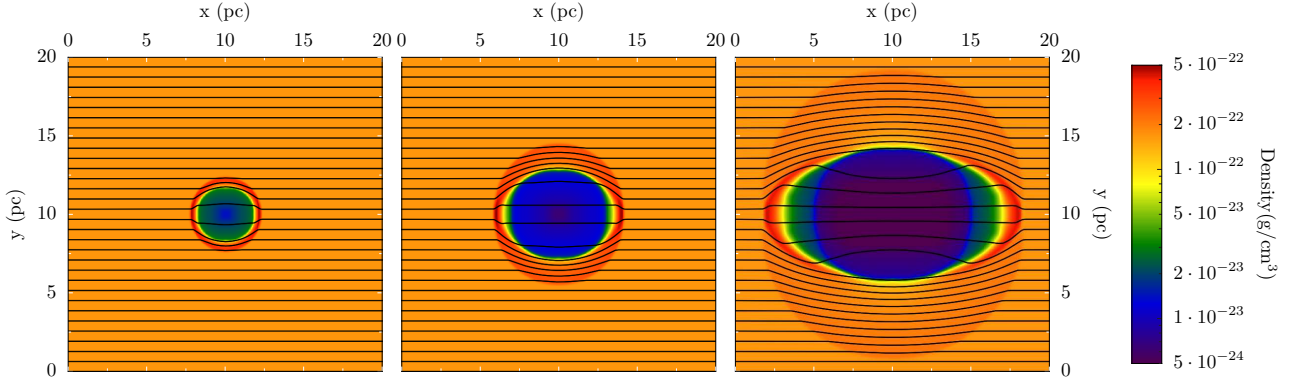


Figure 38. Application 5. (H II region with MHD). Left to right: slices of density at $t = 0.18, 0.53, 1.58$ Myr in the x-y plane. The streamlines show the magnetic field.

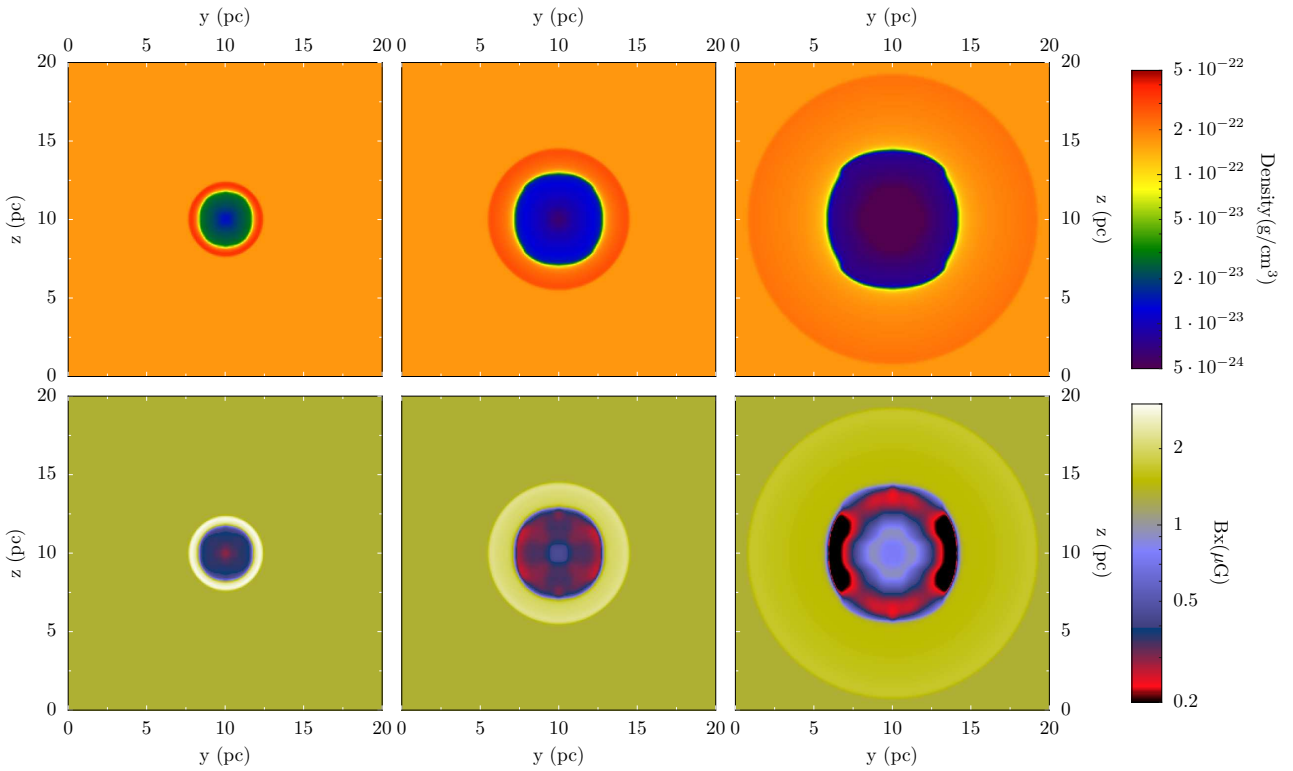


Figure 39. Application 5. (H II region with MHD). Slices of density (top) and the x-component of the magnetic field (bottom) in the y-z plane at $t = 0.18, 0.53, 1.58$ Myr (left to right).

radiative feedback. To test this, we can use an exponentially varying source with some duty cycle t_0 . In a functional form, this can be described as

$$L(t) = L_{\max} \times \exp[A(t_f/t_0 - 1)] \quad (42)$$

where $t_f = 2 \times |t - t_0 \times \text{round}(t/t_0)|$, and $A = 4$ controls the width of the radiation pulse. To illustrate the effects of source variability, we remove any dependence on the medium by considering an optically-thin uniform density $\rho = 10^{-4} \text{ cm}^{-3}$. We take $L_{\text{box}} = 1 \text{ Mpc}$, which has a light crossing time of 3.3 Myr. A source is placed at the origin with $L_{\max} = 10^{55} \text{ ph s}^{-1}$ and $t_0 = 0.5 \text{ Myr}$. We use a radiative transfer timestep of 50 kyr to resolve the duty

cycle by 10 timesteps. The simulation is run for 6 Myr, so the radiation propagates throughout the box.

The variability of the source is clearly illustrated in the photo-ionisation rates, shown in Fig. 36. The shells of relative maximum k_{ph} corresponds to radiation that was emitted when the source was at its peak luminosity. They are separated by $ct_0 \text{ Mpc}$ and are geometrically diluted with increasing radius. Averaged over shells of the same width, photo-ionisation rates decrease as $1/r^2$.

Next we test the hydrodynamical response to a varying source by repeating Test 5. We set the peak luminosity $L_{\max} = 2 \times 10^{49} \text{ erg s}^{-1}$ that is a factor of 4 more luminous than Test 5, so the average luminosity is $\sim 5 \times 10^{48} \text{ erg s}^{-1}$. The spectrum is mono-chromatic with an energy of 29.6 eV.

We set the variation time-scale $t_f = cL_{\text{box}}/3 = 16.3$ kyr and use a constant radiative transfer timestep $t_P = t_f/4 = 4.07$ kyr. The simulation is run for 200 Myr. We show the radial profiles of density, temperature, ionised fraction, and pressure in Fig. 37. The variable source has little effect on the overall growth of the H II region. It has the approximately the same radius as Test 5 at $t = 200$ Myr when run with a mono-chromatic spectrum (see §7.3). At early times, the variable source creates density perturbations with an average size of 500 pc inside the ionised region, seen in the $t = 50$ Myr profiles. They do not create any instabilities and are smoothed out over its sound crossing time of ~ 50 Myr.

6.6 Application 6. H II region with MHD

Another prevalent physical component in astrophysics is a magnetic field. We utilise the new magnetohydrodynamics (MHD) framework (Wang & Abel 2009) in ENZO v2.0 that uses an unsplit conservative hydrodynamics solver and the hyperbolic $\nabla \cdot \mathbf{B} = 0$ cleaning method of Dedner et al. (2002). We show a test problem with an expanding H II region in an initially uniform density field and constant magnetic field. We use the same problem setup as Krumholz et al. (2007) – $\rho = 100 \text{ cm}^{-3}$, $T = 11 \text{ K}$, $L_{\text{box}} = 20 \text{ pc}$ with a resolution of 256^3 . This ambient medium is threaded by a magnetic field $\mathbf{B} = 14.2\hat{x} \mu\text{G}$. The Alfvén speed is 2.6 km s^{-1} . The radiation source is located in the centre of the box with a luminosity $L = 4 \times 10^{46} \text{ ph s}^{-1}$ with a 17.6 eV mono-chromatic spectrum, resulting in a Strömgren radius $R_s = 0.5 \text{ pc}$. The simulation is run for 1.58 Myr. The hydrodynamics solver uses an HLL Riemann solver (Harten et al. 1983) and piecewise linear method (PLM) reconstruction (van Leer 1977) for the left and right states in this problem.

As the H II region grows in the magnetised medium, shown in Figs. 38 and 39, it transforms from spherical to oblate as it is magnetically confined in directions perpendicular to the magnetic field. This occurs at $t > 0.5 \text{ Myr}$ because the magnetic pressure exceeds the thermal pressure, and the gas can only flow along field lines. Krumholz et al. observed some carbuncle artifacts along the ionisation front; whereas we see smooth density gradients, which is most likely caused by both the geometric correction to the ray tracing (§2.3) and the diffusivity of the HLL Riemann solver when compared to Roe’s Riemann solver used in Krumholz et al. (2007), who also use PLM as a reconstruction method. The evolution of the magnetic field lines evolve in a similar manner as their results.

7 RESOLUTION TESTS

Resolution tests are important in validating the accuracy of the code in most circumstances, especially in production simulations where the initial environments surrounding radiation sources are unpredictable. In this section, we show how our adaptive ray-tracing implementation behaves when varying spatial, angular, frequency, and temporal resolutions.

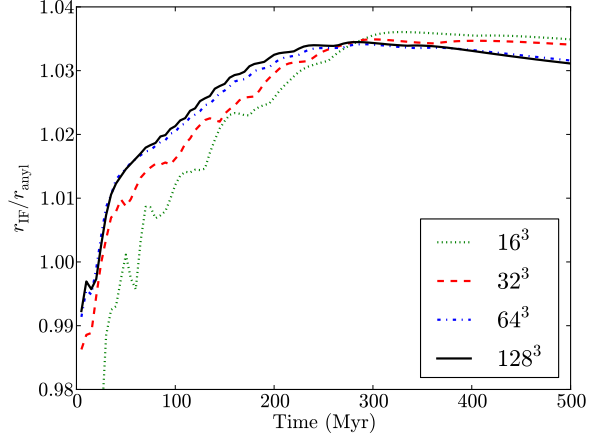


Figure 40. Growth of the ionisation front radius, compared to the analytical radius, in Test 1 with varying spatial resolutions. At resolutions of 16^3 and 32^3 , the ionisation front is underestimated for the first ~ 25 Myr but converges within 0.5% of the higher resolution runs.

7.1 Spatial resolution

Here we use Test 1 (§4.1) as a testbed to investigate how the evolution of the Strömgren radius changes with resolution. We keep all aspects of the test the same, but use resolutions of 16^3 , 32^3 , 64^3 , and 128^3 . In Fig. 40, we show the ratio $r_{\text{IF}}/r_{\text{anly}}$, similar to Fig. 5, using these different resolutions. The radii in the 64^3 and 128^3 runs evolve almost identically. Compared to these resolutions, the lower 16^3 and 32^3 resolution runs only lag behind by 1% until 300 Myr, and afterwards it is larger by 0.5% than the higher resolution cases. This shows that our method gives accurate results, even in marginally resolved cases, which is expected with a photon conserving method. Furthermore this demonstrates that the geometric correction does not significantly affect photon conservation.

7.2 Angular resolution

The Cartesian grid must be sampled with sufficient rays in order to calculate a smooth radiation field. To determine the dependence on angular resolution, we consider the propagation of radiation through an optically thin, uniform medium. The radiation field should follow a $1/r^2$ profile. As the grid is less sampled by rays, the deviation from $1/r^2$ should increase. This test is similar to Test 1, but the medium has $\rho = 10^{-3} \text{ cm}^{-3}$, $T = 10^4 \text{ K}$, and $1 - x_e = 10^{-4}$. The simulation is only run for one timestep because the radiation field should be static in this optically-thin test.

We consider minimum ray-to-cell ratios $\Phi_c = (1.1, 2.1, 3.1, 5.1, 10.1, 25.1)$. Slices of the photo-ionisation rates through the origin are shown in Fig. 41 for these values of Φ_c . In this figure, we limit the colormap range to a factor of 3 to show the nature of the artifacts in more contrast. Unscaled, the rates in the figures would span 4 orders of magnitude. When $\Phi_c \leq 3.1$, the cell-to-cell variations are apparent because there are not enough rays to sufficiently sample the radiation field, even with the geometric correction factor f_c , whose improvements are shown later in §8.1.

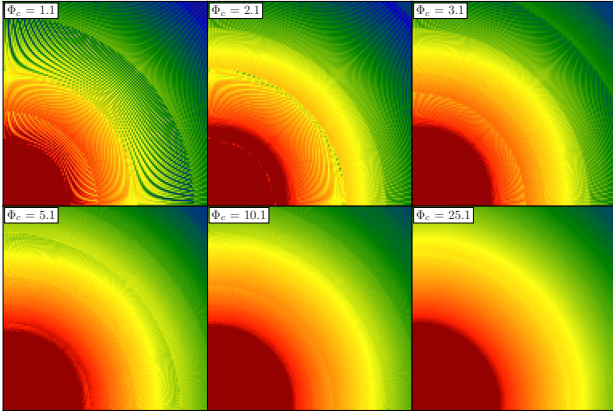


Figure 41. Variations in the photo-ionisation rates for different ray-to-cell samplings Φ_c . The colormap only spans a factor of 3 to enhance the contrast. In comparison, the photo-ionisation rate actually spans 4 orders of magnitude in this test.

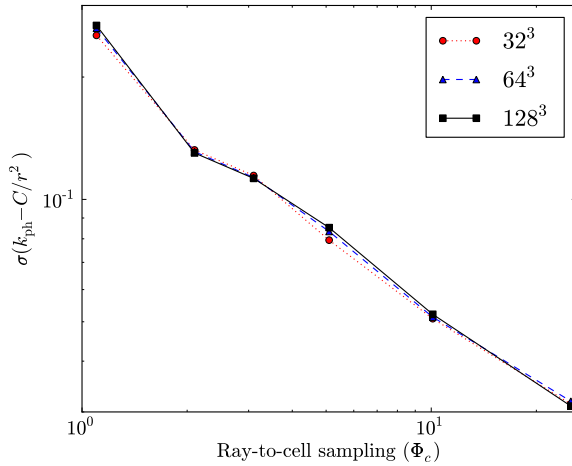


Figure 42. Standard deviations of the difference between the computed photo-ionisation rates and an inverse square law as a function of ray-to-cell samplings Φ_c for different spatial resolutions. There is no dependence on the spatial resolution, and the accuracy increases as $\sigma \propto \Phi_c^{-0.6}$.

At $\Phi_c = 5.1$, these artifacts disappear, leaving behind a shell artifact where the radiation fields do not smoothly decrease as $1/r^2$. At higher values of Φ_c , this shell artifact vanishes as well.

One measure of accuracy is the deviation from an $1/r^2$ field because this problem is optically-thin. To depict the increase in accuracy with ray sampling, we take the difference between the calculated photo-ionisation rate and a $1/r^2$ field, and then plot the standard deviation of this difference field versus angular resolution in Fig. 42. We plot this relation for resolutions of 32^3 , 64^3 , and 128^3 and find no dependence on spatial resolution, which is expected because we control the angular resolution in terms of cell widths, not in absolute solid angles. We find that the deviation from an inverse square law decreases as $\sigma \propto \Phi_c^{-0.6}$.

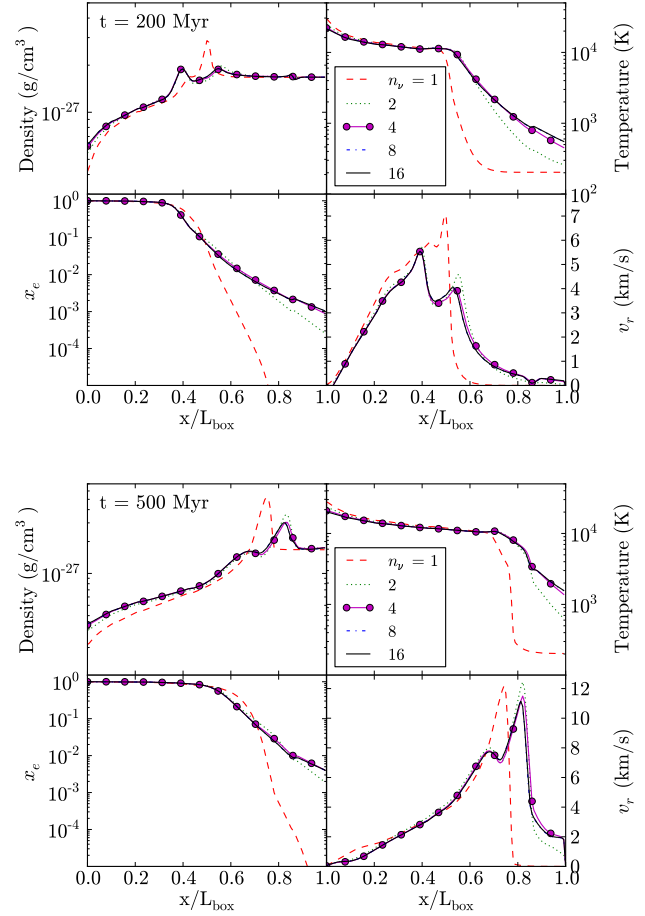


Figure 43. Radial profiles of (clockwise from the upper left) density, temperature, radial velocity, and ionised fraction for Test 5 with $n_\nu = 1, 2, 4, 8$, and 16 frequency bins sampling the $T = 10^5$ K blackbody spectrum. The data are shown at $t = 200$ Myr (top) and $t = 500$ Myr (bottom). The double-peaked structure in the shock only appears with a multi-frequency spectrum. The solution converges at $n_\nu \geq 4$.

7.3 Frequency resolution

The ionisation front radius is within 5–10% of analytical solutions in Tests 1, 2, and 5 with only one energy group; however a multi-frequency spectrum can create differences in the reactive flows. We use Test 5 (§5.1; an expanding H II region with hydrodynamics) to probe any differences in the solution when varying the resolution of the spectrum. In RT09, ZEUS-MP was used to demonstrate the effect of a multi-frequency spectrum on the dynamics of the ionisation front in this test. Instead of a single shock seen in the mono-chromatic spectrum, the shock obtains a double-peaked structure in density and radial velocity. We rerun Test 5 with a $T = 10^5$ K blackbody spectrum sampled by $n_\nu = 1, 2, 4, 8$, and 16 frequency bins. We use the following energies:

- $n_\nu = 1$: Mean energy of 29.6 eV
- $n_\nu = 2$: Mean energies in bins 13.6–30 and >30 eV–21.1, 43.0 eV

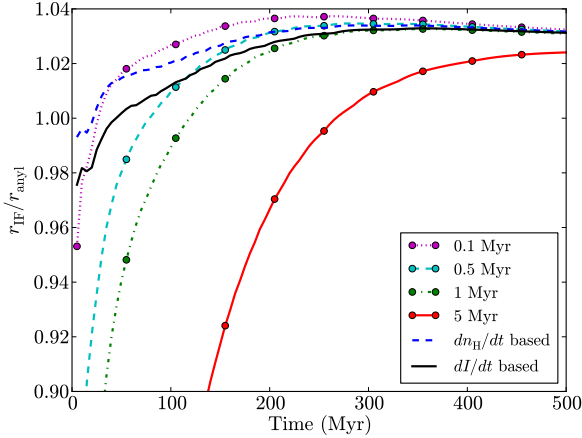


Figure 44. Growth of the ionisation front radius, compared to the analytical radius, in Test 1 with varying radiative transfer timesteps. The dn_{H}/dt and dI/dt based timesteps provide the best accuracy, combined with computational efficiency because they take short timesteps when the H II is expanding rapidly but take long timesteps when the photon gradients are small when r_{IF} is large. At the final time, all but the $t = 5$ Myr constant timestep produce identical ionisation front radii.

- $n_{\nu} = 4$: Mean energies in bins 13.6–20, 20–30, 30–40, and >40 eV–16.7, 24.6, 34.5, 52.1 eV
- $n_{\nu} = 8, 16$: Logarithmically spaced between 13.6 and 50 eV for the first $n_{\nu} - 1$ bins, and the last bin is the mean energy above 50 eV.

Fig. 43 shows the radial profiles of density, temperature, ionised fraction, and radial velocity at $t = 200$ Myr and $t = 500$ Myr. All of the runs with $n_{\nu} > 1$ show the double peaked features in density and radial velocities. The monochromatic spectrum misses this feature completely because all of the radiation is absorbed at a characteristic column density. In the multi-frequency spectra, the higher energy photons are absorbed at larger column densities and photo-heated this gas. This heated gas creates a photo-evaporative flow that collides with the innermost shock, forming the double peaked density profile. The $n_{\nu} \geq 4$ runs are indistinguishable, and the $n_{\nu} = 2$ spectrum only leads to a marginally higher density in the outer shock and lower ionised fractions and temperatures in the ambient medium. In effect, a mono-chromatic spectrum can be sufficient if the problem focuses on large-scale quantities, e.g. ionised filling fractions in reionisation calculations. Conversely these effects may be important when studying the details of small-scale processes, e.g. photo-evaporation.

7.4 Temporal resolution

The previous three dependencies did not affect the propagation of the ionisation front greatly. However in our and others' past experience (e.g. Shapiro et al. 2004; Mellema et al. 2006; Petkova & Springel 2009), the timestep, especially too small a one, can drastically underestimate the ionisation front velocity. Here we use Test 1 but with 64^3 resolution to compare different time-stepping methods – restricted changes in H II (dn_{H}/dt based; §3.4.1), constant timesteps of

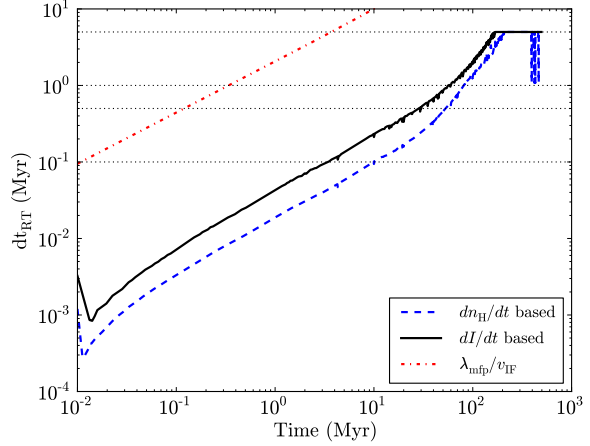


Figure 45. Variable time-stepping for the methods that limit change in neutral fraction (solid) and specific intensity (dotted). The horizontal lines show the constant timesteps that were used in the tests. The crossing time of a mean free path by the ionisation front is plotted for reference.

0.1, 0.5, 1, and 5 Myr (§3.4.3), and based on incident radiation (dI/dt based; §3.4.4). The growth of the ionisation front radius is shown in Fig. 44. Both the H II restricted and incident radiation variable time-stepping methods agree within a few percent throughout the entire simulation, as does the run with constant $dt_P = 0.1$ Myr timesteps. With the larger constant timesteps, the numerical solution lags behind the analytical one, but they converge to an accurate H II radii at late times. Even $dt_P = 5$ Myr timestep, which underestimated it by 35% at 50 Myr, is within a percent of the analytical solution.

The larger constant timesteps deviate from these more accurate solutions at early times because the photon energy gradient is large, and thus so is the ionisation front velocity. To understand this, the ionisation front can be considered static in a given timestep. Here the ionising radiation can only penetrate into the neutral gas by roughly a photon mean path λ_{mfp} . Only in the next timestep, the ionisation front can advance. If the timestep is larger than $\lambda_{\text{mfp}}/v_{\text{IF, any1}}$, then the numerical solution may fall behind.

The variable time-stepping of the dn_{H}/dt and dI/dt methods adjust accordingly to the physical situation, as seen in the plot of timestep versus time (Fig. 45). They provide high accuracy when the source first starts to shine. At later times, the ionisation front slows as it approaches the Strömgren radius, and large timesteps are no longer necessary. The dI/dt method has a similar timestep as the dn_{H}/dt method. It is larger by a factor of ~ 2 because of our choice of the safety factor $C_{\text{RT, cff}} = 0.5$. This causes its calculated radius to be smaller by 1% at $t < t_{\text{rec}}$, which is still in good agreement with the analytical value.

8 METHODOLOGY TESTS

Here we show tests that evaluate new features in ENZO+MORAY, such as the improvements from the geometric correction factor, optically-thin approximations, treatment

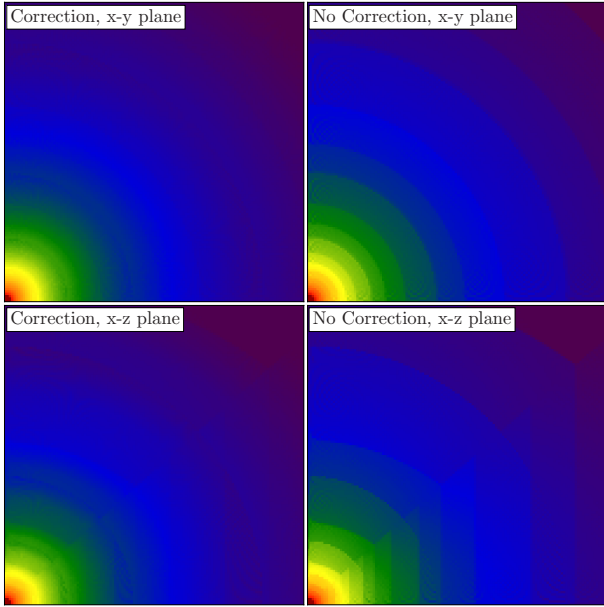


Figure 46. Slices of the photo-ionisation rate in the x-y plane (top row) and x-z plane (bottom row) with (left column) and without (right column) the geometric correction. The slices are through the origin. In the x-y plane, it reduces the shell artifacts. In the x-z plane, it reduces the severity of a non-spherical artifact delineated at a 45 degree angle, where the HEALPix scheme switches from polar to equatorial type pixels.

of X-ray radiation, and radiation pressure. Lastly we test for any non-spherical artifacts in the case of two sources.

8.1 Improvements from the covering factor correction

As discussed in §2.3, non-spherical artifacts are created by a mismatch between the HEALPix pixelisation and the Cartesian grid. This is especially apparent in optically-thin regions, where the area of the pixel is greater than the $(1 - e^{-\tau})$ absorption factor. In this section, we repeat the angular resolution tests in §7.2 with $\Phi_c = 5.1$. Slices of the photo-ionisation rates through the origin are shown in Fig. 46, depicting the improvements in spherical symmetry and a closer agreement to a smooth $1/r^2$ profile. Previous attempts to reduce these artifacts either introduced a random rotation of the HEALPix pixelisation (e.g. Abel & Wandelt 2002; Trac & Cen 2007; Krumholz et al. 2007) or by increasing the ray-to-cell sampling.

In the x-y plane without the correction, there exists shell artifacts where the photo-ionisation rates abruptly drops when the rays are split. This occurs because the photon flux in the rays are constant, so k_{ph} is purely dependent on the ray segment length through each cell. Geometric dilution mainly occurs when the number of rays passing through a cell decreases. With the correction, geometric dilution also occurs when the ray's solid angle only partially covers the cell. This by itself alleviates these shell artifacts. In the x-z plane without the correction, there is a non-spherical artifact delineated at a 45 degree angle. In the lower region, the rays are associated with equatorial HEALPix pixels, and in the

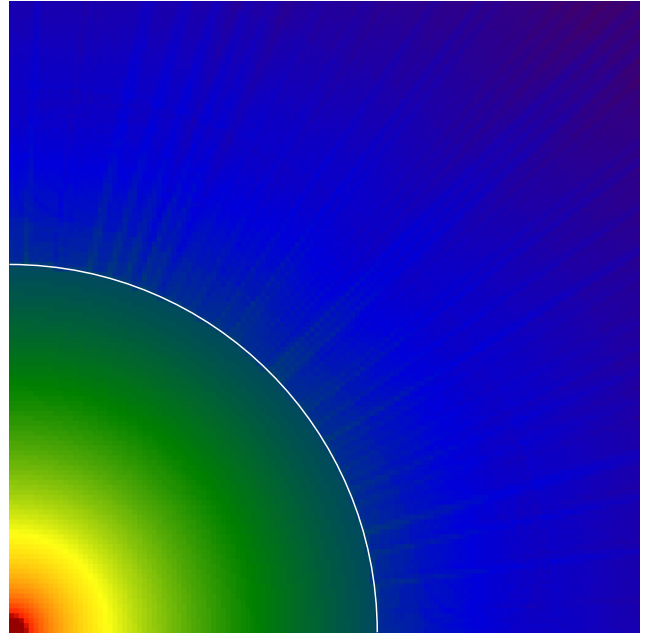


Figure 47. Optically-thin approximation to the radiation field with one ray per cell in optically thin regions. The angular artifacts result from the transition to optically thick (white line) at an optical depth $\tau = 0.1$.

upper region, they are polar HEALPix pixels. This artifact is not seen in the x-y plane because all rays are of a equatorial type. The geometric correction smooths this artifact but does not completely remove it.

8.2 Optically-thin approximation

In practice, we have found it difficult to transition from the optically-thin approximation to the optically-thick regime without producing artifacts in the photo-ionisation rate k_{ph} . We use the optically thin problem used in the angular resolution test (§7.2) with $\Phi_c = 5.1$ to show these artifacts in k_{ph} in Fig. 47. The radiation field strictly follows a $1/r^2$ profile until it reaches $\tau_{\text{thin}} \equiv 0.1$, which is denoted by the white quarter circle in the figure. Within this radius, only $\Phi_c = 1$ is required. Then at this radius, the rays are then split until a sampling of Φ_c is satisfied. Angular spike artifacts beyond this radius arise because of the interface between the optically-thin approximation and full ray tracing treatment. They originate in cells that intersect the τ_{thin} surface, which are split into the optically thin and thick definitions. Unfortunately we have not determined a good technique to avoid such artifacts. They occur because of the following reason. When the first ray with $\tau < 0.1$ exits such a cell, it applies the optically-thin approximation and marks the cell so no other ray from the same source contributes to its k_{ph} and Γ field. However other rays may exit the cell with $\tau > 0.1$ because the maximum distance between the far cell faces and the source is not always $\tau < 0.1$. Then these rays will split in this cell and add to k_{ph} and become attenuated, reducing its photon fluxes. When the rays continue to the next cell after this transition, the photon fluxes are not necessarily equal to each other, creating the angular artifacts seen in Fig. 47. We are continuing to formulate a scheme that avoids these arti-

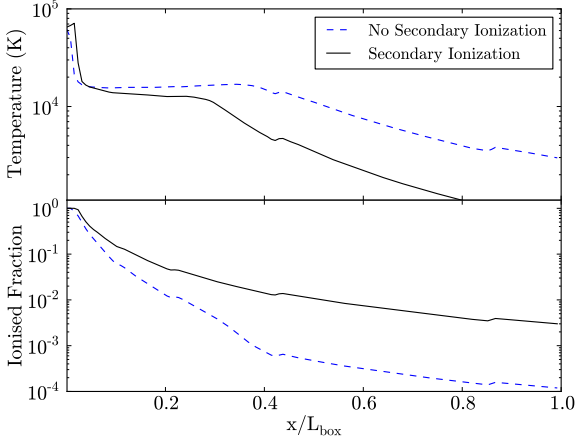


Figure 48. Radial profiles of temperature and ionised fraction showing the effects of secondary ionisations from a monochromatic 1 keV spectrum. The discontinuity at $r \sim 0.4$ is caused by artifacts in the ray tracing, which is described in Test 1. The high energy photons can ionise multiple hydrogen atoms, increasing the ionised fraction. In part, less radiation goes into thermal energy, lowering the temperature.

facts because this approximation will be very advantageous in simulations with large ionised filling factors.

8.3 X-Ray secondary ionisations and reduced photo-heating

Here we test our implementation of secondary ionisations from high-energy photons above 100 eV, described in §2.5.2 and used in Alvarez et al. (2009) in the context of accreting black holes. We use the same setup as Test 5 but with an increased luminosity $L = 10^{50}$ erg s $^{-1}$ and a mono-chromatic spectrum of 1 keV. Fig. 48 compares the density, temperature, ionised fraction, and neutral fraction of the expanding H II region considering secondary ionisations and reduced photo-heating and considering only one ionisation per photon and the remaining energy being thermalised.

Fig. 48 shows the main effects of secondary ionisations from the 1 keV spectrum on the ionisation and thermal state of the system. Without secondary ionisations, each absorption results in one ionisation with the remaining energy transferred into thermal energy. But with secondary ionisations, recall that most of the radiation energy goes into hydrogen and helium ionisations in neutral gas; whereas in ionised gas, most of the energy is thermalised. In this test, only the inner 300 pc is completely ionised because of the small cross-section of hydrogen at $E_{\text{ph}} = 1$ keV. Beyond this core, the medium is only partially ionised. This process expands the hot $T = 10^5$ K core by a factor of 2. In the outer neutral regions, the ionisation fraction is larger by a factor of ~ 10 , which in turn results in less photo-heating, lowering the temperature by a factor 2–3.

8.4 Radiation pressure

Radiation pressure affects gas dynamics in an H II region when its force is comparable to the acceleration created by

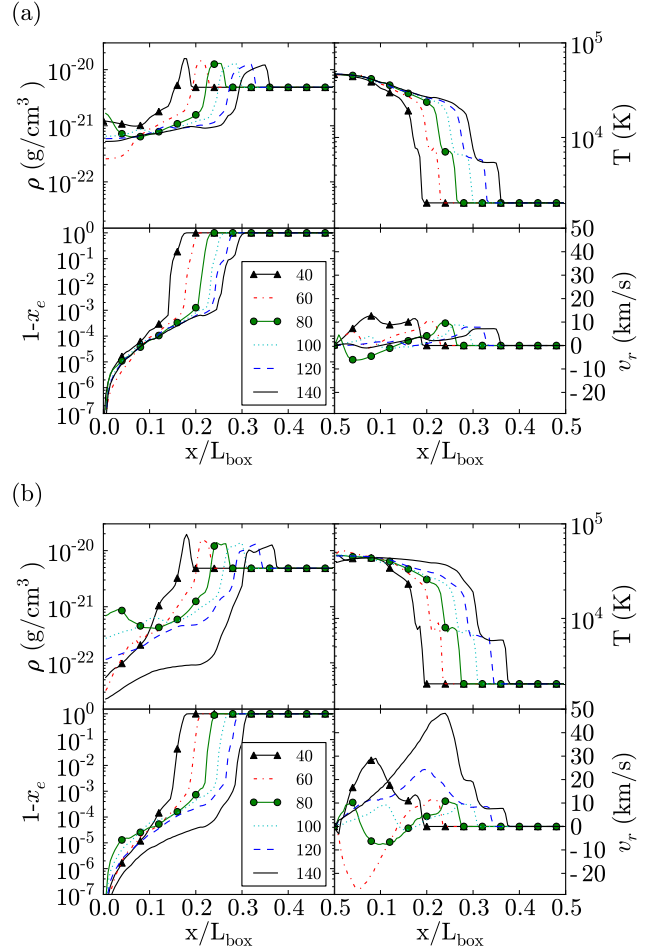


Figure 49. (a) No radiation pressure. Radial profiles of (clockwise from top left) density, temperature, radial velocity, and neutral fraction. Time units in the legend are in kyr. (b) Radial profiles with radiation pressure. The momentum transferred to the gas drives out the gas at higher velocities than without radiation pressure. Afterwards the central region is under-pressurised, and the gas infalls toward the centre, as seen at $t = 60$ kyr. Then the radiation pressure continues to force the gas outwards, increasing gas velocities up to 50 km/s.

gas pressure of the heated region. The imparted acceleration on a hydrogen atom $\mathbf{a}_{\text{rp}} = E_{\text{ph}}/c$. This is especially important when the ionisation front is in its initial R-type phase, where the gas has not reacted to the thermal pressure yet. Thus we construct a test that focuses on a small scales, compared to the Strömgren radius. The domain has a size of 8 pc with a uniform density $\rho = 2900$ cm $^{-3}$ and initial temperature $T = 10^3$ K. The source is located at the origin with a luminosity $L = 10^{50}$ ph s $^{-1}$ and a $T = 10^5$ K blackbody spectrum. We use one energy group $E_{\text{ph}} = 29.6$ eV. The grid is adaptively refined on overdensity with the same criterion as Test 8. The simulation is run for 140 kyr.

We compare nearly identical simulations but one with radiation pressure and one without radiation pressure to quantify its effects. Radial profiles of density, temperature, neutral fraction, and radial velocity are shown in Fig. 49 for both simulations at several times. Without radiation pressure, the evolution of the H II is matches the analytical

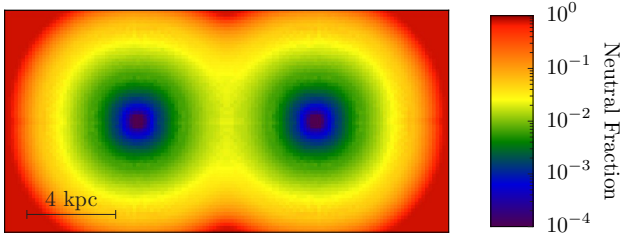


Figure 50. Slice of neutral fraction at $t = 500$ Myr through the sources in the consolidated H II test. There are no artifacts associated with rays being emitted from two sources. Both of the ionised regions are spherically symmetric before they overlap.

expectations described in §5.1. At $t = 140$ kyr with radiation pressure, the ionisation front radius is increased by $\sim 5\% = 0.16$ pc. However radiation pressure impacts the system the greatest inside the ionisation front. At $t = 40$ kyr, the central density is smaller by a factor of 20 with radiation pressure, but the temperatures are almost equal. A rarefaction wave thus propagates toward the centre, depicted by the negative radial velocities at $t = 60$ kyr. This raises the central density to $10^{-21} \text{ g cm}^{-3}$ at $t = 80$ kyr. Afterwards, the radiation continues to force gas outwards. From $t = 100$ kyr to $t = 140$ kyr, the maximum radial velocity of the ionised gas increases from 10 km s^{-1} to 50 km s^{-1} . This leaves behind an even more diffuse medium, lowering the gas density by a factor of 10 at $t = 140$ kyr. Thus the recombination rates are lower, resulting in increased ionisation fractions and temperatures in the H II region.

8.5 Consolidated H II region with two sources

Here we test for any inaccuracies in the case of multiple sources. We use the same test problem as Petkova & Springel (2009, §5.1.2), which has two sources with luminosities of $5 \times 10^{48} \text{ ph s}^{-1}$ and are separated by 8 kpc. The ambient medium is static with a uniform density of 10^{-3} cm^{-3} and $T = 10^4 \text{ K}$. This setup is similar to Test 1. The domain has a resolution of $128 \times 64 \times 64$. It is 20 kpc in width and is 10 kpc in height and depth. The problem is run for 500 Myr.

The H II regions grow to $r = 4$ kpc where they overlap. Then the two sources are enveloped in a common, elongated H II region. To illustrate this, we show the neutral fraction in Fig. 50. Our method keeps spherical symmetry close to the individual sources, and there are no perceptible artifacts from having multiple sources.

9 PARALLEL PERFORMANCE

Last we demonstrate the parallel performance of ENZO+MORAY in weak and strong scaling tests. For large simulations to consider radiative transfer, it is imperative that the code scales to large number of processors.

9.1 Weak Scaling

Weak scaling tests demonstrates how the code scales with the number of processors with a constant amount of work

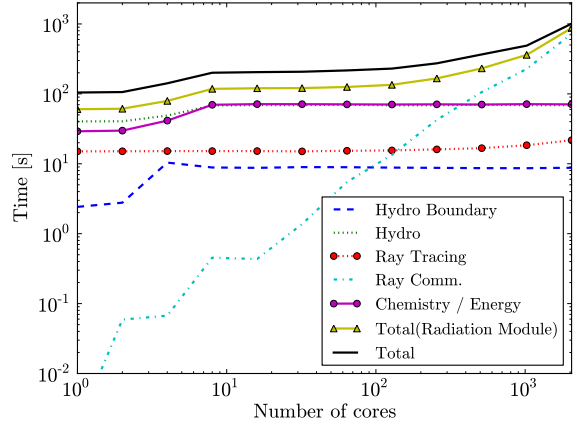


Figure 51. Weak scaling test with one 64^3 block per process. Each block has one source and is set up similar to the radiation hydrodynamics Test 5. Above 8 processes, all parts of the code exhibit good weak scaling except for the inter-processor ray communication. The radiation module timing include the ray tracing, communication, chemistry and energy solver, and all other overheads associated with the radiation transport. Cache locality of the data causes the decrease in performance from 1 to 8 processes.

per processor. Here we construct a test problem with a 64^3 block per core. The grid is not adaptively refined. The physical setup of the problem is nearly the same as Test 5 with a uniform density $\rho = 10^{-3} \text{ cm}^{-3}$ and initial temperature $T = 100 \text{ K}$. Each block has the same size of 15 kpc as Test 5. At the centre of each grid, there exists a radiation source with a luminosity $L = 5 \times 10^{48} \text{ ph s}^{-1}$ and a 17 eV monochromatic spectrum. The problem is run for 250 Myr. We run this test with $N_p = 2^n$ cores with $n = [0, 1 \dots 10, 11]$. The domain has (N_x, N_y, N_z) blocks that is determined with the MPI routine `MPI_Dims_create`. For example with $n = 7$, the problem is decomposed into $(N_x, N_y, N_z) = (4, 4, 8)$ blocks, producing a $256 \times 256 \times 512$ grid. We have run these on the original (Harpertown CPUs) nodes of the NASA NAS machine, Pleiades, with 8 cores per node. Fig. 51 shows the performance timings of various parts of the code. From one to two cores, the total time only increases by $\sim 1\%$ due to the overhead associated with the inter-processor message passing. From two to eight cores, the performance decreases in the hydrodynamics solver, chemistry and energy solver, and obtaining the hydrodynamic boundary conditions because of cache locality problems of the data being passed to the CPU. This occurs because of the CPU architecture, specifically the L1 cache and core connectivity. We see less of a penalty in newer processors, e.g. Intel Nehalem and Westmere CPUs. Above eight processes, these routines exhibit near perfect weak scaling to 2048 cores. Unfortunately there exists a $N_p^{1.5}$ dependence in the ray communication routines. It becomes the dominant process above 512 processes. We are actively pursuing a solution to this scaling problem. The other parts of the code exhibit excellent weak scaling. Overall it scales already well to 512 processes, and there is room to enhance the weak scalability of ENZO+MORAY in the near future.

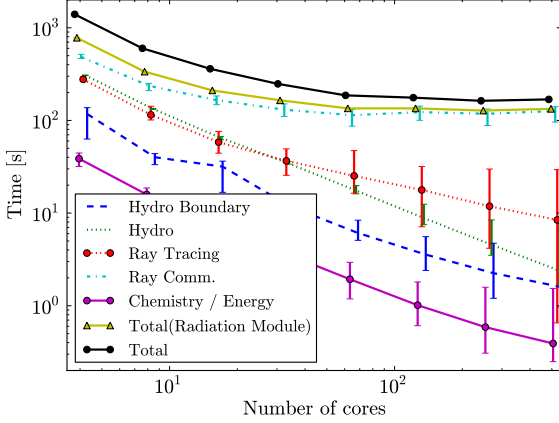


Figure 52. Strong scaling test with a 256^3 AMR calculation of cosmological reionisation with $\sim 392^3$ zones. The error bars represent the minimum and maximum time spent on a single core and measures load balancing. Each point has been slightly offset to make the error bars distinguishable. The hydrodynamics and non-equilibrium chemistry solvers scale well. The communication of rays does not scale well in this problem and limits the performance, where as the ray tracing scales relatively well.

9.2 Strong Scaling

Strong scaling tests shows how the problem scales with the number of processors for the same problem. The overhead associated with the structured AMR framework in ENZO can limit the strong scalability. One key property of strong scaling is that each processor must have sufficient work to compute, compared to the communication involved. In our experience, non-AMR calculations exhibit much better strong scaling than AMR ones because of reduced inter-processor communication. We use an AMR simulation to demonstrate the scalability of ENZO+MORAY in a demanding, research application. Here we use a small-box reionisation calculation with $L_{\text{box}} = 3$ Mpc/h, a resolution of 256^3 , and six levels of refinement. We measure the time spent on the hydrodynamics, non-equilibrium chemistry, ray tracing, and radiation transport communication in a timestep lasting 1 Myr, at $z = 10$. There are nine radiative transfer timesteps in this period. The box has 675 point sources, 15,943 AMR grids, and $6.01 \times 10^7 \approx 392^3$ computational cells in this calculation at this redshift. On average, 4.6×10^8 ray segments are traced each timestep. The ionised volume fraction is 0.10. The calculations are performed on the Nehalem nodes on Pleiades on 2^n cores, where $n = [2, \dots, 9]$.

Fig. 52 shows the strong scaling results of this calculation. The hydrodynamics and non-equilibrium chemistry routines scale very well in this range because they depend on local phenomena. Note that the dominant process is the radiation transport instead of the hydrodynamics when compared to the weak scaling tests. The error bars in the figure represent the deviations across all cores, and it shows that load balancing becomes an issue at 128 and 256 cores. This is an even larger problem for the ray tracing because the grids that host multiple radiation sources will have significantly more work than a distant grid. For example if a few central grids host several point sources, the exterior grids

must wait until those grids are finished ray tracing in order to receive the rays. This idle time constitutes the majority of the time spent in the ray communication routines despite our efforts (see §3.5) to minimize idle time. For this reason, the communication of rays does not scale in this problem. One solution is to split the AMR grids into smaller blocks based on the ray tracing work. This could impact the performance of the rest of ENZO by increasing the number of boundaries and thus communication. Nevertheless in simulations that are dominated by radiation transport, it will be advantageous to construct such a scheme to increase the feasibility of running larger problems.

10 SUMMARY

In this paper, we have presented our implementation, ENZO+MORAY, of adaptive ray tracing (Abel & Wandelt 2002) and its coupling to the hydrodynamics in the cosmology AMR code ENZO, making it a fully functional radiation hydrodynamics code. As this method is photon conserving, accurate solutions are possible with coarse spatial resolution. A new geometric correction factor to ray tracing on a Cartesian grid was described, and it is general to any implementation. We have exhaustively tested the code to problems with known analytical solutions and the problems presented in the RT06 and RT09 radiative transfer comparison papers. Additionally we have tested our code with more dynamical problems – champagne flows, Rayleigh-Taylor instabilities, photo-evaporation of a blastwave, beamed radiation, a time-varying source, and an H II region with MHD – to demonstrate the flexibility and fidelity of ENZO+MORAY. Because production simulations may not have the resolution afforded in these test problems, we have tested the dependence on spatial, angular, frequency, and temporal resolution. It provides accurate solutions even at low resolution, except for the large constant timesteps. However, we have described two methods to determine the radiative transfer timestep that are based on the variations in specific intensity or changes in neutral fraction inside the ionisation front. Both methods give very accurate results and provide the largest timestep to obtain an accurate solution, ultimately leading to higher computational efficiency. On the same topic, we have described a method to calculate the radiation field in the optically-thin limit with ray tracing.

Being a ray tracing code, it scales with the number of radiation sources; nevertheless, it scales well to $O(10^3)$ processors for problems with $\sim 10^9$ computational cells and $\sim 10^4$ sources, such as reionisation calculations. We have also shown that the code shows good strong scaling in AMR calculations, given a large enough problem. The combination of AMR and adaptive ray tracing allows for high-resolution and high-dynamical range problems, e.g. present-day star formation, molecular cloud resolving cosmological galaxy formation, and H II regions of Population III stars. Furthermore, we have included Lyman-Werner absorption, secondary ionisations from X-ray radiation, Compton heating from photon scattering, and radiation pressure into the code, which extends the reach of ENZO+MORAY to study AGN feedback, stellar winds, and local star formation. Coupling the radiative transfer with MHD further broadens the applicability of our code. The full implementation is included in

the latest public version of ENZO³, providing the community with a full-featured radiation hydrodynamics AMR code.

ACKNOWLEDGMENTS

We thank Ji-hoon Kim, Richard Klein, and Jeff Oishi for helpful comments on the manuscript. J. H. W. is supported by NASA through Hubble Fellowship grant #120-6370 awarded by the Space Telescope Science Institute, which is operated by the Association of Universities for Research in Astronomy, Inc., for NASA, under contract NAS 5-26555. Computational resources were provided by NASA/NCCS award SMD-09-1439. The majority of the analysis and plots were done with *yt* (Turk et al. 2011).

REFERENCES

- Abel T., Anninos P., Zhang Y., Norman M. L., 1997, *New Astronomy*, 2, 181
- Abel T., Norman M. L., Madau P., 1999, *ApJ*, 523, 66
- Abel T., Wandelt B. D., 2002, *MNRAS*, 330, L53
- Abel T., Wise J. H., Bryan G. L., 2007, *ApJL*, 659, L87
- Altay G., Croft R. A. C., Pelupessy I., 2008, *MNRAS*, 386, 1931
- Alvarez M. A., Bromm V., Shapiro P. R., 2006a, *ApJ*, 639, 621
- Alvarez M. A., Bromm V., Shapiro P. R., 2006b, *ApJ*, 639, 621
- Alvarez M. A., Wise J. H., Abel T., 2009, *ApJL*, 701, L133
- Anninos P., Zhang Y., Abel T., Norman M. L., 1997, *New Astronomy*, 2, 209
- Aubert D., Teyssier R., 2008, *MNRAS*, 387, 295
- Auer L. H., Mihalas D., 1970, *MNRAS*, 149, 65
- Axford W. I., 1961, *Royal Society of London Philosophical Transactions Series A*, 253, 301
- Berger M. J., Colella P., 1989, *Journal of Computational Physics*, 82, 64
- Bisbas T. G., Wünsch R., Whitworth A. P., Hubber D. A., 2009, *A&A*, 497, 649
- Bodenheimer P., Tenorio-Tagle G., Yorke H. W., 1979, *ApJ*, 233, 85
- Brouillette M., 2002, *Annual Review of Fluid Mechanics*, 34, 445
- Bryan G. L., Norman M. L., 1997, *ArXiv Astrophysics e-prints (astro-ph/9710187)*
- Ciardi B., Ferrara A., Marri S., Raimondo G., 2001, *MNRAS*, 324, 381
- Dalgarno A., Stephens T. L., 1970, *ApJL*, 160, L107+
- Dedner A., Kemm F., Kröner D., Munz C., Schnitzer T., Wesenberg M., 2002, *Journal of Computational Physics*, 175, 645
- Draine B. T., Bertoldi F., 1996, *ApJ*, 468, 269
- Finlator K., Özel F., Davé R., 2009, *MNRAS*, 393, 1090
- Franco J., Tenorio-Tagle G., Bodenheimer P., 1990, *ApJ*, 349, 126
- Gnedin N. Y., 2000, *ApJ*, 542, 535
- Gnedin N. Y., Abel T., 2001, *New Astronomy*, 6, 437
- Gnedin N. Y., Ostriker J. P., 1997, *ApJ*, 486, 581
- González M., Audit E., Huynh P., 2007, *A&A*, 464, 429
- Górski K. M., Hivon E., Banday A. J., Wandelt B. D., Hansen F. K., Reinecke M., Bartelmann M., 2005, *ApJ*, 622, 759
- Haiman Z., Abel T., Rees M. J., 2000, *ApJ*, 534, 11
- Harten A., Lax P. D., van Leer B., 1983, *SIAM Review*, 25, 35
- Hasegawa K., Umemura M., Susa H., 2009, *MNRAS*, 395, 1280
- Hester J. J., et al., 1996, *AJ*, 111, 2349
- Hjellming R. M., 1966, *ApJ*, 143, 420
- Iliev I. T., et al., 2006, *MNRAS*, 371, 1057
- Iliev I. T., et al., 2009, *MNRAS*, pp 1313–+
- Iliev I. T., Mellema G., Pen U., Merz H., Shapiro P. R., Alvarez M. A., 2006, *MNRAS*, 369, 1625
- Iliev I. T., Mellema G., Shapiro P. R., Pen U., 2007, *MNRAS*, 376, 534
- Johnson J. L., Greif T. H., Bromm V., 2007, *ApJ*, 665, 85
- Kahn F. D., 1954, *Bull. Astron. Inst. Netherlands*, 12, 187
- Kim J. H., Wise J. H., Alvarez M. A., Abel T., 2011, *ApJ*, In preparation
- Krumholz M. R., Klein R. I., McKee C. F., Bolstad J., 2007, *ApJ*, 667, 626
- Krumholz M. R., Stone J. M., Gardiner T. A., 2007, *ApJ*, 671, 518
- Lasker B. M., 1966, *ApJ*, 143, 700
- Liska R., Wendroff B., 2003, *SIAM Journal on Scientific Computing*, 25, 995
- Mathews W. G., 1965, *ApJ*, 142, 1120
- McQuinn M., Lidz A., Zahn O., Dutta S., Hernquist L., Zaldarriaga M., 2007, *MNRAS*, 377, 1043
- Mellema G., Iliev I. T., Alvarez M. A., Shapiro P. R., 2006, *New Astronomy*, 11, 374
- Mihalas D., Mihalas B. W., 1984, *Foundations of radiation hydrodynamics*
- Miralda-Escudé J., Haehnelt M., Rees M. J., 2000, *ApJ*, 530, 1
- Norman M. L., Paschos P., Abel T., 1998, *Mem. Soc. Astron. Italiana*, 69, 455
- Oort J. H., 1954, *Bull. Astron. Inst. Netherlands*, 12, 177
- O’Shea B. W., Bryan G., Bordner J., Norman M. L., Abel T., Harkness R., Kritsuk A., 2004, *ArXiv Astrophysics e-prints (astro-ph/0403044)*
- Osterbrock D. E., 1989, *Astrophysics of gaseous nebulae and active galactic nuclei*
- Paardekooper J., Kruip C. J. H., Icke V., 2010, *A&A*, 515, A79+
- Pawlik A. H., Schaye J., 2008, *MNRAS*, 389, 651
- Pawlik A. H., Schaye J., 2010, *ArXiv e-prints (1008.1071)*
- Petkova M., Springel V., 2009, *MNRAS*, 396, 1383
- Razoumov A. O., Scott D., 1999, *MNRAS*, 309, 287
- Ricotti M., Gnedin N. Y., Shull J. M., 2001, *ApJ*, 560, 580
- Rijkhorst E., Plewa T., Dubey A., Mellema G., 2006, *A&A*, 452, 907
- Rybicki G. B., Lightman A. P., 1979, *Radiative processes in astrophysics*
- Sandford II M. T., Whitaker R. W., Klein R. I., 1982, *ApJ*, 260, 183
- Schatzman E., Kahn F. D., 1955, in *Gas Dynamics of Cosmic Clouds Vol. 2 of IAU Symposium, On the Motion of H I and H II Regions*. pp 163–+
- Shapiro P. R., Iliev I. T., Alvarez M. A., Scannapieco E.,

³ <http://enzo.googlecode.com>

- 2006, *ApJ*, 648, 922
- Shapiro P. R., Iliev I. T., Raga A. C., 2004, *MNRAS*, 348, 753
- Shull J. M., van Steenberg M. E., 1985, *ApJ*, 298, 268
- Sokasian A., Abel T., Hernquist L., Springel V., 2003, *MNRAS*, 344, 607
- Sokasian A., Abel T., Hernquist L. E., 2001, *New Astronomy*, 6, 359
- Spitzer L., 1978, *Physical processes in the interstellar medium*
- Spitzer Jr. L., 1948, *ApJ*, 107, 6
- Spitzer Jr. L., 1949, *ApJ*, 109, 337
- Spitzer Jr. L., 1954, *ApJ*, 120, 1
- Spitzer Jr. L., Savedoff M. P., 1950, *ApJ*, 111, 593
- Stecher T. P., Williams D. A., 1967, *ApJL*, 149, L29+
- Stone J. M., Gardiner T. A., Teuben P., Hawley J. F., Simon J. B., 2008, *ApJS*, 178, 137
- Stone J. M., Mihalas D., Norman M. L., 1992, *ApJS*, 80, 819
- Strömgren B., 1939, *ApJ*, 89, 526
- Susa H., 2006, *PASJ*, 58, 445
- Trac H., Cen R., 2007, *ApJ*, 671, 1
- Turk M. J., Smith B. D., Oishi J. S., Skory S., Skillman S. W., Abel T., Norman M. L., 2011, *ApJS*, 192, 9
- van Leer B., 1977, *Journal of Computational Physics*, 23, 276
- Wang P., Abel T., 2009, *ApJ*, 696, 96
- Whalen D., Norman M. L., 2006, *ApJS*, 162, 281
- Whalen D., Norman M. L., 2008, *ApJ*, 673, 664
- Wise J. H., Abel T., 2008a, *ApJ*, 684, 1
- Wise J. H., Abel T., 2008b, *ApJ*, 685, 40
- Wise J. H., Cen R., 2009, *ApJ*, 693, 984
- Wise J. H., Turk M. J., Norman M. L., Abel T., 2010, *ArXiv e-prints* (1011.2632)
- Yorke H. W., 1986, *ARA&A*, 24, 49
- Yorke H. W., Tenorio-Tagle G., Bodenheimer P., 1983, *A&A*, 127, 313

This paper has been typeset from a $\mathrm{T}_{\mathrm{E}}\mathrm{X}$ / $\mathrm{L}^{\mathrm{A}}\mathrm{T}_{\mathrm{E}}\mathrm{X}$ file prepared by the author.

